

1

[ATLAS Semivisible Jets]

2

[Elena Laura Busch]

3

Submitted in partial fulfillment of the
requirements for the degree of
Doctor of Philosophy
under the Executive Committee
of the Graduate School of Arts and Sciences

4

5

6

7

8

COLUMBIA UNIVERSITY

9

2024

10

© 2024

11

[Elena Laura Busch]

12

All Rights Reserved

13

Abstract

14

[ATLAS Semivisible Jets]

15

[Elena Laura Busch]

16

Abstract of dissertation (place-holder).

Table of Contents

18	Acknowledgments	xv
19	Dedication	xvi
20	Introduction or Preface	1
21	I Theory	2
22	Chapter 1: The Standard Model	3
23	1.1 Phenomenology: Particles and Forces	3
24	1.1.1 Particles	3
25	1.1.2 Forces	5
26	1.2 QCD and Jets	7
27	1.3 Symmetries	8
28	1.3.1 Spontaneous Symmetry Breaking and The Higgs Mechanism	9
29	1.4 Experimental Validation of the Standard Model	10
30	1.5 Limitations of the Standard Model	11
31	Chapter 2: Physics Beyond the Standard Model	13
32	2.1 Hidden Valley Models	13
33	2.2 Dark QCD	14

34	2.3 Semi-visible Jets	15
35	II Experiment	17
36	Chapter 3: The Large Hadron Collider	18
37	3.1 Accelerator Physics	19
38	3.1.1 The Journey of a Proton	19
39	3.1.2 Magnets	20
40	3.2 Luminosity	21
41	3.3 LHC Timeline	24
42	Chapter 4: The ATLAS Detector	26
43	4.1 Coordinate System and Geometry	26
44	4.2 Inner Detector	28
45	4.2.1 Pixel Detector	28
46	4.2.2 Semiconductor Tracker	29
47	4.2.3 Transition Radiation Tracker	29
48	4.3 Calorimeters	30
49	4.3.1 Liquid Argon Calorimeter	31
50	4.3.2 Tile Calorimeter	34
51	4.4 Muon Spectrometer	35
52	4.5 Magnet System	37
53	4.6 Forward Detectors	38
54	4.7 Trigger and Data Acquisition	39

55	Chapter 5: Particle Reconstruction and Identification	41
56	5.1 Inner Detector Tracks	41
57	5.2 Photons and Electrons	42
58	5.3 Muons	44
59	5.4 Jets	46
60	5.4.1 Calorimeter Clusters	47
61	5.4.2 Particle Flow Algorithm	48
62	5.4.3 Jet Clustering	49
63	5.4.4 Ghost Track Association	52
64	5.5 Missing Transverse Energy	53
65	III Search	55
66	Chapter 6: Monte Carlo and Data	56
67	6.1 Data	56
68	6.2 Simulation	57
69	6.2.1 Simulated Backgrounds	57
70	6.2.2 Signal Simulation	58
71	Chapter 7: Machine Learning Tools	61
72	7.1 Introduction	61
73	7.1.1 Particle Flow Network (Supervised)	62
74	7.1.2 ANTELOPE (Semi-supervised)	72
75	Chapter 8: Analysis Strategy	79

76	8.1 Preselection	79
77	8.2 SVJ Fit and Discovery Analysis Strategies	81
78	8.3 Analysis Regions	85
79	8.3.1 Control and Validation Regions	85
80	8.3.2 Signal Region	87
81	8.4 Background Estimation	89
82	8.5 Fit Strategy and Validation	90
83	8.5.1 SVJ Fit Strategy	90
84	8.5.2 Discovery Strategy)	103
85	Chapter 9: Results	108
86	Conclusion or Epilogue	109
87	References	113
88	Appendix A: Trigger Studies	119
89	Appendix B: Machine Learning Approaches	123
90	B.1 Unsupervised: AE vs. ANTELOPE	123
91	B.2 PFN Optimality Checks	124
92	B.3 Supervised: BDT vs. PFN	127
93	B.4 Single Jet vs Jet System ML Approach	127
94	B.5 PFN Training Composition	129
95	B.6 E_T^{miss} and $E_T^{\text{miss}}\phi$ Shapes	131

96	B.6.1 NCB Preselection	131
97	B.6.2 TileCal Correction	133
98	Appendix C: Truth Studies	136
99	C.1 Jet dR Matching	136

List of Figures

101	1.1	Diagram of the 17 particles comprising the Standard Model	4
102	1.2	Fundamental particle interactions of the three fundamental forces described by the Standard Model [2].	6
104	1.3	An example Feynmann diagram of jet production	7
105	1.4	An illustration of the “hat shaped” potential of the Higgs field, resulting in a non-zero vacuum expectation value.	9
107	2.1	Illustration of the hidden valley potential.	14
108	2.2	The massive mediator particle Z' of the s-channel realization of a HV model	14
109	3.1	The LHC accelerator complex at CERN [29]	20
110	3.2	The octants of the LHC and location of various beam activities [28]. Stars indicate the locations of beam collisions, and the associated detectors recording the outcome of those collisions.	21
113	3.3	(Left) Total integrated luminosity over the course of Run 2. (Right) Average number of $p p$ interactions per bunch crossing in Run 2. Each curve is weighted by the integrated luminosity for the year.	23
116	3.4	Timeline of LHC and HL-LHC activities [31]. Integrated luminosity estimates are approximate, and not reflective of the exact amount delivered to each experiment. .	25
118	4.1	ATLAS coordinate system and geometry	28
119	4.2	A 3D visualization of the structure of the ID in the barrel region [35]	29
120	4.3	ATLAS calorimetery system [36]	30

121	4.4	Diagram of a segment of the EMB, demonstrating the accordion plate arrangement [37]	32
122			
123	4.5	A LAr pulse as produced in the detector (triangle) and after shaping (curve) [37]	33
124			
125	4.6	Readout gap structure in HEC [37]	33
126			
127	4.7	TileCal wedge module [40]	35
128			
129	4.8	Cross section view of the muon spectrometer system [41]	36
130			
131	4.9	Layout of the barrel and endcap toroid magnets [34]	38
132			
133	5.1	Graphic illustrating the various objects and high level features identified by ATLAS object reconstruction, and their interaction with different systems of the ATLAS detector [44]	42
134			
135	5.2	Track reconstruction seeding, finding and fitting illustration [45]	43
136			
137	5.3	Three types of EM object candidates [47].	44
138			
139	5.4	Four types of muon track candidates [49].	46
140			
141	5.5	The fragmentation and hadronization processes undergone by a quark produced in a proton-proton collision [51].	47
142			
143	5.6	A flow chart illustrating the particle flow algorithm progression [56].	50
144			
145	5.7	A comparison of jet clustering with four different jet algorithms. The anti- k_t algorithm is observed to create the most conical jets, where the shape of the jet is immune to the presence of soft radiation [52].	51
146			
147	5.8	A comparison of MC simulation and data for $Z \rightarrow \mu\mu$ events where real $E_T^{\text{miss}} = 0$ [63]. The resolution of the missing energy in the transverse ($x - y$) plane is observed to increase with increasing total $\sum E_T$	54
148			
149	6.1	The transverse momentum slices of the QCD MC simulation, overlayed to show how they come together to create a smooth distribution (left) once weighted properly. The original unweighted distribution is shown on the right, illustrating the enhanced statistics for the high p_T range.	58
150			

147	6.2	Background processes relevant to the SVJ signal. The agreement between the black line (data) and grey line (all MC processes combined) illustrates that this collection of background processes is sufficient to model the expected E_T^{miss} in the selected data events.	59
151	7.1	The Energy/Particle Flow Network concept, from Ref. [69].	63
152	7.2	An annotated diagram of the PFN architecture. y and ϕ represent geometric in- formation for the input particles, z represents energy information, and PID encom- passes any other particle ID information in the input.	63
155	7.3	A illustration of the expected dijet behavior of semi-visible jets, where one jet is closely aligned with E_T^{miss}	64
157	7.4	Illustration of track coordinates d_0 and z_0	65
158	7.5	Distributions of the track multiplicity in the leading and subleading jets, comparing signal and background PFN training samples.	65
160	7.6	A diagram demonstrating how the two jet system is rotated in (ϕ, η)	66
161	7.7	The 6 PFN track variables in background MC and signal MC. There are some differences between signal and background, but the track kinematics are largely similar.	66
164	7.8	The 6 PFN track variables in data and background MC, after the scaling and ro- tation procedure is applied. There is excellent modeling of the data by the MC within the track variables. The slight discrepancy in the phi distribution is due to the modeling of dead TileCal cells by the QCD MC, which will be discussed in Chapter 8. The level of discrepancy is determined to be within tolerance given that the final result will be data driven and the QCD model is used in the PFN training only.	67
171	7.9	PFN score for background MC, data, and signal, comparing a PFN training on QCD-only vs all-background MC samples. The average AUC for the QCD-only training (left) is 0.93, while the average AUC for the mixed background training (right) is 0.84. The sensitivity estimate across the grid is better for the QCD-only training - from the distribution we can conclude that this is because the sensitivity to MET enhanced signals is greatly reduced.	69
177	7.10	PFN architecture loss during training as a function of epoch (left) and the evaluated loss over the signal and background (right).	69

179	7.11 ROC the PFN score for combined signal (true positive) and QCD background (false positive).	70
181	7.12 AUC from the PFN score for each signal in the SVJ grid, shown versus the QCD- only training sample.	71
183	7.13 PFN score for two signals and the total background MC (top), and between data and MC (bottom). The difference between data and MC efficiency is minimal (< 5%).	71
186	7.14 A visual representation of the 64 PFN latent space variables which create the input of the VAE component of ANTELOPE. The left shows a 2D histogram of the PFN latent space index (0-63) versus the value assumed by that index. The right shows 1D histograms of two particular PFN latent space variables.	73
190	7.15 An annotated diagram of the ANTELOPE architecture.	74
191	7.16 ANTELOPE architecture loss during training as a function of epoch.	75
192	7.17 ANTELOPE score distribution comparing data and the total background MC (left), with good agreement observed between data and simulated background, and com- paring all background MC to signals (right), revealing good discrimination power.	76
196	7.18 AUC from the ANTELOPE score for each signal in the SVJ grid.	77
197	7.19 Comparing data and the alternate signal models for the PFN score (left) and AN- TELOPE score (right). The emerging jet signal is an example of the gain of the model-independent ANTELOPE approach, where it has a bimodal shape in PFN score but is clearly tagged as anomalous by ANTELOPE.	78
201	7.20 Comparing data and the alternate signal models in terms of sensitivity (S/\sqrt{B}) for the PFN and ANTELOPE tools, applying the selection that is used in the analysis. The ANTELOPE network is found to provide significant added sensitivity to alter- nate signals such as the gluino → R-hadron and emerging jets, which have higher E_T^{miss} than the SVJs.	78
206	8.1 Preselection cutflow for data (left) and signal (right).	80
207	8.2 Energy and momentum analysis variables at preselection, for data, all background MC and representative signal models. m_T is the key fit variable, and this plot illustrates the smoothly falling background in comparison to the resonant shape of the signals. m_T is further illustrated in Figure 8.9.	82

211	8.3 Orientation analysis variables at preselection, for data, all background MC and 212 representative signal models. While $\Delta\phi(E_T^{\text{miss}}, j)$ variables are not used explicitly 213 in the analysis flow, they help create a picture of the event.	83
214	8.4 Flow of analysis selections, regions, and background estimation/validation fitting 215 strategy. TODO: diagram needs to be corrected	84
216	8.5 Distributions of the subleading jet width width_{j2} (left) and leading jet with width_{j1} 217 (right) in data, background MC and signals at preselection. All SVJ signals are 218 seen to be wider than the background in width_{j2} . The same is not true for width_{j1} , 219 where some signals are observed to closely match the background.	85
220	8.6 2D plots revealing correlations between width_{j2} and m_T (left), width_{j2} and ML 221 score (middle), and m_T with ML score (right). For the top row, the ML score is 222 the PFN score, and for the bottom three, the ML score is the ANTELOPE score. 223 Minimal correlations are observed and are shown to not sculpt m_T , validating these 224 variables for analysis region construction and statistical treatment.	86
225	8.7 m_T in simulation across the CR, VR, and SR for both PFN (left) and ANTELOPE 226 (right) selections.	87
227	8.8 Definition of CR, VR, and SR regions using width_{j2} and the ML score, along with 228 the population of each region in data statistics. The SVJ Fit region is shown on top 229 with the PFN score on the x-axis, and Discovery region is shown on the bottom, 230 with the ANTELOPE score on the x-axis.	88
231	8.9 The resonant shape of the SVJ signals in m_T , in contrast to the smoothly falling 232 m_T background. The high R_{inv} signals (right) boast a wider shape, making them 233 more difficult to detect, while the low R_{inv} signals(left) produce a more narrow 234 resonance in m_T	89
235	8.10 Background-only m_T fits using representative MC in the CR (left), VR (middle), 236 and SR (right).	91
237	8.11 Background-only m_T fits using data in the full statistics CR and VR regions.	92
238	8.12 Post-fit parameters for the PFN CR and VR.	92
239	8.13 Background-only m_T fits using data in orthogonal but statistically identical samples 240 to the SR, obtained by downsampling the CR/VR statistics, for the CR (top) and 241 VR (bottom).	93
242	8.14 m_T distribution in the data CR, before (left) and after (right) smoothing.	94
243	8.15 p -value histograms from 100 fits to Asimov data in the CR.	94

244	8.16 Example S+B fits on background only spectrum (without systematics) for a variety 245 of signal points.	95
246	8.17 Example S+B fits on a background m_T spectrum with injected signal from the point 247 (2500 GeV , $R_{inv}=0.2$).	97
248	8.18 Linearity of fitted vs. injected signal across m_T , for signal points with $R_{inv}=0.2$, 249 0.4, 0.6, and 0.8, with several Z' masses (2500 GeV, 3500 GeV, and 5000 GeV top 250 to bottom) for a single CR template with no systematics.	98
251	8.19 Spurious signal at a variety of injected values (1, 2, and 5σ significant), for all 252 signal points in the grid, $R_{inv}=0.2$ (top left), 0.4 (top right), 0.6 (bottom left), and 253 0.8 (bottom right). i	100
254	8.20 $S_{\text{spur}}/\sigma_{\text{fit}}$ at a variety of injected values (1, 2, and 5σ significant), for all signal 255 points in the grid, $R_{inv}=0.2$ (top left), 0.4 (top right), 0.6 (bottom left), and 0.8 256 (bottom right). i	101
257	8.21 95% C.L. upper limits for signal models across Z' mass, for four different R_{inv} frac- 258 tions, from the CR region (without systematics).	102
259	8.22 Post-fit parameters for the ANTELOPE CR and VR.	103
260	8.23 Post-fit function and residuals for the ANTELOPE CR and VR.	104
261	8.24 Example determinations of the 60% mass window means for several signal points. .	105
262	8.25 Signal mass resolution for m_T binning for the signal grid in (R_{inv} , mass) space. .	105
263	8.26 m_T bins based on the signal mass resolution and the minimum 100 GeV width 264 requirement, for each R_{inv} signal category.	106
265	8.27 BumpHunter fits on the ANTELOPE m_T spectra for both the CR and VR. In 266 a signal-depleted region, good agreement with the background estimation is ob- 267 served.	107
268	8.28 BumpHunter p-values extracted for 100 Asimov toys for both the ANTELOPE 269 CR (top) and VR (bottom) showing the highest (left) and lowest (right) p-value 270 fits. The number of events in the histogram deviates from 100 based on failed 271 background-only fits.	107
272	A.1 Trigger yield and efficiency for both the MET trigger and small-R jet trigger ap- 273 proach. Each entry represent a signal point, labelled by the Z' mass and the 274 R_{inv} fraction.	119

275	A.2 The factor of improvement in S/\sqrt{B} for each trigger method compared to the un-	
276	triggered case.	120
277	A.3 The ratio of S/\sqrt{B} of jet trigger over E_T^{miss} trigger selection.	120
278	A.4 Analysis variables where high R_{inv} signals a clearly distinct from background and	
279	low R_{inv} variables. On the contrary, leading jet p_T is one of the only variables	
280	where low R_{inv} signals are distinct from background.	122
281	A.5 OR of jet and E_T^{miss} triggers.	122
282	B.1	123
283	B.2	124
284	B.3 AUC from the PFN score for each signal in the SVJ grid, shown versus the QCD-	
285	only training sample (top) and the total MC background (bottom). Note the three	
286	missing points will be added shortly - they were delayed due to a DAOD production	
287	mistake.	125
288	B.4 Comparison of PFN AUC (top), SIC (middle), and sensitivity in the m_T mass win-	
289	dow (bottom) for a single PFN model (left) vs. two models, trained on $R_{inv} < 0.5$	
290	and > 0.5 separately.	126
291	B.5 Preferred cuts on the PFN score for each point in the grid, comparing the effect of	
292	adding the NCB preselection.	127
293	B.6 Scans done to check for optimality of PFN training parameters.	128
294	B.7	128
295	B.8 ϕ Performance comparison between single jet and jet system ML approach	129
296	B.9 ϕ Comparison in the AUC score across the grid for the mixed background strategy	
297	vs the QCD only strategy. The bottom table highlights that the QCD only strategy	
298	gives superior sensitivity across the signal grid.	130
299	B.10 E_T^{miss} in data before and after Tight event cleaning is applied.	131
300	B.11 E_T^{miss} vs jet1 p_T in data before and after Tight event cleaning is applied.	132
301	B.12 η vs ϕ for leading and subleading jets, before and after the application of tight	
302	cleaning.	132

303	B.13 Added NCB preselection and impact on E_T^{miss} shape.	133
304	B.14 NCB preselection impact on data and signal yields.	134
305	B.15 Impact of tight cleaning and non-collision background preselection.	135
306	B.16 $E_T^{\text{miss}}\phi$ in data, before (left) and after (right) application of the TileCal correction	
307	tool.	135
308	C.1 Index of jets truth matched (by requirement of $\Delta R < 0.4$) with dark quark.	136
309	C.2 Percent of jets with $\Delta R(j, E_T^{\text{miss}}) < 0.4$ comparing two jet identification strategies.	
310	Leading and subleading jets are seen to be the better metric for identifying jets	
311	associated with the dark quark decay.	137

List of Tables

313	6.1 Fixed parameters in the Pythia8 HV model	60
314	6.2 Values for m_{dark}	60
315	6.3 Mass points and cross sections of the SVJ search signal grid	60

316

Acknowledgements

317 Insert your acknowledgements text here. This page is optional, you may delete it if not

318 needed.

319

Dedication

320

Dedicated to my friends and family

321

Introduction or Preface

322 Insert your preface text here if applicable. This page is optional, you may delete it if not
323 needed. If you delete this page make sure to move page counter comment in thesis.tex to correct
324 location.

325

Part I

326

Theory

Chapter 1: The Standard Model

329 The Standard Model of particle physics is a universally accepted framework which explains
 330 the interactions of fundamental particles. All known fundamental particles, outlined in Figure
 331 1.1, are represented in the Standard Model. The model describes three of the four known forces:
 332 the electromagnetic force, the weak force, and the strong force. Gravity, the fourth fundamental
 333 force, is not addressed by the Standard Model. The Standard Model was primarily developed over
 334 the course of the 1960s and 1970s, by combining the work of many physicists into one coherent
 335 model. The Standard Model has been established as a well-tested theory by decades of experimen-
 336 tal physics research.

337 This chapter will seek to introduce the phenomenology and mathematical foundations of the
 338 Standard Model, and present the supporting experimental evidence. Phenomenon which are unex-
 339 plained by the Standard Model such as gravity will be considered at the end of the chapter, leading
 340 to an exploration of theories beyond the Standard Model in the subsequent chapter.

341 **1.1 Phenomenology: Particles and Forces**

342 1.1.1 Particles

343 A classic representation of the particles comprising the Standard Model is shown in Figure
 344 1.1. The two primary particles classes are bosons (gauge bosons and the scalar Higgs boson) and
 345 fermions (leptons and quarks). The bosons are carriers of fundamental forces, while the fermions
 346 are the building blocks of matter. Fermions are sorted into three *generations*, and each fermion is
 347 identified by a unique *flavor*.

348 Each entry in the table in Figure 1.1 is accompanied by 3 characteristic numbers: mass, charge,
 349 and spin. The mass of each particle is determined to limited precision by experimental observation,

Standard Model of Elementary Particles

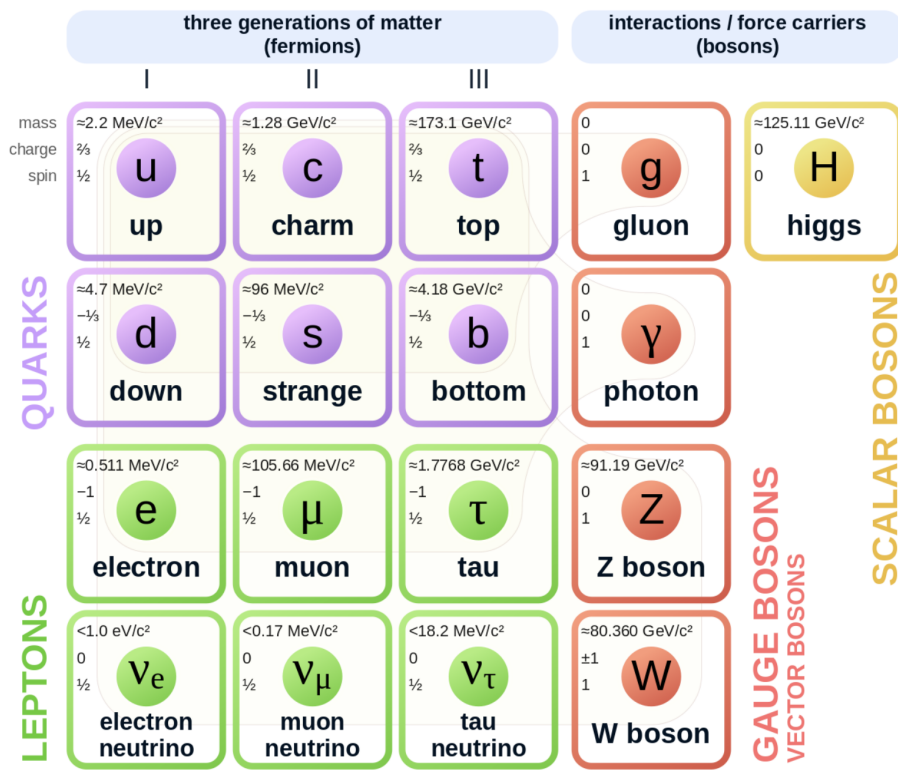


Figure 1.1: Diagram of the 17 particles comprising the Standard Model

350 with the exception of photons and gluons which are known to be massless. Charge refers to the
351 electromagnetic charge, which is integer for leptons and fractional for quarks. Spin is an intrinsic
352 form of angular momentum carried by fundamental particles; all fermions have half integer spin,
353 while bosons have integer spin.

354 Each particle is also known to have an *antiparticle*. Each antiparticle has the same mass but the
355 opposite charge of their Standard Model counter part; for example, the antiparticle of the electron
356 is the positron, which has all the same properties but a positive charge. The photon, Z boson,
357 and Higgs are each their own antiparticle. The nature of antineutrinos is an open question driving
358 neutrino physics research, as it is not currently known whether neutrinos are their own antiparticle.

359 1.1.2 Forces

360 The three fundamental forces explained by the Standard Model are the electromagnetic force,
361 the strong force, and the weak force. The photon is the carrier of the electromagnetic force, which
362 dictates the nature of interactions between electrically charged particles, and is widely covered by
363 introductory physics courses. The electromagnetic force has an infinite interaction range, a result
364 of the massless and non-self interaction nature of the photon. The electromagnetic interaction is
365 described by the theory of quantum electrodynamics (QED).

366 The weak force gives rise to atomic radiation and decay. It allows for the processes of beta
367 decay, which enables conversion between neutrons and protons within the nucleus of an atom. In
368 the process of beta decay, a proton decays into a neutron, a positron, and a neutrino; or, a neutron
369 decays into a proton, an electron and an antineutrino. The weak interaction allows for quark flavor
370 mixing, the which enables beta decay. The W^+ , W^- , and Z^0 are the force carriers of the weak force.
371 The effective range of the weak force is limited to subatomic distances, as a result of the massive
372 nature of the mediator bosons. The unified theory of the electroweak interaction posits that at high
373 enough energies the electromagnetic interaction and the weak force merge into the same force.
374 This threshold is termed the unification energy and calculated to be about 246 GeV [1].

375 The strong force confines quarks into hadron particles, such as protons and neutrons. The

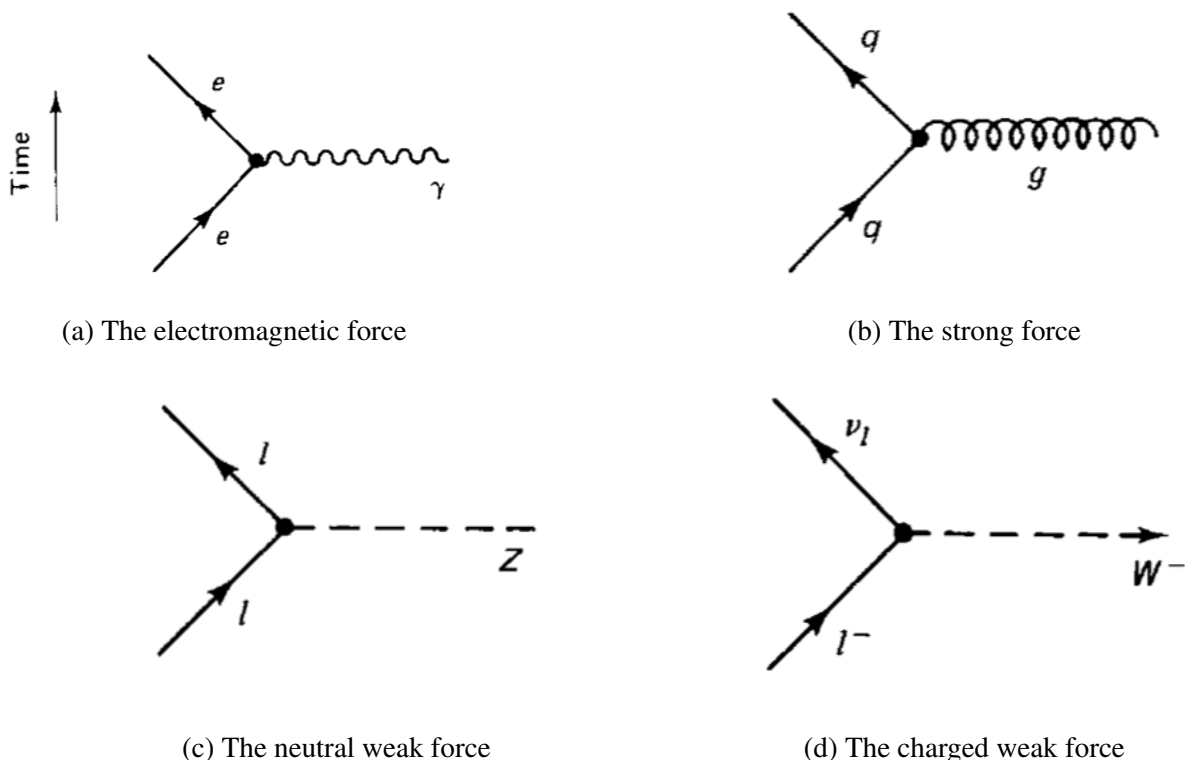


Figure 1.2: Fundamental particle interactions of the three fundamental forces described by the Standard Model [2].

376 strong force also allows for the creation of atomic nuclei by binding protons and neutrons together,
377 and is generally referred to as the “nuclear force” in this context. The gluon is the mediator of
378 the strong force, which is a short-range force which acts at subatomic distances on the order of
379 10^{-15} m. At this range, the strong force is about 100x as strong as the electromagnetic force,
380 which allows for the creation of positively charged nuclei [2]. The strong force is described by the
381 theory of quantum chromodynamics (QCD). In the same way that QED dictates the interaction of
382 electrically charges particles, QCD dictates the interactions of *color-charged* particles. Due to the
383 particular importance of QCD in this thesis, this topic will be explored in detail in section 1.2.

The fundamental Feynmann diagram for each of the three forces discussed here is depicted in Figure 1.2. The fourth fundamental force, gravity, is not currently explained by any known mechanism within the Standard Model.

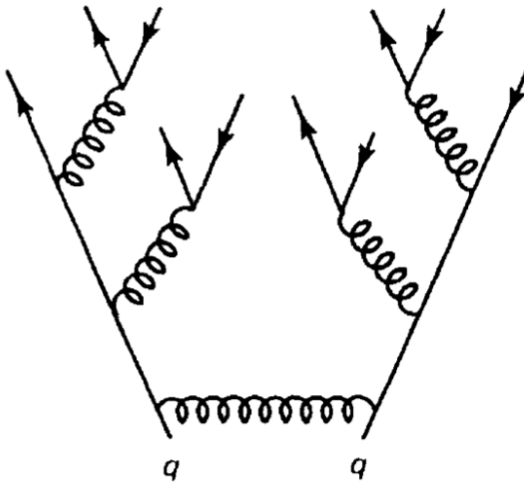


Figure 1.3: An example Feynmann diagram of jet production

³⁸⁷ **1.2 QCD and Jets**

³⁸⁸ While there is only one type of electric charge, there are three types of color charge; red, green,
³⁸⁹ and blue. In the process $q \rightarrow q + g$, the color of the quark can change. In order to conserve color
³⁹⁰ charge, gluons are bicolored, and always carry some positive color charge and some negative color
³⁹¹ charge.

³⁹² Color charged particles can only exist in bound states which result in a neutral total color
³⁹³ charge, a principle known as confinement. This requires that quarks and gluons exist in group
³⁹⁴ states known as hadrons; either mesons in the case of two quarks or baryons in the case of three
³⁹⁵ quarks. When a quark is separated from a hadron, confinement dictates that other colored objects
³⁹⁶ are produced around the quark to obey confinement. An example of this process is shown in
³⁹⁷ Figure 1.3. This ensemble of objects, generally a mixture of quarks and gluons, is termed a *jet*.
³⁹⁸ Jets are among the most common phenomenon observed by detectors at hadron colliders, and their
³⁹⁹ complex structure makes them a key focus of many physics analyses.

400 **1.3 Symmetries**

401 The Standard Model is a renormalizable quantum field theory that obeys the local symmetry

402 G_{SM} :

$$G_{SM} = SU(3)_C \times SU(2)_L \times U(1)_Y. \quad (1.1)$$

403 The $SU(3)_C$ symmetry component represents the non-Abelian gauge group of QCD. There
404 are 8 generators for the $SU_C(3)$ group which correspond to 8 types of gluon, each representing a
405 different superposition of color charge [3]. The $SU(2)_L \times U(1)_Y$ symmetry group represents the
406 electroweak sector of the Standard Model, which can be spontaneously broken into the electromag-
407 netic and weak sectors. There are 4 generators for this group, which correspond to four massless
408 gauge bosons W^1 , W^2 , W^3 , and B . From these massless gauge bosons are formed the massive
409 mediators of the weak force, the W^- , W^+ and Z^0 bosons, and the massless electromagnetic force
410 carrier, the photon γ . Spontaneous symmetry breaking and the process by which gauge bosons
411 acquire mass will be addressed in section 1.3.1.

412 Noether's theorem [4] stipulates that any continuous symmetry is associated with a conserved
413 quantity. In the Standard Model, this means that the $SU(3)_C$ symmetry gives rise to conservation of
414 color charge. The $SU(2)_L \times U(1)_Y$ symmetry gives rise to conservation of electromagnetic charge.
415 Conservation of spin results from the Poincaré symmetry described by the theory of special rela-
416 tivity, which combined with Noether's theorem gives us the conservation of energy, momentum,
417 and angular momentum.

418 The SM Lagrangian is invariant under CPT symmetry, or charge, parity, and time reversal.
419 Charge conjugation (C) transform a particle into its corresponding antiparticle by reversing the
420 charge and other quantum numbers. Parity conjugation (P) reverses spatial coordinates, which
421 transforms left-handed particles into right-handed particles and vice-versa. Time reversal (T) is
422 the theoretical process of reversing time. The L subscript in the $SU(2)_L$ group indicates that this
423 symmetry only applies to left-handed fermions. As a result, the $W^{1,2,3}$ gauge bosons of $SU(2)_L$

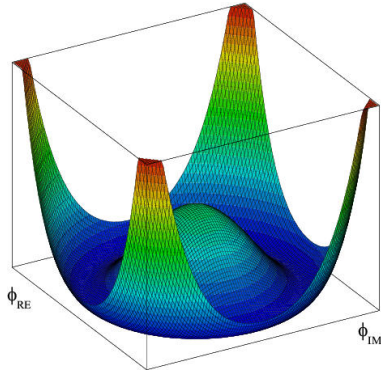


Figure 1.4: An illustration of the “hat shaped” potential of the Higgs field, resulting in a non-zero vacuum expectation value.

only interact with left handed particles, a process which maximally violates P-symmetry in the weak force. A small amount of the CP symmetry violation is also observed in the Standard Model, through the decays of strange flavored mesons [5] and b -mesons [6]. The CPT theorem posits that the violation of CP symmetry implies that T-symmetry must also be violated, so that CPT is a preserved symmetry.

1.3.1 Spontaneous Symmetry Breaking and The Higgs Mechanism

Spontaneous symmetry breaking is the process by which a Lagrangian obeys a symmetry at high energies, but exhibits asymmetric behavior at lower energies. The electroweak symmetry group is spontaneously broken as $SU(2)_L \times U(1)_Y \rightarrow U(1)_{EM}$. The quantity conserved by the $SU(2)_L$ symmetry is weak isospin $T_{1,2,3}$, while the quantity conserved by $U(1)_Y$ symmetry is weak hypercharge Y . Below very high energies, the presence of the Higgs field causes the electroweak symmetry to break. The Higgs field is a scalar field which forms a complex doublet of the $SU(2)$ symmetry group, with four degrees of freedom. The shape of the Higgs field potential, shown in Figure 1.4, results in a ground state with a non-zero vacuum expectation value; thus the Higgs field takes a non-zero value throughout all space, which breaks the symmetry of the weak isospin $SU(2)$ group.

The interaction with the Higgs field mixes the four massless gauge bosons $W^{1,2,3}$ and B . Three Higgs field degrees of freedom mix with the massless gauge bosons, resulting in three massive

442 gauge bosons W^- , W^+ and Z^0 . The massless photon γ is created from the components of the
443 massless gauge bosons which do not interact with the Higgs field. The scalar Higgs boson arises
444 from the one unmixed degree of freedom the Higgs field. Spontaneous symmetry breaking also
445 violates the conservation of weak isospin and weak hypercharge, leaving only electromagnetic
446 charge ($Q = T_3 + \frac{1}{2}Y$) as a conserved quantity associated with the $U(1)_{EM}$ symmetry.

447 1.4 Experimental Validation of the Standard Model

448 The theoretical framework of the Standard Model coalesced into a unified theory in the mid-
449 20th century. A cascade of discoveries providing empirical evidence for the model followed
450 closely. In the 1960s, three quarks (up, down and strange) and four leptons (electron, muon,
451 and their associated neutrinos) were the known particulate building blocks of matter and the Stan-
452 dard Model. The discovery of the charm quark in 1974, through the observation of the J/ψ meson
453 [7][8], confirmed the existence of a fourth quark flavor. The discovery of the τ in 1975 [9] provided
454 the first evidence of a 3rd generation of matter. This was quickly followed by the observation of
455 the Υ meson in 1977 [10], which provided evidence for the existence of a fifth quark, the b quark
456 (bottom, or beauty). The existence of a 3rd generation of fermion also explained the observation
457 of CP violation in the weak force, as it allowed for the addition of a complex phase in the CKM
458 matrix (a unitary matrix which describes flavor mixing in the weak interaction). The top quark
459 (t) and tau neutrino (ν_τ) were predicted at this point as the final building blocks of three complete
460 generations of fermions, and they were discovered by experimental observation around the turn of
461 the 21st century [11] [12] [13].

462 The W and Z bosons were predicted by the Standard Model, but to observe them required the
463 construction of a particle accelerator powerful enough to produce them. They were finally observed
464 at CERN in 1983 by the UA1 and UA2 experiments [14] [15] at the newly constructed Super Proton
465 Synchrotron (SPS). Their masses were observed to be compatible with the masses predicted by the
466 Standard Model nearly a decade earlier. The final missing piece then was confirming the existence
467 of the Higgs, which again required the construction of a newer and more powerful collider. CERN

468 achieved this with the construction of the Large Hadron Collider (LHC), and in 2012 the ATLAS
469 and CMS experiments announced the discovery of the Higgs particle [16] [17].

470 **1.5 Limitations of the Standard Model**

471 While the Standard Model has enjoyed decades of experimental results which confirm its pre-
472 dictions, there are several glaring shortcomings. The observed phenomenon for which the Standard
473 Model provides no explanation are summarized below.

- 474 • Gravity - the Standard Model does not account for the fourth fundamental force of gravity.
- 475 • Dark Matter - there is no viable candidate to explain the existence of dark matter, a non-
476 interacting form of matter which must exist to account for gravitational observations which
477 cannot be explained by general relativity, such as the motion of galaxies, gravitational lens-
478 ing, and the structure of the universe [18].
- 479 • Matter-Antimatter asymmetry - the level of CP violation in the Standard Model isn't suf-
480 ficient to explain the large discrepancy between the amount of matter and the amount of
481 antimatter in the universe today, and the origins of this imbalance are not understood.
- 482 • Neutrino masses - the Standard Model assumes that neutrinos are massless and provides
483 no mechanism for them to acquire mass. However, observations of neutrino oscillations
484 indicates they posses some small non-zero mass [19].

485 In addition to these unexplained natural phenomenon, there are several questions about the
486 *naturalness* of the Standard Model. The principle of naturalness states that dimensionless ratios
487 between physical constants should be of order 1, and that nature should not be arbitrarily fine-
488 tuned. While this is largely an aesthetic argument, it points to many aspects of the Standard Model
489 for which there exists no natural explanation.

- 490 • Strong CP - while CP symmetry is violated in the weak force, observations indicate that it
491 is preserved by the strong force [20]. The Standard Model predicts that CP violation in the

492 strong force is possible. There is no principle which motivates this incongruity between the
493 weak force and strong force.

- 494 • Hierarchy Problem - The wide range of masses for elementary particles and the wide range of
495 scales at which the four fundamental forces operate is not motivated by the SM. Specifically,
496 it is not understood why the Higgs mass is observed to be well below the Plank scale λ ,
497 which is the energy level at which the effects of quantum gravity become significant. QFT
498 indicates that the Higgs mass is determined by contributions from all energy scales including
499 λ , meaning that its observed mass is inexplicably small.

500 The limitations of the Standard Model provide a road map for theoretical and experimental
501 particle physicists, who seek to develop new theories which account for these observations, and
502 then to find evidence which might support these *Beyond the Standard Model* (BSM) theories. The
503 next chapter will introduce the BSM theories which motivate the physics search presented in this
504 thesis.

Chapter 2: Physics Beyond the Standard Model

507 In light of the various phenomenon unexplained by the Standard Model, physicists have pro-
 508 posed various extensions to the Standard Model, collectively termed *Beyond the Standard Model*
 509 (BSM) theories. A particular focus of the physics programs at the Large Hadron Collider (LHC)
 510 are BSM models which suggest dark matter candidate particles. If these particles couple to Stan-
 511 dard Model, they could be produced and observed at the LHC. This chapter will explore Hidden
 512 Valley models, and in particular the potential for Hidden Valley models to produce *semi-visible*
 513 *jets*. This will set the theoretical foundations for the experimental search presented in the later
 514 chapters of this thesis. The mechanisms of dark QCD that arise from these models and allow for
 515 the production of semi-visible jets will also be discussed.

516 **2.1 Hidden Valley Models**

517 Hidden Valley (HV) models are a category of BSM models that allow for dark matter (DM)
 518 production at the LHC. They extend the Standard Model with an additional non-Abelian gauge
 519 group [21]. This introduces the possibility of a complex dark sector, which mirrors the complexities
 520 of Standard Model QCD, and introduces the possibility of dark quarks and gluons. The term
 521 “hidden valley” refers to the idea that the DM is hidden from the SM by a high-energy barrier, as
 522 illustrated in Figure 2.1. The dark sector is assumed to communicate with the Standard Model via
 523 a “portal”, or “messenger particle”, that can interact with both Standard Model and HV forces. For
 524 the s-channel scenario, the portal is considered to be a new massive mediator particle Z' .

525 The portal particle allows for the production of dark sector particles at hadron colliders. If
 526 dark quarks are produced via the decay $Z' \rightarrow q_D q_D$ they can hadronize and form dark jets. The
 527 properties of the dark jets are determined by the dynamics of the dark sector, which are explored in

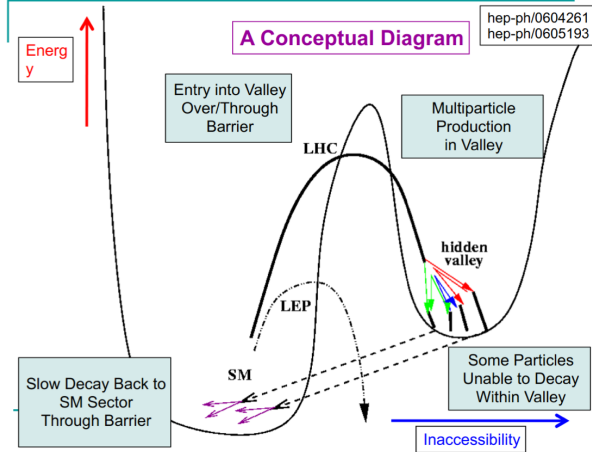


Figure 2.1: Illustration of the hidden valley potential.

528 the subsequent section. Depending on the details of the model, the jets formed by the dark hadrons
 529 can be categorized as fully dark, semi-visible, leptonic, emerging, or other [21].

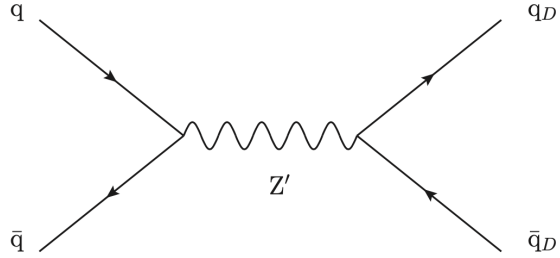


Figure 2.2: The massive mediator particle Z' of the s-channel realization of a HV model

530 2.2 Dark QCD

531 The theoretical underpinning of the semi-visible jet phenomenology is a dark sector with a
 532 gauge group $SU(N)_d$ leading to confinement at a scale Λ_d . For illustration, let's consider the
 533 case of an $SU(2)_d$ gauge theory, which gives rise to two dark fermionic generations $\chi_a = \chi_1, \chi_2$.
 534 Following the work of Ref [22] we can write the fundamental dark Lagrangian as:

$$\mathcal{L}_{dark} \supset -\frac{1}{2} \text{Tr} G_{\mu\nu}^d G^{d\mu\nu} - \bar{\chi}_a (i\cancel{D} - M_{d,a}) \chi_a \quad (2.1)$$

535 The first term allows for the dark gluons to self-interact, while the second term enables the dark
536 quarks to hadronize and acquire mass. The dark quarks are assumed to have a common mass M_d .

537 The coupling strength of the strongly interacting dark quarks is termed α_d . At the confinement
538 scale Λ_d , the dark quarks can form bound states. At the scale $M_d \approx \Lambda_d$ a QCD-like shower occurs.

539 The properties of the hadrons formed by the dark quarks are of particular importance to the
540 observed dark QCD dynamics. Dark-isospin number $U(1)_{1-2}$ and dark-baryon number $U(1)_{1+2}$
541 are accidental symmetries of the theory which determine the stability of the hadrons. In the case
542 of two dark flavors, six dark hadrons can be formed: four mesons ($\chi_1\bar{\chi}_1$, $\chi_2\bar{\chi}_2$, $\chi_1\bar{\chi}_2$, $\bar{\chi}_1\chi_2$) and
543 two baryons ($\bar{\chi}_1\bar{\chi}_2$, $\bar{\chi}_1\chi_2$). The mesons $\chi_1\bar{\chi}_2$ and $\bar{\chi}_1\chi_2$ are charged under dark-isospin and will be
544 stable if this symmetry is unbroken. The baryons would also be stable as they are charged under
545 the dark-baryon number. These four stable hadrons become dark matter candidates of the theory.

546 The $\chi_1\bar{\chi}_1$ and $\chi_2\bar{\chi}_2$ mesons are not charged under either symmetry and are thus expected to decay.
547 The unstable mesons can decay into stable dark mesons, or into an off-shell Z' . The off-shell Z'
548 will then decay into two DM quarks or two SM quarks, and its products will continue to shower
549 until the final state particles are stable.

550 The number of stable and unstable dark states varies substantially depending on the details
551 of the model. The model discussed above can be generalized from $SU(2)_d$ to $SU(N)_d$, with any
552 number of colors N_c or flavors N_f . This affects the ratio of possible stable to unstable mesons,
553 which can directly impact the amount of missing energy. The fraction of missing energy is a
554 variable in many dark QCD models, and is especially important in the case of semi-visible jets.

555 2.3 Semi-visible Jets

556 A “semi-visible jet” occurs when the heavy Z' messenger particle decays into dark quarks,
557 which then hadronize in a QCD-like shower. If some of the dark hadrons are stable while others
558 decay to SM quarks via the off-shell Z' , a collimated mixture of visible and dark matter is formed
559 – this is termed a semi-visible jet. If the Z' messenger particle is produced at rest, the two jets will
560 be back-to-back in the transverse plane. If there is an imbalance in the amount of invisible particles

561 between the two jets, one of the jets will be observed to be aligned with missing transverse energy.

562 While there are a myriad of HV and dark QCD models, a handful of model parameters are most
563 important in determining the observable of these showers within a particle detector. The coupling
564 strength α_d is one of the most important, as it controls the fraction of dark hadrons emitted in the
565 shower and their average p_T . The mass of the dark quarks directly impacts the jet mass. If the
566 masses of the dark quark flavors are comparable, the ratio of stable to unstable dark hadrons will
567 be approximately 1:1. However, if there is a mass splitting, stable or unstable dark hadrons may
568 be favored, which impacts the amount of missing energy observed.

569 The ratio of stable to unstable dark hadrons in the shower is a critical variable for capturing the
570 behavior of dark showers. This value is termed R_{inv} :

$$R_{inv} = \frac{\# \text{ of stable hadrons}}{\# \text{ of hadrons}} \quad (2.2)$$

571 Events containing jets aligned with missing transverse momentum are generally considered to
572 be misreconstructed by other DM searches, and therefore discarded. This class of final states is
573 therefore largely uncovered by existing DM searches. The nature of the dark hadron shower is
574 determined by the following parameters: the Z' mass $m_{Z'}$, the Z' couplings to visible and dark
575 quarks g_q and g_{q_D} , the number of dark colors and flavors, the characteristic scale of the dark sector
576 confinement Λ_D , the mass scale of the dark hadrons m_D , and the average fraction of stable hadrons
577 in the decay R_{inv} . The coupling to SM quarks determines the Z' production cross section.

578

Part II

579

Experiment

Chapter 3: The Large Hadron Collider

582 The Large Hadron Collider (LHC) is a 26.7 km circular high-energy particle accelerator, span-
583 ning the Swiss-French border near the city of Geneva, Switzerland [23]. The LHC occupies the
584 tunnel constructed in 1989 for the Large Electron-Positron (LEP) Collider, and reaches a maxi-
585 mum depth of 170m below the surface. The LHC is operated by the European Organization for
586 Nuclear Research (CERN), the largest international scientific collaboration in the world.

587 The LHC accelerates protons and heavy ions, and collides them at four interaction points
588 around the ring, with a design center-of-mass energy per collision of $\sqrt{s} = 14$ TeV. Each interaction
589 point is home to one of four detector experiments, which study the products of the collisions. The
590 largest of these experiments is the ATLAS detector, a general purpose detector designed to study
591 the Standard Model and search for new physics that could be produced in LHC collisions [24].
592 The CMS detector is another general purpose detector, designed and operated independently of the
593 ATLAS detector, but intended to probe the same range of physics [25]. The ALICE experiment is
594 a dedicated heavy ion experiment, and the LHC-b experiment is a dedicated *b*-physics experiment
595 [26] [27].

596 This chapter will cover the multi-component accelerator complex powering the LHC, the state-
597 of-the-art magnets which steer the particle beams, measurements of the intensity and number of
598 collisions produced by the LHC, and finally an overview of LHC activities in the past, present, and
599 future.

600 **3.1 Accelerator Physics**

601 **3.1.1 The Journey of a Proton**

602 From 2010 - 2018, the protons which fed the LHC started as hydrogen gas. The electrons were
603 removed from the hydrogen atoms through the use of strong electric fields. The linear accelerator
604 LINAC2 then accelerated the protons to an energy of 50 MeV. Between 2018 and 2020, LINAC2
605 was replaced with LINAC4, which instead accelerates H^- ions, hydrogen atoms with two electrons.
606 LINAC4 is capable of accelerating the H^- ions to 160 MeV. Before injection to the next part of
607 the acceleration chain, both electrons are stripped from the H^- ions, leaving just protons. From
608 here the protons enter the Proton Synchrotron booster, where they are accelerated up to 1.4 GeV of
609 energy. Subsequently they are sorted into bunches separated in time by 25 ns, where each bunch
610 contains approximately 10^{11} protons. Next the bunches pass through the Proton Synchrotron (PS)
611 and the Super Proton Synchrotron (SPS), where they reach energies of 25 GeV and 450 GeV
612 respectively. Finally they are injected into the LHC as two beams traveling in opposite direction.
613 The original design allowed each beam to be accelerated up to 7 TeV of energy. Due to limitations
614 in the performance of the superconducting LHC magnets, the highest energy actually achieved by
615 the LHC beams during Run 2 was 6.5 TeV, giving a collision center-of-mass energy of $\sqrt{s} = 13$
616 TeV [28]. Figure 3.1 shows the full LHC accelerator complex.

617 Acceleration in the LHC is performed by eight radio frequency (RF) cavities located around the
618 ring. Each RF cavity produces a 2 MV electric field oscillating at 40 MHz. The 40MHz oscillation
619 produces a point of stable equilibrium every 2.5 ns. These points of equilibrium are synchronized
620 with the occurrence of the proton bunches produced in the PS – a proton bunch occupies one out
621 of every ten points of stable equilibrium, such that the bunches maintain a 25 ns spacing [28].

622

The CERN accelerator complex Complexe des accélérateurs du CERN

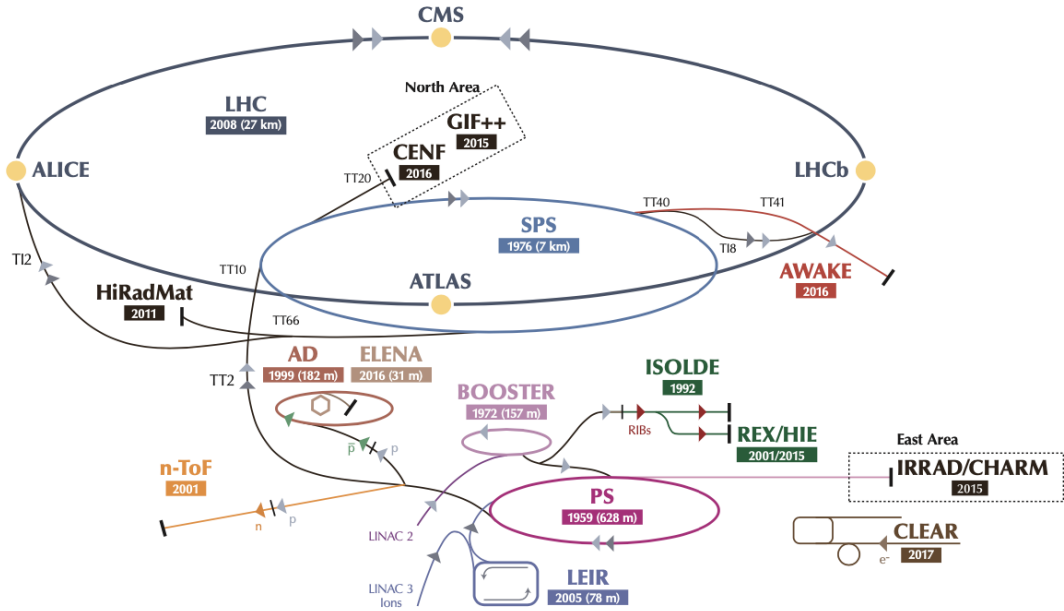


Figure 3.1: The LHC accelerator complex at CERN [29]

623 3.1.2 Magnets

624 In addition to the acceleration cavities, the LHC houses 9593 superconducting magnets which
 625 direct and focus the proton beam on its 27 kilometer journey. The magnets are comprised of super-
 626 conducting Niobium-Titanium coils cooled to 1.9K by superfluid helium. As the beams approach
 627 one of the four collision points around the ring, multipole magnets focus and squeeze the beam for
 628 optimal collisions [28].

629 The LHC is divided into sections, where each section contains an arc and a straight insertion. The arcs are composed of 1232 large dipole magnets which bend the beam
 630 to follow the roughly circular 27 km path. The main dipoles generate powerful 8.3 tesla magnetic
 631 fields to achieve this bend. Each dipole magnet is 15 meters long and weighs 35 tonnes. The
 632 dipoles work in conjunction with quadrupole magnets, which keep the particles in a focused beam,
 633 and smaller sextupole, octupole and decapole magnets which tune the magnetic field at the ends of
 634 the dipole magnets [30].

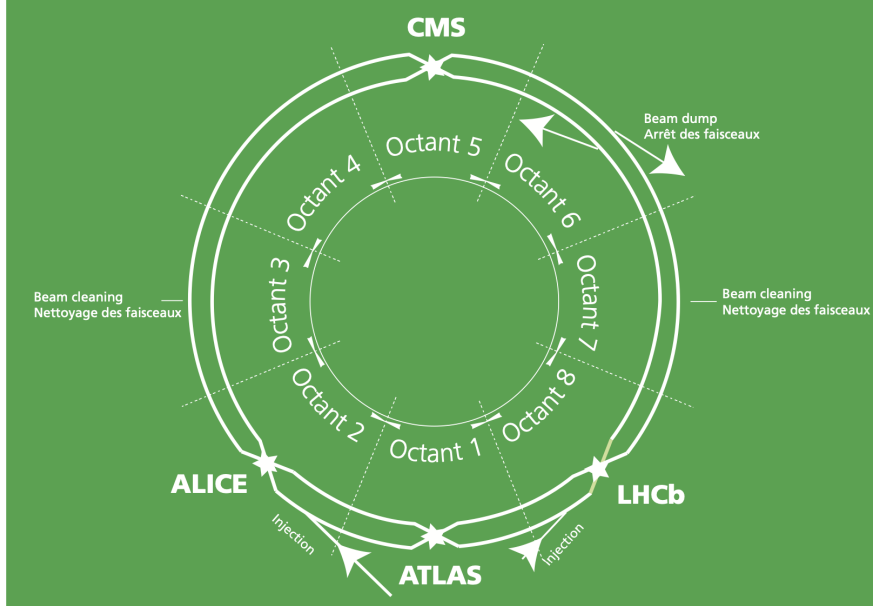


Figure 3.2: The octants of the LHC and location of various beam activities [28]. Stars indicate the locations of beam collisions, and the associated detectors recording the outcome of those collisions.

636 The straight insertion sections have different purposes depending on their location around the
 637 ring: beam collisions, beam injection, beam dumping, or beam cleaning. At the four collision
 638 points, insertion magnets squeeze the beam to ensure a highly focused collision. This is accom-
 639 plished with a triplet of quadrupole magnets, which tighten the beam from 0.2 millimeters to just
 640 16 micrometers in diameter. Insertion magnets also clean the beam, which prevents stray particles
 641 from hitting sensitive components throughout the LHC. When the LHC is ready to dispose of a
 642 beam of particles, beam dump magnets deflect the path of the beam into a straight line towards
 643 a block of concrete and graphite that stops the beam. A dilution magnet then reduces the beam
 644 intensity by a factor of 100,000 before the final stop [30]. Figure 3.2 shows the locations various
 645 beam activities.

646 3.2 Luminosity

647 Collisions at the LHC occur when the two beams of proton bunches cross at one of the four
 648 interaction points. The intensity of collisions is described by the instantaneous luminosity, the

649 formula for which is given in equation 3.1.

$$L = \frac{fN_1N_2}{4\pi\sigma_x\sigma_y} \quad (3.1)$$

650 Here f is the revolution frequency, N_1 and N_2 are the number of particle per bunch for each
651 beam, and σ_x , σ_y are the horizontal and vertical beam widths.

652 The instantaneous luminosity gives the number of the collisions that could be produced at the
653 interaction point per unit of cross-sectional area per unit of time, generally expressed in $\text{cm}^{-2}\text{s}^{-1}$.
654 The integrated luminosity is obtained by integrating the instantaneous luminosity over a given
655 block of time, and measures the total number of collisions which have occurred during that op-
656 eration period. The total integrated luminosity is directly correlated with the size of the datasets
657 collected by the LHC experiments. Total integrated luminosity for Run 2 is illustrated in Figure
658 3.3.

659 High levels of instantaneous luminosity result in multiple pp collisions per bunch crossing,
660 which leads to an effect known as *pileup*. Pileup poses a challenge for detector physics, as recon-
661 structing the products of multiple simultaneous events is far more challenging than reconstructing
662 a single event with no pileup. Pileup conditions vary from year-to-year and run-to-run of LHC op-
663 eration, and the impact of these conditions are taken into account when analyzing the data, as will
664 be discussed further in Chapter 5. Measurement of pileup conditions during Run 2 are illustrated
665 in Figure 3.3.

666 The design peak luminosity of the LHC is $1.0 \times 10^{34} \text{ cm}^{-2}\text{s}^{-1}$. During Run 1 of the LHC the
667 peak instantaneous luminosity was $0.8 \times 10^{34} \text{ cm}^{-2}\text{s}^{-1}$. Over the course of Run 1 the LHC collected
668 a total integrated luminosity of 5.46 fb^{-1} at $\sqrt{s} = 7 \text{ TeV}$, and 22.8 fb^{-1} at $\sqrt{s} = 8 \text{ TeV}$. Following the
669 first long shutdown and upgrade phase of operations, the LHC achieved a center of mass energy
670 $\sqrt{s} = 13 \text{ TeV}$ at the beginning of Run 2 in 2015. The LHC was also able to deliver 2.0×10^{34}
671 $\text{cm}^{-2}\text{s}^{-1}$ peak instantaneous luminosity, double the design value. During LHC Run 2, from 2015-
672 2018, the LHC delivered 156 fb^{-1} of integrated luminosity for proton-proton collisions. Run 3 of

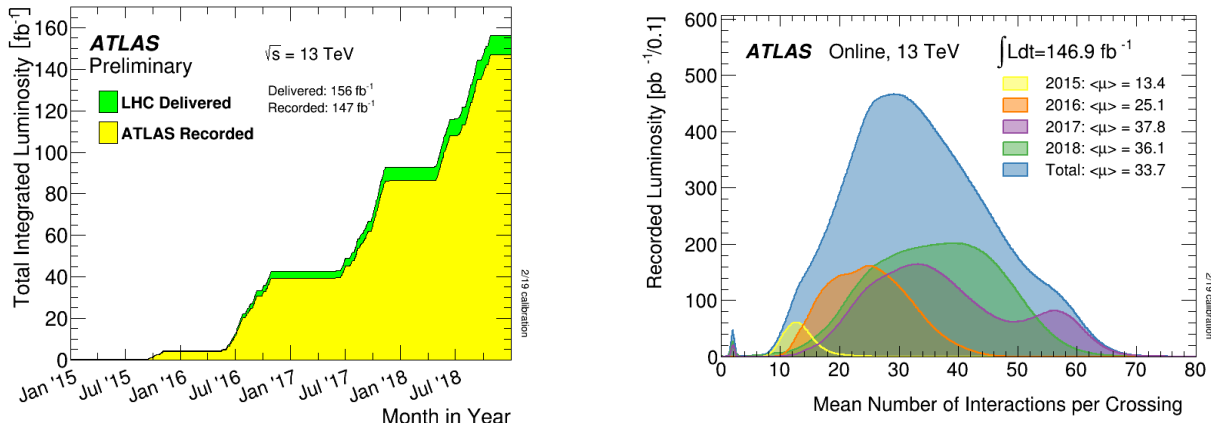


Figure 3.3: (Left) Total integrated luminosity over the course of Run 2. (Right) Average number of pp interactions per bunch crossing in Run 2. Each curve is weighted by the integrated luminosity for the year.

673 the LHC began in 2022, and is expected to deliver 250 fb^{-1} of integrated luminosity to the ATLAS
 674 and CMS experiments by 2026 [31].

675 The goal of LHC physic analyses is to find and study rare events produced by interesting
 676 physics processes. The cross section σ of a given process indicates the probability of that process
 677 occurring given the beam conditions of the LHC. Multiplying the cross section by the integrated
 678 luminosity of a dataset gives the expected number of events for that process within the dataset.

$$N_{\text{events}} = \int \sigma L(t) dt = \mathcal{L} \times \sigma \quad (3.2)$$

679 The cross section for most processes of interest, especially BSM processes, is several orders of
 680 magnitude below the total cross section for the LHC. Therefore maximizing the number of events
 681 produced in collisions is crucial to increase the likelihood of producing events from processes of
 682 interest. For this reason, maximizing instantaneous luminosity is a key factor in accelerator design
 683 and operation, while mitigating the resulting pileup effects is a key component in detector design
 684 and operation.

685 **3.3 LHC Timeline**

686 The first proton-proton collisions at the LHC were achieved in 2010 with a center-of-mass
687 energy of $\sqrt{s} = 7$ TeV. Run 1 of the LHC took place between 2010 and early 2013, during which
688 time the center-of-mass collision energy increased from 7 TeV to 8 TeV. Figure 3.4 shows an
689 overview of LHC activities beginning in 2011, in the midst of Run 1. The data collected during
690 Run 1 led to the discovery of the Higgs Boston in 2012 [32].

691 Between 2013 and 2015 the LHC underwent the first Long Shutdown (LS1) during which
692 time maintenance and renovation was performed on the accelerator chain, including the repair and
693 consolidation of the high-current splices which connect the super-conducting LHC magnets. Run
694 2 of the LHC took place from 2015 to 2018 and achieved a center-of-mass energy of $\sqrt{s} = 13$ TeV.
695 Analysis of data collected in Run 2 is still on going, and is the subject of study in this thesis.

696 Between 2018 and 2022 the LHC underwent the second Long Shutdown (LS2), allowing for
697 further detector and accelerator maintenance and upgrades. Key improvements to the LHC in-
698 cluded the improvement of the insulation for over 1200 diode magnets, and the upgrade from
699 LINAC2 to LINAC4 mentioned in Section 3.1.1. Run 3 of the LHC began in 2022 and achieved a
700 center-of-mass energy of $\sqrt{s} = 13.6$ TeV.

701 Run 3 is scheduled to continue through 2026, at which point the LHC machine and detectors
702 will undergo upgrades for the *high luminosity* LHC (HL-LHC). The HL-LHC will increase the
703 instantaneous machine luminosity by a factor of 5 - 7.5 with respect to the nominal LHC design.
704 The bottom panel of Figure 3.4 shows an overview of the preparation work for the HL-LHC that
705 has been going on concurrently with Run 1, 2, and 3 of the LHC [33].



Figure 3.4: Timeline of LHC and HL-LHC activities [31]. Integrated luminosity estimates are approximate, and not reflective of the exact amount delivered to each experiment.

Chapter 4: The ATLAS Detector

708 The ATLAS detector (**A** Toroidal **L**H**C** Apparatu**S**) is one of two general purpose physics
 709 detectors designed to study the products of proton-proton collisions at the LHC. The detector is
 710 composed of a variety of specialized subsystems, designed to fully capture a wide array of physics
 711 processes. The apparatus is 25m high, 44m in length, and weighs over 7000 tons [34]. The LHC
 712 beam pipes direct proton beams to an interaction point at the center of ATLAS, and the cylindrical
 713 detector design captures a complete 360° view of the *event*, tracking all particles that result from
 714 the collision.

715 The main components of the ATLAS detector are the Inner Detector (ID) which provides high
 716 precision tracking of charged particles leaving the collision vertex, the calorimeter system which
 717 measures the energy of electromagnetic and hadronic objects, and the Muon Spectrometer (MS)
 718 which gives detailed information about muons that reach the outer radii of the detector. Two
 719 magnet systems, a 2 T solenoid magnet surrounding the ID, and a 0.5-1.0 T toroid magnet system
 720 situated throughout the MS, produce magnetic fields which bend the trajectory of charged particles
 721 traversing the detector. In addition to the main detector components, dedicated forward detectors
 722 monitor beam conditions and instantaneous luminosity, and an online trigger system reduces the
 723 data rate to a manageable level for storage. Each of these components will be discussed in further
 724 detail in this chapter.

725 4.1 Coordinate System and Geometry

726 The ATLAS detector employs a right hand cylindrical coordinate system. The z axis is aligned
 727 with the beam line, and the x-y plane sits perpendicular to the beam line. The coordinate system
 728 origin is centered on the detector, such that the origin corresponds with the interaction point of the

729 two colliding beams. The detector geometry is usually characterized by polar coordinates, where
730 the azimuthal angle ϕ spans the x-y plane. The polar angle θ represents the angle away from the
731 beam line, or z axis. $\theta = 0$ aligns with the positive z -axis, and $\phi = 0$ aligns with the positive x-axis.

732 The polar coordinate θ is generally replaced by the Lorentz invariant quantity *rapidity* or y :

$$y = \frac{1}{2} \ln\left(\frac{E + p_z}{E - p_z}\right). \quad (4.1)$$

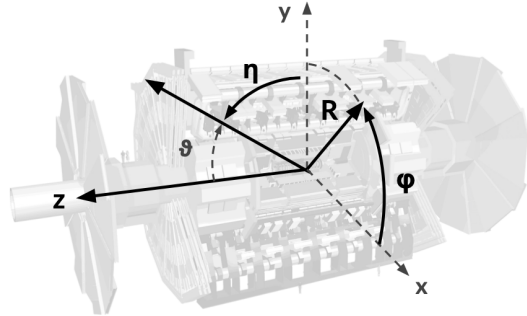
733 This substitution is advantageous because objects in the detector are traveling at highly rela-
734 tivistic speeds. The relativistic speed also means that the masses of the particles are generally small
735 compared to their total energy. In the limit of zero mass, the rapidity y reduces to the pseudorapid-
736 ity η , which can be calculated directly from the polar angle θ :

$$\eta = -\ln\left(\frac{\theta}{2}\right). \quad (4.2)$$

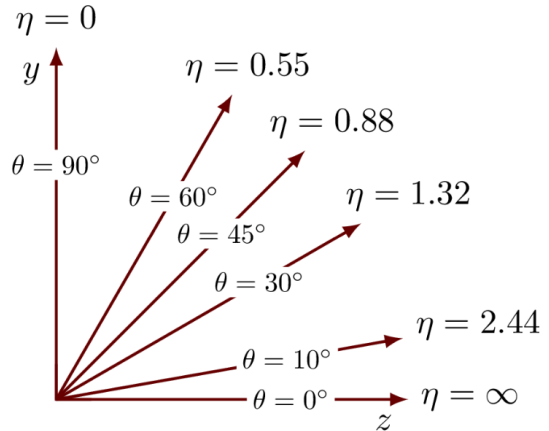
737 The distance between physics objects in the detector is generally expressed in terms of the solid
738 angle between them ΔR :

$$\Delta R = \sqrt{\Delta\phi^2 + \Delta\eta^2} \quad (4.3)$$

739 Figure 4.1a depicts the orientation of the coordinate system with respect to the ATLAS detector,
740 while Figure 4.1b illustrates the relationship between θ , η , and the beamline axis z . Direct or “head
741 on” proton-proton collisions are more likely to result in objects whose momentum is directed
742 along transverse plane (low $|\eta|$); glancing proton-proton collisions are more likely to result in
743 objects whose momentum is directed along the z -axis (high $|\eta|$). Due to the difference in the
744 nature of these collisions, as well as the cylindrical design of the ATLAS detector, the detector
745 is divided into regions of low and high η . Each subsystem has a “central” or “barrel” region
746 covering low $|\eta|$, while the “forward” or “end-cap” regions cover the area up to $|\eta| = 4.9$. Each of
747 the three main ATLAS subsystems will be discussed in the following sections.



(a) The ATLAS geometry



(b) Relationship between η and θ

Figure 4.1: ATLAS coordinate system and geometry

748 4.2 Inner Detector

749 The Inner Detector (ID) is the ATLAS subsystem closest to the interaction point. The primary
 750 purpose of the ID is to determine the charge, momentum, and trajectory of charged particles pass-
 751 ing through the detector. With this information the ID is also able to precisely determine interaction
 752 vertices.

753 The ID is composed of three sub-detectors; the Pixel Detector, the Semiconductor Tracker
 754 (SCT) and the Transition Radiation Tracker (TRT). Figure 4.2 shows the location of these three
 755 subsystems with respect to each other and the interaction point.

756 4.2.1 Pixel Detector

757 The pixel detector is the first detector encountered by particles produced in LHC collisions.
 758 The original pixel detector consists of 3 barrel layers of silicon pixels, positioned at 5 cm, 9 cm
 759 and 12 cm from the beamline. There are also 3 disks on each end-cap positioned 50 - 65 cm from
 760 the interaction point, providing full coverage for $|\eta| < 2.2$. The layers are comprised of silicon
 761 pixels each measuring $50 \times 400 \mu\text{m}^2$, with 140 million pixels in total. The pixels are organized
 762 into modules, which each contain a set of radiation hard readout electronics chips. In 2014, the
 763 Insertable B-layer (IBL) was installed, creating a new innermost layer of the pixel detector sitting

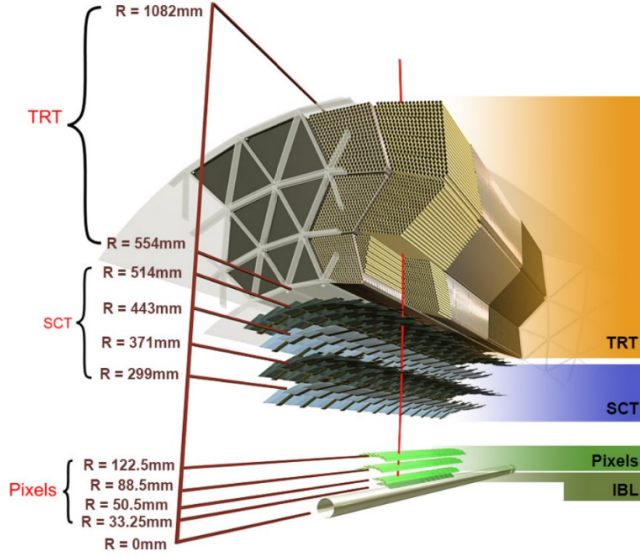


Figure 4.2: A 3D visualization of the structure of the ID in the barrel region [35]

764 just 3.3 cm from the beamline. The pixels of the IBL measure $50 \mu\text{m}$ by $250 \mu\text{m}$, and cover
 765 a pseudo-rapidity range up to $|\eta| < 3$. The IBL upgrade enhances the pixel detector's ability
 766 to reconstruct secondary vertices associated with short-lived particles such as the b-quark. The
 767 improved vertex identification also helped compensate for increasing pile-up in Run 2 [34].

768 4.2.2 Semiconductor Tracker

769 The SCT provides at least 4 additional measurements of each charged particle. It employs the
 770 same silicon technology as the Pixel Detector, but utilizes larger silicon strips which measure $80 \mu\text{m}$
 771 by 12.4 cm . The SCT is composed of 4 barrel layers, located between 30 cm and 52 cm from
 772 the beamline, and 9 end-cap layers on each side. The SCT can distinguish tracks that are separated
 773 by at least $200 \mu\text{m}$.

774 4.2.3 Transition Radiation Tracker

775 The TRT provides an additional 36 hits per particle track. The detector relies on gas filled
 776 straw tubes, a technology which is intrinsically radiation hard. The straws which are each 4 mm in
 777 diameter and up to 150 cm in length and filled with xenon gas. The detector is composed of about

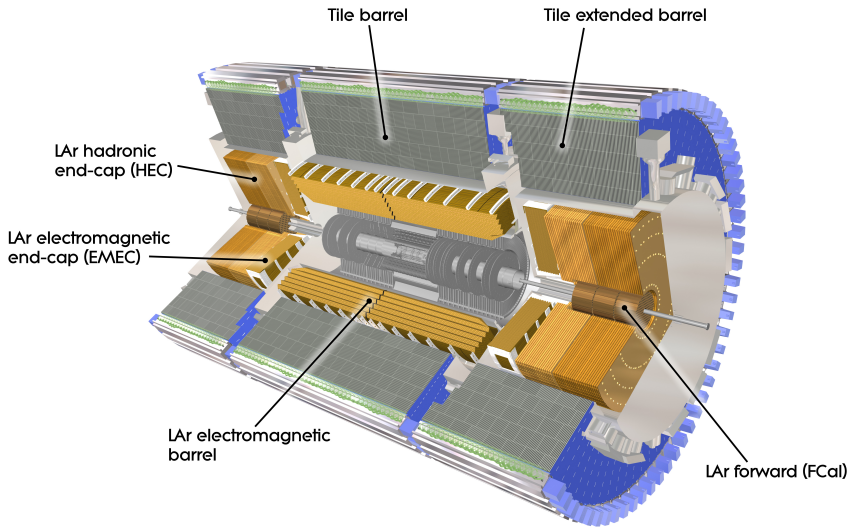


Figure 4.3: ATLAS calorimetry system [36]

778 50000 barrel region straws and 640000 end-cap straws, comprising 420000 electronic readout
 779 channels. Each channel provides a drift time measurement with a spatial resolution of $170\ \mu\text{m}$ per
 780 straw. As charged particles pass through the many layers of the detector, transition radiation is
 781 emitted. The use of two different drift time thresholds allows the detector to distinguish between
 782 tracking hits and transition radiation hits.

783 4.3 Calorimeters

784 The ATLAS calorimeter system is responsible for measuring the energy of electromagnetically
 785 interacting and hadronically interacting particles passing through the detector. The calorimeters are
 786 located just outside the central solenoid magnet, which encloses the inner detectors. The calorime-
 787 ters also stop most known particles, which the exception of muons and neutrinos, preventing them
 788 from traveling to the outermost layers of the detector. The ATLAS calorimetry system is composed
 789 of two subsystems - the Liquid Argon (LAr) calorimeter for electromagnetic calorimetry and the
 790 Tile calorimeter for hadronic calorimetry. The full calorimetry system is shown in Figure 4.3.

791 4.3.1 Liquid Argon Calorimeter

792 The LAr calorimeter is a sampling calorimeter designed to trigger on and measure the ener-
793 gies of electromagnetic (EM) particles, as well as hadronic particles in the high η regions. It is
794 divided in several regions, as shown in Figure 4.3. For the region $|\eta| < 1.4$, the electromagnetic
795 barrel (EMB) is responsible for EM calorimetry, and provides high resolution energy, timing,
796 and position measurements for electrons and photons passing through the detector. The elec-
797 tromagnetic endcap (EMEC) provides additional EM calorimetry up to $|\eta| < 3.2$. In the re-
798 gion $1.4 < |\eta| < 3.2$, the hadronic endcap (HEC) provides hadronic calorimetry. For hadronic
799 calorimetry in the region $|\eta| < 1.4$, corresponding to a detector radii > 2.2 m, the less expensive
800 tile calorimeter (discussed in the next section) is used instead. A forward calorimeter (FCAL)
801 extends the hadronic calorimetry coverage up to $3.1 < |\eta| < 4.8$ [37].

802 The LAr calorimeter is composed of liquid argon sandwiched between layers of absorber mate-
803 rial and electrodes. Liquid argon is advantageous as a calorimeter active medium due to its natural
804 abundance and low cost, chemical stability, radiation tolerance, and linear response over a large
805 energy range [38]. The calorimeter is cooled to 87k by three cryostats: one barrel cryostat encom-
806 passing the EMB, and two endcap cryostats. The barrel cryostat also encloses the solenoid which
807 produces the 2T magnetic field for the inner detector. Front-end electronics are housed outside the
808 cryostats and are used to process, temporarily store, and transfer the calorimeter signals.

809 **Electromagnetic Calorimeter**

810 For the electromagnetic calorimeters, the layers of electrodes and absorber materials are ar-
811 ranged in an an accordion shape, as illustrated in Figure 4.4. The accordion shape ensures that
812 each half barrel is continuous in the azimuthal angle, which is a key feature for ensuring consistent
813 high resolution measurements. Liquid argon permeates the space between the lead absorber plates,
814 and a multilayer copper-polymide readout board runs through the center of the liquid argon filled
815 gap.

816 The detection principle for the LAr calorimeter is the current created by electrons which are

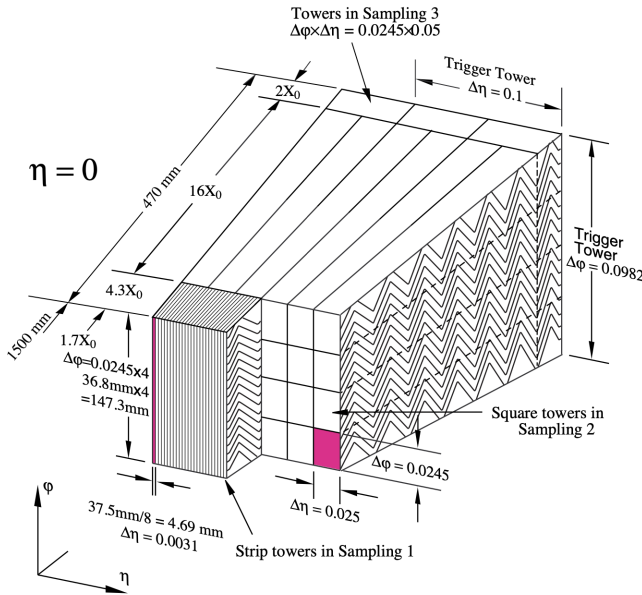


Figure 4.4: Diagram of a segment of the EMB, demonstrating the accordion plate arrangement [37]

817 released when a charged particle ionizes the liquid argon. In the barrel region, the electrons are
 818 driven towards the center electrodes by a 2000 V potential with a drift time of less than 450 ns [39].
 819 In the end-caps the voltage varies as a function of the radius in order to maintain a flat response
 820 [37]. The amount of current produced by the ionized electrons is proportional to the energy of
 821 the particle creating the signal. Figure 4.5 shows the shape of the signal produced in the LAr
 822 calorimeter, before and after it undergoes shaping during the readout process. The shaping of the
 823 pulse enforces a positive peak and a negative tail, which ensures that subsequence pulses can be
 824 separated with the precision required for the 25 ns LHC bunch spacing [37].

825 Hadronic End-cap Calorimeter

826 The HEC sits radially beyond the EMEC. The copper absorber plates in the HEC are oriented
 827 perpendicular to the beamline, with LAr as the active medium. Each end-cap is divided into two
 828 independent wheels; the inner wheel uses 25 mm copper plates, while the outer wheel uses 50 mm
 829 plates as a cost saving measure. In each wheel, the 8.5 mm plate gap is crossed by three parallel

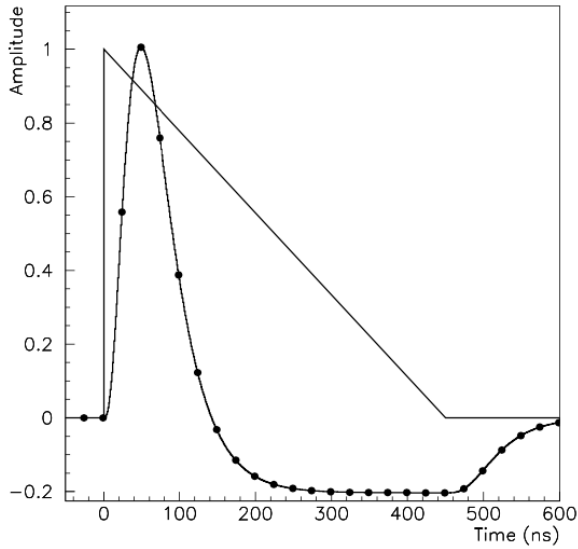


Figure 4.5: A LAr pulse as produced in the detector (triangle) and after shaping (curve) [37]

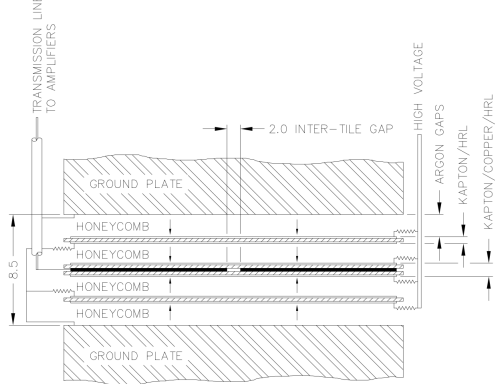


Figure 4.6: Readout gap structure in HEC [37]

830 electrodes, creating an effective drift distance of 1.8 mm. This gap is illustrated in Figure 4.6.
 831 Each wheel is divided into 32 wedge-shaped modules, each containing their own set of readout
 832 electronics.

833 **Forward Calorimeter**

834 The forward range is covered by the FCal, which provides both EM and hadronic calorimetry.
 835 It is composed of three active cylindrical modules; one EM module with copper absorber plates,
 836 and two hadronic modules with tungsten absorber plates. The plates are oriented perpendicular to

837 the beamline, and LAr is used as the active material throughout. The electrodes of the FCal consist
838 of tubes that run parallel to the beam line, arranged in a honeycomb pattern. The resulting LAr
839 gaps are as small as $250\ \mu\text{m}$, which enables the FCal to handle the large influx of particles in the
840 forward region [37].

841 4.3.2 Tile Calorimeter

842 The Tile Calorimeter (TileCal) provides hadronic calorimetry in the region $\eta < 1.7$, and sur-
843 rounds the LAr calorimeter. It is responsible for measurements of jet energy and jet substructure,
844 and also plays an important role in electron isolation and triggering (including muons) [40]. Tile-
845 Cal is composed of 3 sections, as shown in Figure 4.3; a barrel calorimeter sits directly outside the
846 LAr EMB and provides coverage up to $\eta < 1.0$. Two extended barrel sections sit outside the LAr
847 endcaps and cover the region $0.8 < \eta < 1.7$.

848 TileCal is a sampling calorimeter composed of steel and plastic scintillator plates as illustrated
849 in Figure 4.7. A total of 460,000 scintillators are read out by wavelength-shifting fibers. The
850 fibers are gathered to define cells and in turn read out by photomultiplier tubes, which amplify
851 the signal and convert it to an electrical signature. Each cell has an approximate granularity of
852 $\Delta\eta \times \Delta\phi = 0.1 \times 0.1$. Each barrel is divided azimuthally into 64 independent modules, an example
853 of which is show in Figure 4.7. The modules are each serviced by front-end electronic housed in a
854 water-cooled drawer on the exterior of the module.

855 The detection principle of the TileCal is the production of light from hadronic particles inter-
856 acting with the scintillating tiles. When a hadronic particle hits the steel plate, a shower of particles
857 are produced. The interaction of the shower with the plastic scintillator produces photons, the num-
858 ber and intensity of which are proportional to the original particle's energy.

859

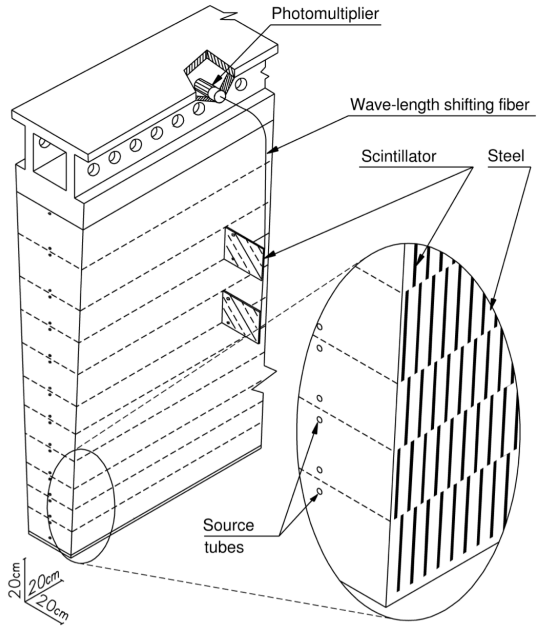


Figure 4.7: TileCal wedge module [40]

860 4.4 Muon Spectrometer

861 Unlike electrons, photons, and hadrons, muons interact minimally with the ATLAS calorime-
 862 ters, and can pass through large amounts of detector material without stopping. The ATLAS Muon
 863 Spectrometer (MS) provides additional tracking information to improve the identification and mea-
 864 surement of muons. The MS comprises the outermost layers of the detector, and is interspersed
 865 with toroid magnets (discussed in Section 4.5), which provide a magnetic field of approximately
 866 0.5 T. The magnetic field bends the trajectory of the muons as they pass through the detector, and
 867 the degree of the bend is directly correlated with the muon momentum. The path of the muon is
 868 primarily measured by hits in three layers of Monitored Drift Tube (MDT) precision chambers,
 869 which cover the range $|\eta| < 2.7$. The barrel layout of the MS is show in Figure 4.8.

870 Muon triggering is provided by three layers of Resistive Plate Chambers (RPC) in the barrel
 871 ($|\eta| < 1.05$), and 3 - 4 layers of Thin Gap Chambers (TGC) in the end-caps ($1.05 < |\eta| < 2.4$).
 872 RPCs and TGCs also provide muon track measurements in the non-bending coordinate (ϕ). RPCs
 873 are constructed from two parallel resistive plates separated by a 2mm gap filled with a sensitive

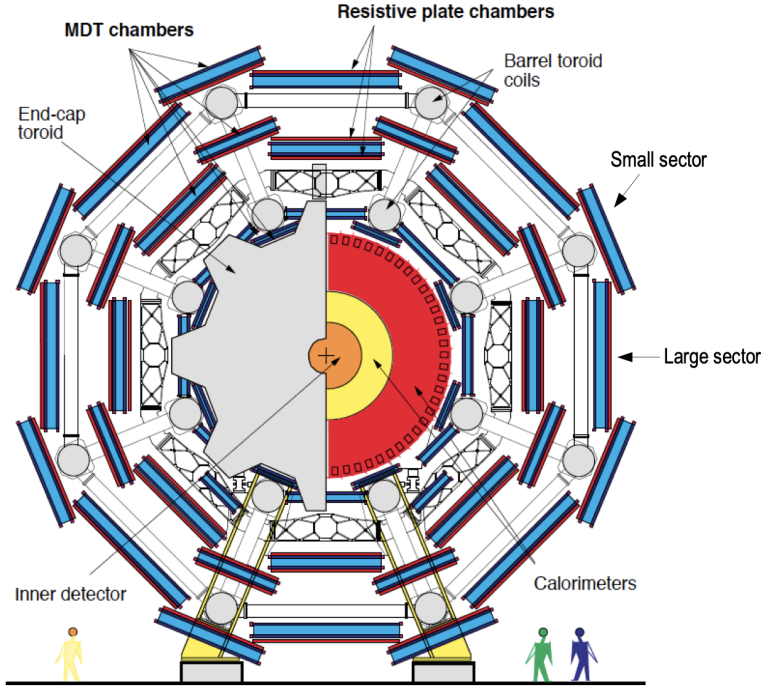


Figure 4.8: Cross section view of the muon spectrometer system [41]

gas mixture. This provides a total of six independent measurements for each muon track, with a spatial resolution of ~ 1 cm and a time resolution of ~ 1 ns. Time measurements from the RPCs are primarily associated to hits in the MDT precision chambers to determine the bunch crossing. The time measurement is also used to reject cosmic muons, and to search for delayed signals. TCGs provide triggering in the end-cap regions, and consist of parallel $30\ \mu\text{m}$ wires suspended in a sensitive gas mixture. TCGs provide high radiation tolerance and a fast response time, both features that are necessary for handling the high flux of muons in the forward region [41].

Precision measurements of muon momentum and position are primarily achieved by MDTs. The MDTs are constructed from 30 mm diameter tubes, permeated by a gas mixture of 93% Ar and 7% CO₂. The average single-tube spatial resolution is $80\ \mu\text{m}$. Each chamber consists of six drift tube layers, which together provide a muon track segment resolution of $35\ \mu\text{m}$. The momentum of the muons can be calculated from the bend in the muon trajectory as they pass through the 0.5T magnetic field provided by the toroids. For a $p_T = 1$ TeV track, the average p_T resolution is 11%. In the inner most end-cap wheels, Cathode Strip Chambers (CSC) are used instead of MDTs,

888 covering the region $2.0 < |\eta| < 2.7$. CSCs are multi-wire proportional chambers, with a cathode
889 strip readout. The CSCs have a spatial resolution in the range of $50 \mu\text{m}$, and a maximum drift time
890 of about 30 ns, which makes them superior for handling the high flux of particles in the forward
891 region [42].

892 **4.5 Magnet System**

893 The ATLAS magnet system consists of four sets of superconducting magnets: a barrel solenoid,
894 a barrel toroid, and two end-cap toroids. The solenoid magnet produces a 2T magnetic field re-
895 sponsible for bending the trajectories of charged particles as they pass through the inner detector.
896 The three toroid magnets provide a field of 0.5 - 1 T and curve the path of muons passing through
897 the muon spectrometer.

898 The inner solenoid magnet is composed of over 9 km of niobium-titanium superconductor
899 wires, which are imbedded into strengthen pure aluminum strips. The solenoid is just 4.5 cm
900 thick, which minimizes interactions between the magnet material and particles passing through the
901 detector. It is housed in the LAr cryostat, as described in section 4.3.1, which further reduces the
902 amount of non-detector material required to support the solenoid. The return yoke of the magnet
903 is provided by the iron absorber of the TileCal [43].

904 The central ATLAS toroid magnet, providing the magnetic field for the barrel region of the MS,
905 is the largest toroidal magnet ever constructed at 25 m in length. The toroid is composed of eight
906 individual coils, each housed in their own cryostat. The toroidal magnetic field is advantageous
907 as the direction of the field is almost perpendicular to the path of the charged particles. 56 km of
908 aluminum stabilized niobium-titanium-copper superconductor wire compose the magnet. In each
909 end-cap, eight smaller superconducting coils extend the toroidal magnetic field to particles leaving
910 the detector in the forward direction [43]. Figure 4.9 shows the layout of the toroid magnets.

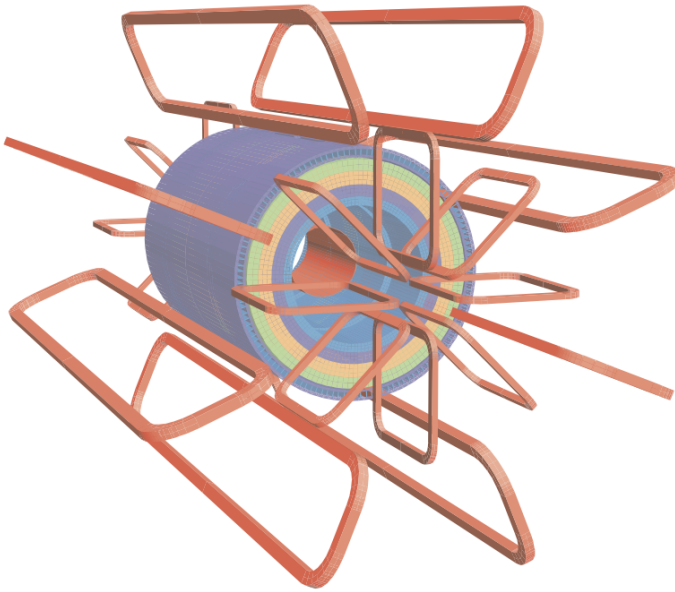


Figure 4.9: Layout of the barrel and endcap toroid magnets [34]

911 4.6 Forward Detectors

912 In addition to the inner detector, calorimeters, and muon spectrometer, three smaller detectors
 913 provide coverage in the very forward region. The innermost forward detector, at 17 m from the
 914 interaction point, is the **L**Uminosity measurement using **C**erenkov **I**ntegrating **D**etector (LUCID).
 915 LUCID's primary purpose is to measure the relative online-luminosity for the ATLAS detector,
 916 from inelastic $p - p$ scattering. The detector is composed of 20 aluminum Cerenkov tubes which
 917 surround the beam pipe and face towards the interaction point.

918 The second forward detector is the Zero-Degree Calorimeter (ZDC), located 140 m from the
 919 interaction point in both directions, at the point where the LHC beam-pipe divides into two separate
 920 pipes. The ZDC's primary purpose is to detect forward neutrons from heavy ion collisions.

921 The third forward detector is the Absolute Luminosity For ATLAS (ALFA) system, located 240
 922 m from the interaction point in both directions. ALFA determines luminosity by measuring elastic
 923 scattering at small angles, from which luminosity can be calculated via the optical theorem. The
 924 detector is built from scintillating fiber trackers. These are connected to the accelerator vacuum

via Roman pots, which allow the detector to come as close as 1mm to the beam without disrupting the machine vacuum. The LUCID and ALFA detectors are crucial to determining the real-time conditions of the beams and the total luminosity delivered to the ATLAS detector [34].

4.7 Trigger and Data Acquisition

The trigger and Data Acquisition systems (TDAQ) are responsible for selecting the most viable events to save for further downstream processing. Because of the high luminosities delivered to the ATLAS detector, not all events recorded can be saved; the 40 MHz bunch crossing rate must be reduced by 5 orders of magnitude to an event storage rate of ~ 1 kHz. The trigger system is composed of three distinct levels: Level 1 (L1), Level 2 (L2) and the event filter. Collectively the L2 trigger and the event filter form the High Level Trigger (HLT).

The L1 trigger is implemented in the hardware of the ATLAS calorimeter and muon systems. The primary modality of the L1 trigger is to identify muons, electrons, photons, jets, and τ -leptons with high transverse momentum. Particles with high transverse momentum are more likely to originate from direct, high energy collisions, which are most likely to produce interesting physics processes. The L1 trigger also identifies events with large missing transverse energy, which could be indicative of new physics. The L1 muon trigger (L1Muon) relies on RPC and TGC trigger chambers in the barrel and end-cap regions of the muon spectrometer. The L1 Calorimeter Trigger (L1Calo) uses reduced granularity information collected by all the calorimeter subsystems. Results from the L1Muon and L1Calo triggers are combined by the Central Trigger Processor (CTP), which implements a trigger ‘menu’, listing various combinations of trigger requirements. The maximum L1 acceptance rate is 75 kHz, and the L1 trigger decision must reach the front-end electronics within $2.5 \mu\text{s}$ of its associated bunch-crossing [34].

The L1 trigger defines a Region-of-Interest (RoI) for each passing event. The ROI is represented by the η - ϕ detector region where interesting features were identified by the L1 selection process. Information about the type of feature identified and the threshold which was exceeded to trigger the L1 response is also recorded. The ROI data is sent to the L2 trigger, which uses all of

951 the available information within the ROI at full granularity and precision. The L2 trigger reduces
952 the event rate from 75 kHz to 3.5 kHz, with an average processing time of 40 ms. The final stage of
953 the HLT is the event filter, which reduces the event rate to 200 Hz. The event filter uses an offline
954 analysis process to select fully rebuilt events which will be saved for further analysis.

955 All levels of the ATLAS trigger system depend on specialized electronics. Each detector front-
956 end system has a specialized Readout Driver (ROD) which collects information from several front-
957 end data streams at once. The ROD is composed of front-end analogue processing, an L1 buffer
958 which retains the information long enough for the L1 trigger decision, and dedicated links which
959 send the front-end L1 triggered data to Data Acquisition System (DAQ). Any digital signals are
960 formatted as raw data before being transferred to the DAQ. The first stage of the DAQ temporarily
961 stores the L1 data in local buffers. The ROI data is then requested by the L2 trigger, after which
962 selected events are transferred to an event building system, before events passing the event filter
963 are sent to the CERN computer center for permanent storage. The DAQ system not only allows
964 for the readout of detector data, but is also responsible for the monitoring and configuration of
965 the hardware and software components which make up the data readout system via the Detector
966 Control System (DCS).

967 The DCS allows centralized control of all detector subsystems simultaneously. It continually
968 monitors operational conditions, reports any abnormal behavior to the operator, and can perform
969 both automatic and manual interventions. The DCS reports on real time detector conditions such
970 as high or low voltage detector electronics, gas and cooling systems, magnetic field conditions,
971 humidity and temperature. This information is continually monitored by experts in the ATLAS
972 control room, so that action can be taken immediately to correct any issues that arise. The DCS also
973 handles communication between detector systems, and other systems such as the LHC accelerator,
974 the ATLAS magnets, and CERN technical services [34].

Chapter 5: Particle Reconstruction and Identification

With a design luminosity of $1.0 \times 10^{34} \text{ cm}^{-2}\text{s}^{-1}$, and a peak Run-2 instantaneous luminosity of $2.0 \times 10^{34} \text{ cm}^{-2}\text{s}^{-1}$, reconstructing and identifying the products of LHC pp collisions is one of the most complex tasks for each LHC experiment. The accurate reconstruction and identification of physics objects lays the ground work for all subsequent physics analyses, so it is also one of the most fundamentally important tasks performed by an experiment.

Reconstruction is the process of combining raw and uncalibrated hits across various subsystems into specific unique objects. Two particular subsystems, the Inner Detector (ID) tracker and the calorimeters play particularly important roles and will be discussed in detail. Analysis of the properties of the reconstructed objects identifies them as photon, electrons, muons, or jets. While photons, electrons, and muons are fundamental particles, jets represent a collimated shower of many hadronic particles, whose definition is more flexible. Jet reconstruction, clustering and track association are all of particular import to jet identification, and to the later content of this thesis. Finally, reconstruction also identifies missing transverse energy E_T^{miss} in events, which is a crucial variable for BSM physics searches. Figure 5.1 shows how the physics objects listed here interact with various systems in the ATLAS detector.

5.1 Inner Detector Tracks

As the inner most layer of the detector, the ID measures charged particles close to the interaction point. The various hits of these charged particles throughout the ID are used to reconstruct *tracks* which give the trajectories of charged particles [45]. Track reconstruction begins by clustering hits in the Pixel and SCT detectors, and combining clusters from different radial layers of these detectors. The multi-layer clusters form track *seeds*, which provide initial estimates of mea-

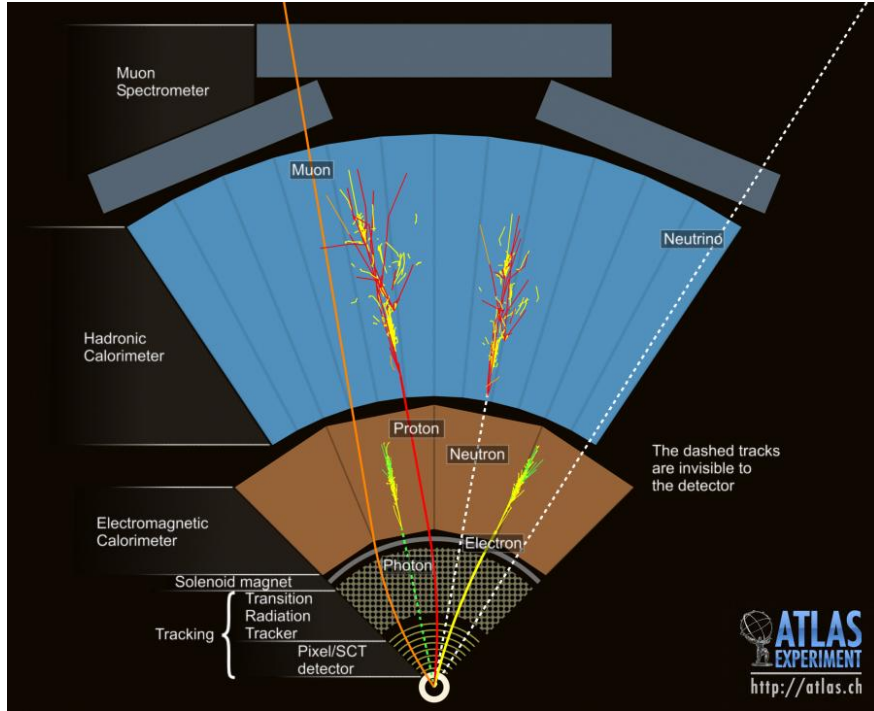


Figure 5.1: Graphic illustrating the various objects and high level features identified by ATLAS object reconstruction, and their interaction with different systems of the ATLAS detector [44]

998 surements belonging to an individual track. The requirement of three points allows for a rough
 999 estimate of the track p_T to be made by calculating the curvature of the track and accounting of the
 1000 magnetic field in the ID.

1001 Track seeds are subject to a variety of quality requirements, such as having a minimum esti-
 1002 mated p_T and passing interaction region compatibility criterion. If these requirements are satisfied,
 1003 the track seeds are passed to the track finding and fitting algorithms. The interplay of these three
 1004 track reconstruction steps is illustrated in Figure 5.2.

1005 **5.2 Photons and Electrons**

1006 Photons and electrons shower in the LAr calorimeter, and are identified by the energy deposits
 1007 they leave there. Energy deposits in a collection of nearby cells are termed *clusters*, which become
 1008 the starting point for electron and photon reconstruction [46]. The clustering algorithm begins
 1009 when the energy deposit in a certain cell exceeds the noise threshold with a significance of 4σ .

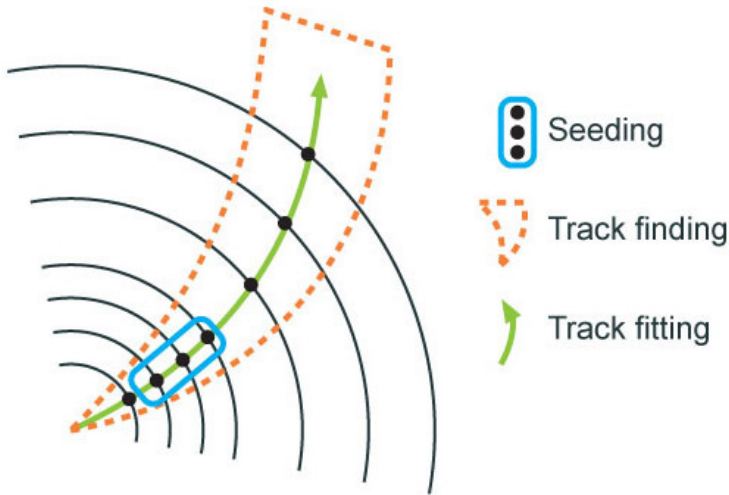


Figure 5.2: Track reconstruction seeding, finding and fitting illustration [45]

1010 The algorithm then collects neighboring cells which have an energy deposit exceeding the noise
 1011 threshold with a significance of 2σ , creating a topo-cluster. Next, these topo-clusters are matched
 1012 to ID tracks, created as described in Section 5.1. The location of the topo-cluster defines a region
 1013 of interest (ROI) in the ID, where additional modified track reconstruction algorithms are run in the
 1014 case that no associated tracks are found. Any ID tracks associated to the topo-cluster are retrofitted to
 1015 allow for additional energy loss due to bremsstrahlung. A converted photon track reconstruction
 1016 algorithm is run to check for tracks coming from secondary vertices consistent with converted
 1017 photons. The secondary vertices are constructed from two oppositely charged tracks consistent
 1018 with a massless particle, or from one track without any hits in the innermost layer of the ID.

1019 For electron identification, the EM cluster is required to match ID tracks that originate from
 1020 the primary vertex at the interaction point. For photon identification, the EM cluster can either be
 1021 matched to tracks coming from a secondary vertex (converted photon), or matched to no tracks
 1022 (unconverted photon). Figure 5.3 illustrates these three cases for EM object identification.

1023 *Superclusters* are built separately for photons and electrons, based on the combined topo-cluster
 1024 and ID track information. First, the EM topo-clusters are tested to see if they meet the minimum
 1025 requirements to become electron or photon seed clusters. For electrons, the cluster must have a
 1026 minimum E_T of 1 GeV, and must be matched to a track with at least 4 hits in the silicon tracking

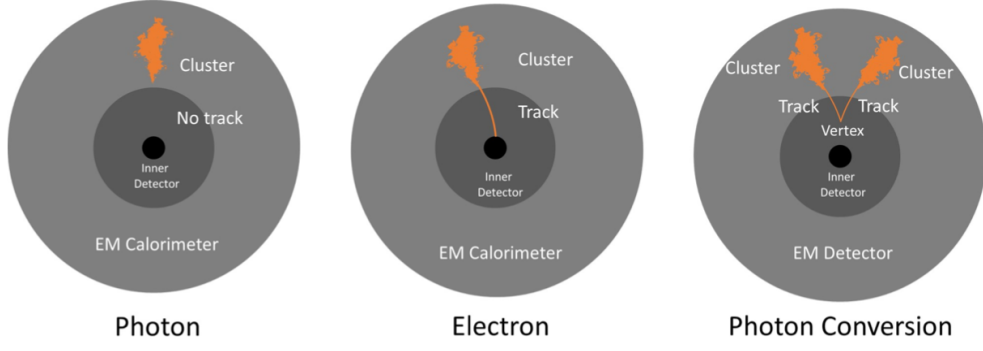


Figure 5.3: Three types of EM object candidates [47].

detectors. For photons, the cluster must have an E_T greater than 1.5 GeV. If the seed cluster requirements are met, the algorithm searches for satellite clusters, which can arise from bremsstrahlung radiation. If the satellite clusters pass the positional, energy and tracking requirements to be associated with the proto-cluster, they are combined into a supercluster.

Electron and photon objects are identified from the superclusters after energy calibration and position corrections are applied. Because photon and electron superclusters are built independently, some clusters can produce both a photon and an electron. In this case an ambiguity resolution procedure is applied to determine if the supercluster can be easily identified as only a photon (no tracks present) or only an electron (good tracks pointing to the primary vertex). In some cases, the identity of the cluster is still ambiguous, in which case both a photon and electron object are created for analysis and flagged as ambiguous. Energy, shower shape, and other analysis variables are calculated from the supercluster and saved with the electron or photon object.

5.3 Muons

Muons are identified through the tracks and energy deposits they leave in the ID, calorimeters, and Muon Spectrometer (MS). Muon identification begins in the Muon Drift Tube chambers by performing a straight line fit between the hits found in each layer, creating *segments*. Segments in the middle layers are then used as seeds for the track building algorithm, which searches for compatible combinations of segments based on their relative positions and angles [48]. A χ^2 fit is

1045 performed on each track candidate. Based on the χ^2 criteria, hits are removed or added such that
1046 the track contains as many hits as possible while satisfying the fit criteria.

1047 The MS track candidates are combined with track information from the ID and calorimeters
1048 according to various algorithms based on the information available from each subdetector. Four
1049 different types of muons arise from the various reconstruction algorithms:

- 1050 • Combined muon: a muon track identified through independent track reconstruction in the
1051 ID and MS, where the combined track is formed using a global refit that uses hit information
1052 from both detectors. Most muons are constructed through an outside-in procedure, in which
1053 a muon track candidate is identified in the MS and then an associated track is found in the ID.
1054 A complementary inside-out procedure is also implemented and identifies additional muons.
- 1055 • Segment-tagged muon: an ID track is identified as a muon if when extrapolated out to the
1056 MS (following the inside-out global fit procedure) it is matched to at least one local MS
1057 segment.
- 1058 • Calorimeter-tagged muon: an ID track is identified as a muon if it is matched to a calorimeter
1059 energy deposit that is compatible with a minimum-ionizing particle. This muon identifica-
1060 tion has the lowest purity, but it used in regions where the MS has only partial coverage due
1061 to cabling and service access routes.
- 1062 • Extrapolated muons: the muon is reconstruction only from the MS track and a requirement
1063 on compatibility with the primary interaction point. The muon track is required to cross at
1064 least two layers of the MS, and three layers in the forward region. These muons are mainly
1065 used to extend muon acceptance into the region $2.5 < |\eta| < 2.7$ where ID track information
1066 is not available.

1067 Figure 5.4 illustrates the four types of muon reconstruction. Overlap between reconstructed
1068 muons using ID tracks is resolved by giving preference to combined muons, then segment tagged
1069 muons, and finally calorimeter tagged muons. Overlap with extrapolated muons is resolved by
1070 giving preference to the muon with a better fit quality and higher number of tracks.

1071 All muon track candidates are required to pass a series of quality selections to be identified in
 1072 the final muon collection. The primary qualities considered are the χ^2 goodness of fit for the global
 1073 track, the difference in p_T measurement between the ID and MS tracks, and the ratio between the
 1074 charge and momentum of the tracks. The quality requirements help reject hadrons, primarily from
 1075 kaon and pion decays. Muons candidates consistent with cosmic rays are also rejected.

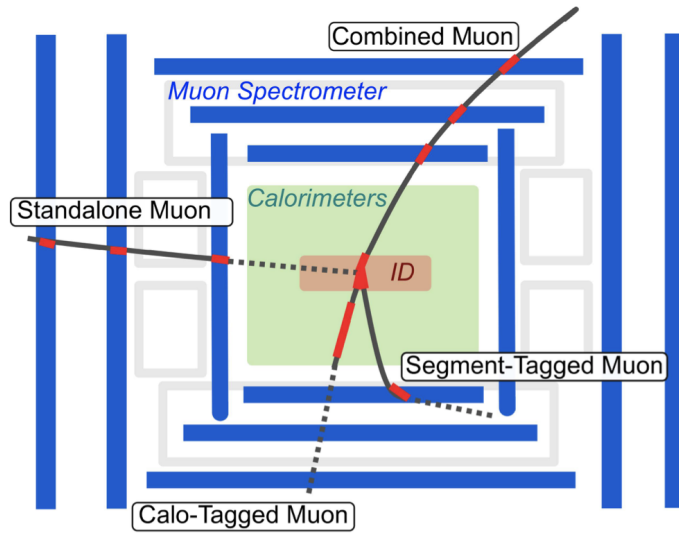


Figure 5.4: Four types of muon track candidates [49].

1076 5.4 Jets

1077 The protons accelerated in the LHC are composed of quarks and gluons, and thus their colli-
 1078 sions often result in the release of energetic quarks and gluons, collectively termed *partons*. The
 1079 energetic partons can radiate additional gluons, and these gluons can pair produce quarks in a pro-
 1080 cess called *fragmentation*. Fragmentation continues until the energy drops sufficiently that color
 1081 conservation plays a dominant role. At that point, additional quarks and gluons are produced from
 1082 vacuum to create neutral color states for the fragmented collection of partons. This process is
 1083 known as *hadronization* [50]. The hadronized partons compose a collimated stream of particles,
 1084 known as a *jet*, which is then observed in the detector. The full process that produces jets is known
 1085 as a *parton shower*, and is illustrated in Figure 5.5.

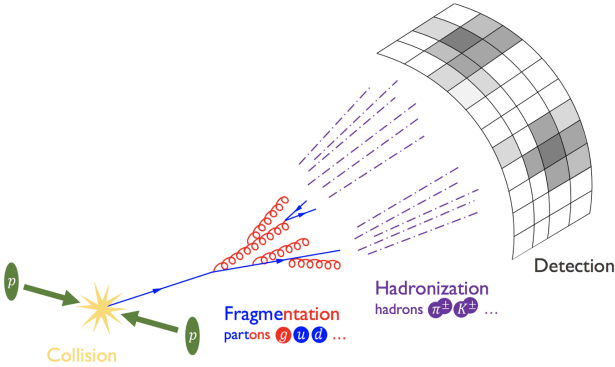


Figure 5.5: The fragmentation and hadronization processes undergone by a quark produced in a proton-proton collision [51].

1086 Jets are identified by the energy deposits they leave in the calorimeter, which are then matched
 1087 to the tracks they leave in the ID. Jet reconstruction generally begins in the calorimeters, with the
 1088 identification of *topo-clusters*. Then jet reconstruction algorithms combine calorimeter informa-
 1089 tion with tracking information. The anti- k_t algorithm [52] as provided by the FastJet library [53] is
 1090 generally used by the ATLAS experiment, with varying reconstruction radius settings. There are a
 1091 variety of jet collections depending on the exact usage of calorimeter and tracking information in
 1092 the reconstruction. Some common collections include particle flow jets (PFlow), track calo-cluster
 1093 jets (TCC), EM topo-cluster jets (EMTopo), and unified flow object jets (UFO). Only particle flow
 1094 jets will be discussed in greater detail due to their importance in this analysis. The following sec-
 1095 tions discuss jet identification in the calorimeters, particle flow jet construction using the anti- k_t
 1096 algorithm, jet clustering and jet substructure characteristics.

1097 5.4.1 Calorimeter Clusters

1098 Jets are first identified by the energy deposits they leave in the calorimeters. The reconstruc-
 1099 tion of jets in ATLAS begins with the construction of *topo-clusters*, which are topologically-grouped
 1100 noise-suppressed clusters of calorimeter cells [54]. The topo-cluster seed is a cell with an energy
 1101 that is at least 4× the average background noise level for the cell. Any cells adjacent to the seed
 1102 cell in three dimensions are added to the cluster if they have an energy deposit that is at least 2x

1103 the average expected noise. This process is repeated, growing the cluster, until no adjacent cells
1104 exceeding the energy deposit threshold remain. As a final step, all adjacent cells are added to the
1105 topo-cluster, irrespective of their energy.

1106 The construction process for topo-clusters allows for the possibility that several independent
1107 signatures are grouped into one topo-cluster. To correct for this, the topo-cluster is scanned for
1108 local maximum, defined by any cell with energy > 500 MeV, and no neighboring cells with greater
1109 energy. If more than one local maximum is identified, the topo-cluster is split among the corre-
1110 sponding energy peaks [55]. In the event that one cell neighbors two or more local maxima, the
1111 cell is assigned to the two highest-energy clusters that is neighbors. This means each cell is shared
1112 at most once, between at most two post-splitting topo-clusters.

1113 Two measurements for the total energy of the topo-cluster are considered. The raw, or electro-
1114 magnetic (EM), scale simply considers the sum of energy from all cells in the topo-cluster. The
1115 local cell weighting (LCW) scale first classifies clusters as electromagnetic or hadronic, and then
1116 applies appropriate corrections for hadronic interactions in the jet energy calculation [54]. The
1117 corrections are derived from Monte Carlo simulations, and account for the weaker response of
1118 ATLAS calorimeters to hadronic interactions (ATLAS calorimeters are *non-compensating*), and
1119 hadronic energy losses due to interactions with dead material [55].

1120 5.4.2 Particle Flow Algorithm

1121 The calorimeters provide excellent jet energy resolution for high energy jets. However, the
1122 granularity of the hadronic calorimeter is restricted to 0.1×0.1 in $\eta \times \phi$. Combining the infor-
1123 mation from the calorimeter with tracking information provides superior angular resolution and
1124 energy resolution. The particle flow (PFlow) algorithm is one of a handful of algorithms which
1125 can perform this task.

1126 An overview of the process is given in Figure 5.6. Tracks from the ID which are selected for the
1127 PFlow algorithm are required to have at least 9 hits in the silicon detector, and missing pixel hits in
1128 places where a hit would be expected. Additionally, the tracks have $p_T > 0.5$ GeV, and $|\eta| < 2.5$.

1129 The algorithm then attempts to match these tracks to EM scale calorimeter topo-clusters. This
1130 matching is performed using the distance metric

$$\Delta R' = \sqrt{\left(\frac{\Delta\phi}{\sigma_\phi}\right)^2 + \left(\frac{\Delta\eta}{\sigma_\eta}\right)^2} \quad (5.1)$$

1131 where σ_η and σ_ϕ represent the angular widths of the topo-clusters, and $\Delta\eta$ and $\Delta\phi$ represent the
1132 distance between the track, extrapolated to the second layer of the EM calorimeter, and barycenter
1133 of the topo-cluster [56]. The topo-cluster closest to the track as measured by $\Delta R'$ is considered
1134 matched to the track. If no topo-cluster is found within the cone size of $\Delta R' = 1.64$, it is assumed
1135 that particle which left the track did not form a topo-cluster in the calorimeter.

1136 The PFlow algorithm predicts the expected single topo-cluster energy for a given track, based
1137 on the track momentum and topo-cluster position. This value is then compared to the observed
1138 energy of the topo-cluster, and the probability that the particle energy was deposited in more than
1139 one topo-cluster is evaluated. If necessary, the algorithm adds more topo-clusters to the track/topo-
1140 cluster system, in order to account of the full shower energy of the track particle.

1141 To reduce the impact of double counting the energy of a given particle by including both its
1142 tracker and calorimeter energy measurements, the calorimeter energy measurements associated to a
1143 given track are subtracted from the total calorimeter measurement. If the expected energy deposited
1144 by the particle exceeds the topo-cluster energy, the full topo-cluster is removed. If the expected
1145 energy is less than the EM scale energy of all the considered topo-clusters, topo-cluster cells are
1146 removed one by one, until the full expected energy deposit of the particle has been removed from
1147 the calorimeter information. The resulting set of tracks and topo-clusters represent the event with
1148 no double-counting of energy between subdetectors [56]. This information is passed to the jet-
1149 finding algorithm.

1150 5.4.3 Jet Clustering

1151 When a parton decays in the detector, its energy deposits often result in multiple calorimeter
1152 clusters. For physics purposes, it is useful to combine clusters that likely resulted from an individ-

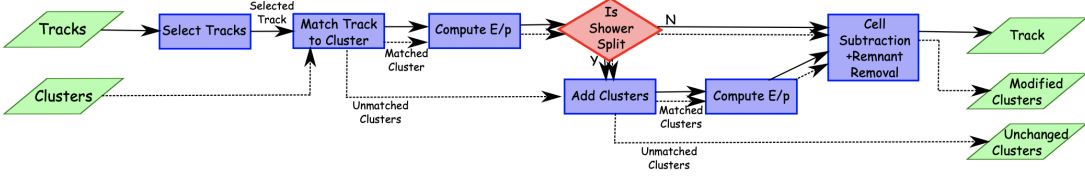


Figure 5.6: A flow chart illustrating the particle flow algorithm progression [56].

1153 ual parton decay, in order to reconstruct the parton. The process of grouping topo-clusters which
 1154 were produced by the same parton decay is *jet clustering*.

1155 The anti- k_t algorithm is the most commonly used algorithm for jet clustering in ATLAS. The
 1156 anti- k_t algorithm is based on sequential recombination algorithms [57]. A sequential recombina-
 1157 tion considers the distance d_{ij} between objects i and j (particles or pseudojets), and the distance
 1158 d_{iB} between an object i and the beam line B . If d_{ij} between two objects is the smallest distance
 1159 among those considered, i and j are combined into a pseudojet. The process continues until the
 1160 smallest distance is d_{iB} at which point the object i is determined to be a jet and removed from the
 1161 objects in consideration. The procedure is repeated with the remaining objects until there are none
 1162 remaining [52].

1163 The anti- k_t algorithm adopts this procedure, but modifies the distance measurements d_{ij} and
 1164 d_{iB} to consider the transverse momentum k_t :

$$d_{ij} = \min(k_{ti}^{2p}, k_{tj}^{2p}) \frac{\Delta_{ij}^2}{R^2}, \quad (5.2a)$$

$$d_{iB} = k_{ti}^{2p}. \quad (5.2b)$$

1165 The addition of the term p allows adjustments to algorithm which govern the relative power of
 1166 the momentum versus the geometrical scale $\Delta_{i,j}$, which is defined as $\Delta_{i,j} = (y_i - y_j)^2 + (\phi_i - \phi_j)^2$
 1167 where y_i and ϕ_i are respectively the rapidity and azimuth of particle i [52]. The radius parameter
 1168 R is chosen and determines the geometric cone size [57].

1169 In the case $p = 1$ the inclusive k_t algorithm [57] is recovered, which is a standard sequential

combination jet clustering algorithm. In the case $p = 0$, the Cambridge/Aachen sequential combination algorithm [58] is recovered. The case $p = -1$ gives rise to the anti- k_t algorithm. The impact of this choice means that the distance d_{ij} between many soft particles is larger than between soft and hard particles. Therefore, soft particles tend to cluster with hard ones before they cluster with other soft particles. They key feature of this behavior is that soft particles do not modify the shape of the jets. This leads to the creation of circular conical jets, a desirable feature which sequential combination algorithms and cone algorithms struggle to achieve. Figure 5.7 compares anti- k_t jet formation with the inclusive k_t and Cambridge/Aachen algorithms mentioned here, as well as the SIScone algorithm [59], which checks for sets of stable cones compatible with the observed radiation.

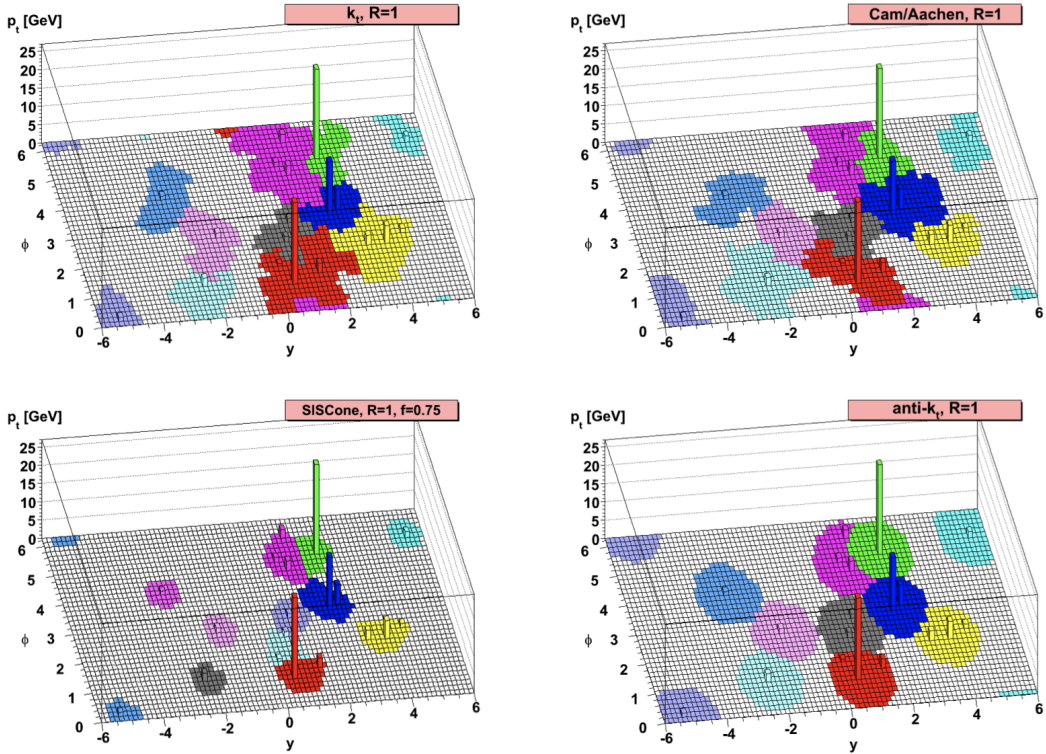


Figure 5.7: A comparison of jet clustering with four different jet algorithms. The anti- k_t algorithm is observed to create the most conical jets, where the shape of the jet is immune to the presence of soft radiation [52].

Any useful jet clustering algorithm must satisfy the requirements of infrared safety and collinear

1181 (IRC) safety. Infrared safety implies that the resulting set of jets is unaltered by the presence of
1182 additional soft particles in the list of seed clusters. As explained above, the anti- k_t algorithm is
1183 natural infrared safe. Collinear safety requires that the final set of jets is not impacted by collinear
1184 splitting of one of the jets. If the hardest particle p_1 is split into a collinear pair (p_{1a}, p_{1b}) (as
1185 is common in the fragmentation process for a hard parton), the jet clustering algorithm must
1186 still recognize (p_{1a}, p_{1b}) as the hardest jet in the collision. If another softer particle p_2 with
1187 $p_{t,1a}, p_{t,1b} < p_{t,2} < p_{t,1}$ is instead considered the hardest particle in the event, a different final
1188 set of jets would be returned. Collinear safety is a requirement of perturbative QCD, to ensure
1189 non-divergent higher-order calculations [60]. The anti- k_t algorithm's tendency to cluster hard par-
1190 ticles first ensures its collinear safety. By satisfying the IRC safety requirement, anti- k_t jets can be
1191 calculated using perturbative QCD, which improves comparisons with theory.

1192 5.4.4 Ghost Track Association

1193 Once a collection of jets has been created, the jet objects can be studied at both the event-level
1194 and the jet-level. In the event-level picture, the momentum, energy, and geometric orientation
1195 of the jets within an event are considered. This yields important information about decay of any
1196 resonant heavy objects, the total energy in the event, and the distribution of energy amongst the jets.
1197 At the jet-level picture, the particles composing the jet are considered. The momentum, energy,
1198 and geometric orientation of the particle tracks provides a low-level picture of the jet, which can
1199 help determine if the properties of the jet are consistent with standard QCD, or if new physics
1200 processes might be represented within the patterns found in the constituent particles. Jet-level
1201 analysis is also widely used in flavor tagging.

1202 For anti- k_t jets with a radius parameter $R = 0.4$, one way of studying the jet-level picture
1203 is through considering the ghost-associated tracks. Track association is process of determining
1204 which tracks should be considered associated with a given jet. In the ghost association algorithm,
1205 the anti- k_t clustering algorithm is used for the collection of tracks and calorimeter clusters [61].
1206 However, the tracks are considered to have infinitesimal momentum (*ghosts*), so their addition to

1207 a jet object does not alter the four-momentum of the jet. This ensures the final jet collection is not
1208 altered by the presence of the ghost tracks in the reclustering, but information about the associated
1209 tracks for each reconstructed jet becomes available [62].

1210 Ghost tracks are of particular importance to this analysis, as a means of providing a low-level
1211 picture of the shape of $R = 0.4$ jets, and discriminating Standard Model QCD-like jets from dark
1212 QCD-like jets.

1213 5.5 Missing Transverse Energy

1214 A simple principle leveraged in ATLAS physics analyses is checking for conservation of mo-
1215 mentum among the products of any pp collisions. The initial state transverse momentum of any
1216 pp collision is always zero, so the transverse momentum of all final state particles should likewise
1217 be zero. The missing transverse energy, E_T^{miss} , is determined by the magnitude of the negative
1218 momentum vector sum of all final state objects resulting from the pp collision.

1219 Specifically, the objects considered in the E_T^{miss} calculation are photons, electrons, muons, jets,
1220 and soft terms. The first four items comprise the hard components of the E_T^{miss} calculation, and
1221 have been discussed previously in this chapter. The final item represents a collection of *soft terms*,
1222 comprising any detector signals not associated to hard detector objects. These can be based on
1223 unassociated tracks, or unassociated soft calorimeter clusters. Both are generally not used in the
1224 same calculation to avoid double counting of soft terms. In this analysis the calorimeter cluster
1225 soft terms are considered in the E_T^{miss} calculation.

1226 E_T^{miss} can arise due to non-interacting Standard Model objects such as neutrinos, fake sources
1227 such as mis-reconstructed objects and dead detector regions, or in some theories, non-interacting
1228 BSM objects such as a dark matter candidate particles. To understand the amount of E_T^{miss} at-
1229 tributable to detector noise and mis-reconstruction, E_T^{miss} is studied in $Z \rightarrow \mu\mu$ where little real
1230 E_T^{miss} is expected [63]. As Figure 5.8 illustrates, the resolution of E_T^{miss} generally decreases as
1231 E_T^{miss} increases, due to detector resolution effects. As E_T^{miss} is an important quantity for most dark
1232 QCD analyses, limitations in the accuracy of the E_T^{miss} calculation must be considered.

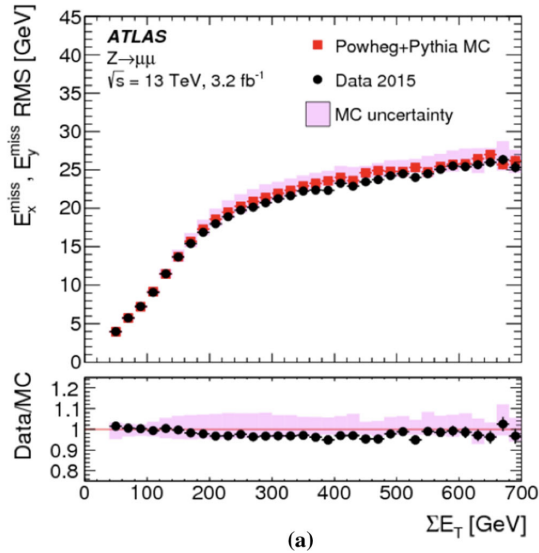


Figure 5.8: A comparison of MC simulation and data for $Z \rightarrow \mu\mu$ events where real $E_T^{\text{miss}} = 0$ [63]. The resolution of the missing energy in the transverse ($x - y$) plane is observed to increase with increasing total $\sum E_T$.

1233

Part III

1234

Search

1235

1236

Chapter 6: Monte Carlo and Data

1237 The search for semi-visible jets via s-channel production presented in the following chapters is
1238 performed with 139 fb^{-1} of proton-proton collision data collected by the ATLAS detector during
1239 Run 2 (2015 - 2018). The full Run-2 dataset is used for the final interpretation. Monte Carlo
1240 (MC) simulations of background processes and the semi-visible jet signal process are used in the
1241 development of the analysis strategy, and in the final interpretation to set limits on the observed
1242 cross-section of the signal model. This chapter will provide details about the full Run-2 dataset,
1243 and the background MC simulations, and the signal MC simulations used in this search.

1244 **6.1 Data**

1245 The 139 fb^{-1} of proton-proton collision data is selected according to the *good runs list* (GRL),
1246 which identify runs with good detector conditions that are suitable for physics evaluation. Events
1247 are further selected to pass a single-jet trigger selection, where events are required to have a jet at
1248 trigger-level with a p_T that exceeds a certain value. The lowest p_T unprescaled single jet trigger
1249 threshold for each period is as follows:

- 1250 • 2015: $p_T \geq 360 \text{ GeV}$
- 1251 • 2016 & 2017: $p_T \geq 380 \text{ GeV}$
- 1252 • 2017: $p_T \geq 380 \text{ GeV}$
- 1253 • 2017 & 2018: $p_T \geq 420 \text{ GeV}$

1254 A post-trigger selection of jet $p_T > 450 \text{ GeV}$ ensures all these triggers are fully within their
1255 efficiency plateaus. The jet collection used is anti- k_t EM particle flow jets with a radius parameter
1256 of $R = 0.4$, also referred to as small-R jets.

1257 Due to the variance in visible and invisible momenta due to the R_{inv} parameter of the signal
1258 model, many signals also have significant E_T^{miss} . The use of a E_T^{miss} trigger to select events was
1259 considered, and the single jet approach described here was found to preserve more signal events
1260 across the grid, particularly in the high resonance mass and low R_{inv} region of phase space. These
1261 studies are documented in Appendix A.

1262 The data are subject to a blinding strategy throughout the analysis design so as to mitigate
1263 analyzer-induced bias. Blinded and unblinded region definitions are described further in Sec-
1264 tion 8.1.

1265 6.2 Simulation

1266 Simulated events are generated with a variety of Monte Carlo (MC) generator processes that
1267 run in stages. The pp hard scatter physics process is simulated, and the final state particles are
1268 subsequently showered and decayed. This full description of the event is then propagated through
1269 a detailed detector simulation based on GEANT4 [64]. The MC simulation is weighted to match
1270 the distribution of the average number of interactions per bunch crossing μ observed in collision
1271 data.

1272 All simulated samples included in this analysis were produced with three different campaigns:
1273 `mc20a` corresponds to 2015-2016 data-taking conditions, `mc20d` to 2017, and `mc20e` to 2018.
1274 These three campaigns are weighted to the integrated luminosities of their respective data-taking
1275 periods and combined to produce simulation for the entire Run 2 dataset. Simulated events are
1276 reconstructed with the same algorithms run on collision data.

1277 6.2.1 Simulated Backgrounds

1278 Though the final background estimation is data-driven, background MC is studied for analysis
1279 optimization and machine learning tool development.

1280 Dijet QCD is the dominant background process. QCD is simulated with PYTHIA8 [65], and
1281 generated in approximate slices of p_T , to ensure high statistics across the momentum spectrum.

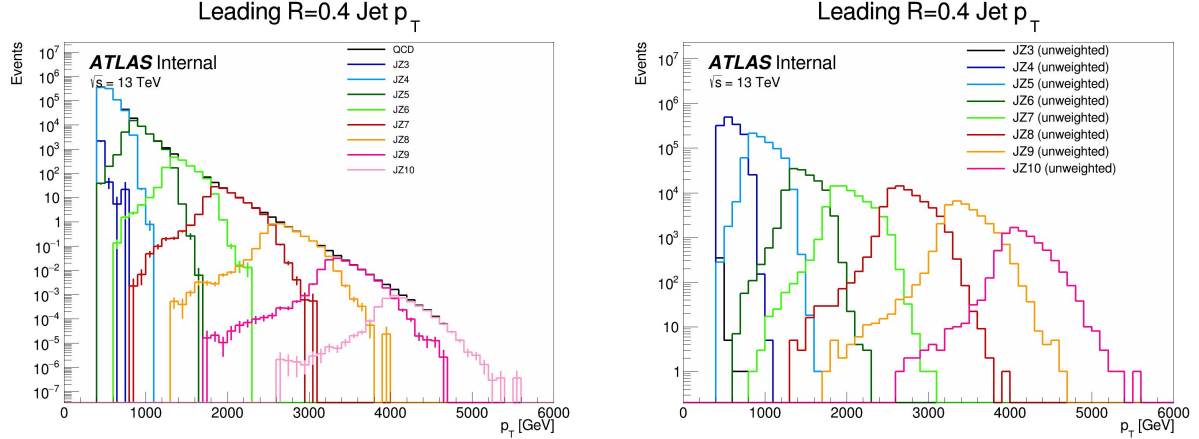


Figure 6.1: The transverse momentum slices of the QCD MC simulation, overlayed to show how they come together to create a smooth distribution (left) once weighted properly. The original unweighted distribution is shown on the right, illustrating the enhanced statistics for the high p_T range.

1282 The slices are then reweighted using MC generated event weights to create a physical distribution.
 1283 Figure 6.1 illustrates the 8 momentum slices used in this analysis.

1284 Due to presence of E_T^{miss} in the SVJ signals, additional MC background processes are required
 1285 to create a full picture of the relevant background. The $Z \rightarrow vv$ process contributes to the back-
 1286 ground due to its high missing energy. Leptonic W/Z decays and W/Z+jets are also included as
 1287 they can contribute both additional missing energy and significant hadronic activity. Single top
 1288 and $t\bar{t}$ processes are also considered for their contribution to hadronic activity,. The background
 1289 composition in the selected region (discussed in Section 8.1) is 76% QCD, 12% W/Z+jets, 8%
 1290 top and $t\bar{t}$ processes, and 4% $Z \rightarrow vv$. Figure 6.2 illustrates the background composition for the
 1291 analysis.

1292 6.2.2 Signal Simulation

1293 The Hidden Valley signal model implementation is based on Ref [22]. The s-channel semi-
 1294 visible jet model is governed by a number of parameters. The mass of the mediator $m_{Z'}$ can be set,
 1295 together with the couplings of the Z' to the visible and dark quarks g_q and g_{q_D} . The dark sector
 1296 shower is governed by the number of dark colors N_{c_D} , the number of dark flavors N_{f_D} , and the

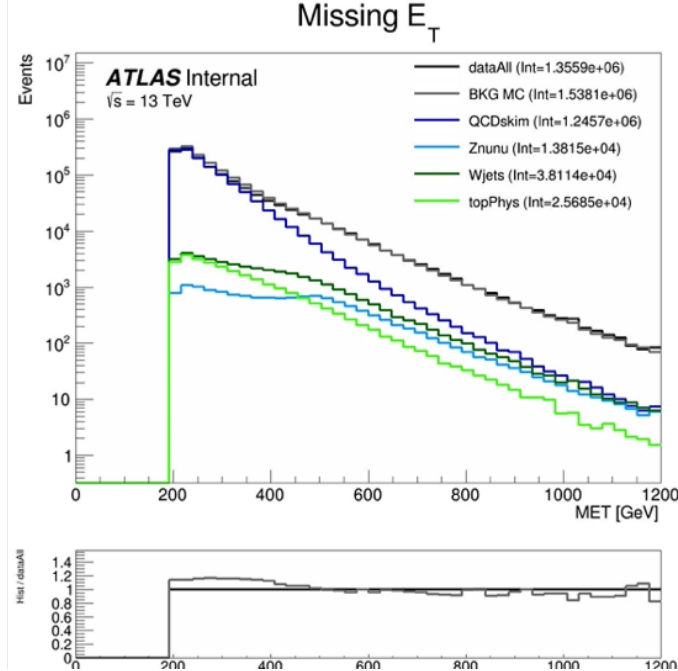


Figure 6.2: Background processes relevant to the SVJ signal. The agreement between the black line (data) and grey line (all MC processes combined) illustrates that this collection of background processes is sufficient to model the expected E_T^{miss} in the selected data events.

1297 dark sector confinement scale Λ_D . There is also the characteristic scale of the dark hadrons m_D ,
 1298 which determines the mass of the dark hadrons, which can be pseudoscalars m_{π_D} or vectors m_{ρ_D} .
 1299 Finally, the average fraction of invisible particles in the final state jet is dictated by R_{inv} .

1300 The chosen parameters for this model were carefully selected in collaboration with theorists to
 1301 be compatible with the new benchmarks established in the 2021 Snowmass process [21]. These pa-
 1302 rameters reflect extensive communication with the Snowmass, CMS, and theory teams. The signal
 1303 generation allows for up to two initial state radiation jets, and uses an MLM merging scheme [65]
 1304 to match jets to the original partons.

1305 The choices of fixed parameters for the Pythia8 HV model are summarized in Table 6.1. A
 1306 detailed discussion of these parameters and their implications on the dark shower topology can be
 1307 found in Ref. [21]. The mass choices for the dark quark and the dark hadrons are also summarized
 1308 in Table 6.2.

1309 Note that the number of dark flavors differs from the Snowmass recommendation of $N_{f_D} = 4$.
 1310 This change is minimal in impact because R_{inv} is set explicitly (rather than allowing it to arise

Parameter	Value
HiddenValley:Ngauge	3
HiddenValley:alphaOrder	1
HiddenValley:Lambda	10.0
HiddenValley:nFlav	2
HiddenValley:spinFv	0
HiddenValley:FSR	on
HiddenValley:fragment	on
HiddenValley:pTminFSR	1.1
HiddenValley:probVector	0.58

Table 6.1: Fixed parameters in the Pythia8 HV model

Parameter	Value [GeV]
m_{π_D}	17
m_{ρ_D}	31.77
m_{q_D}	10

Table 6.2: Values for m_{dark}

naturally from the HV theory), and allows us to remain more comparable with the CMS semi-visible jets analysis and the ATLAS t-channel analysis.

The mediator mass $m_{Z'}$ and the fraction of invisible particles in the final state R_{inv} vary, and are used to define the search grid. $m_{Z'}$ varies between 2.0 TeV and 5.0 TeV, while R_{inv} varies from 0.2 to 0.8. R_{inv} values of 0.2, 0.4, 0.6, and 0.8 are generated for each $m_{Z'}$ mass point. Table 6.3 illustrates the signal grid and the associated cross-section for each signal.

Samples are generated using MADGRAPH5 [66] version 2.9.9 interfaced to PYTHIA8.244P3 [65] for shower and hadronization with NNPDF23LO PDF [67] and the ATLAS A14 [68] to tune the underlying event data.

$m_{Z'}$ (GeV)	Cross section (fb)
2000	2.52e+2
2500	7.42e+1
3000	2.45e+1
3500	8.83e+0
4000	3.49e+0
5000	7.57e-1

Table 6.3: Mass points and cross sections of the SVJ search signal grid

1320

1321

Chapter 7: Machine Learning Tools

1322 **7.1 Introduction**

1323 The search for semi-visible jets presents an opportunity to use novel machine learning (ML)
1324 tools to uncover patterns in the behavior of dark QCD. The subtlety of the shower differences be-
1325 tween dark and SM QCD motivates a complex model that can accept high-dimensional low-level
1326 inputs to best understand key differences between signal and background correlations. Addition-
1327 ally, the large number of theory parameters which can be chosen arbitrarily and affect the shape of
1328 the dark QCD shower motivate exploring a data-driven machine learning approach, which could
1329 be sensitive to a wider variety of dark QCD behavior.

1330 To this end, two machine learning approaches are developed for this search, which are used
1331 in tandem. The first is a supervised ML method where the ML algorithm is built to maximize
1332 exclusion sensitivity to the specific generated SVJ signal models used in this analysis. Here, su-
1333 pervised refers to the use of full and correct labels for all events considered during model training,
1334 which necessitates training over simulated data. The second is a semi-supervised method, where
1335 training of the model is data-driven and labels are only partially provided during training. The
1336 semi-supervised ML algorithm broadens the discovery sensitivity of the search, and reduces the
1337 dependence on the exact theory parameters chosen for signal model simulation.

1338 The two different ML algorithms used in this approach will be explained in the following
1339 sections, along with their application in the SVJ analysis strategy.

1340 7.1.1 Particle Flow Network (Supervised)

1341 **Architecture Fundamentals**

1342 A Particle Flow Network (PFN) [69] architecture is selected for two reasons: *permutation in-*
1343 *variant input modeling* to best describe the events consisting of an unordered set of particles, and a
1344 *low-level input modeling* using tracks to take advantage of the available high-dimensional informa-
1345 tion to best exploit available correlations within the event. Permutation invariant input modeling
1346 is an architecture priority as ordered input modeling has been observed to bias the performance of
1347 low-level modeling tools as in [70]. Low-level input modeling is an architecture priority to capture
1348 the intricacies of dark QCD showers which may not express themselves in higher level variables,
1349 as explored in [22]. A comparison to a high-level *boosted decision tree* (BDT) is available in
1350 Appendix B.3.

1351 The PFN is used to model input events as an unordered set of tracks. Given the inherently
1352 unordered and variable-length nature of particles in an event, this choice of modeling as a *set*
1353 can enable the model to better learn the salient features of the dataset that enable a signal-to-
1354 background classification. Constructing the PFN involves the creation of new basis variables \oplus
1355 for each particle in the event. Permutation invariance is enforced by summing over the \oplus basis for
1356 every particle in the event to create a new permutation invariant latent space basis O . Finally the
1357 classifier F is a function of the sum over this new basis. The creation of the latent space basis O
1358 from M particles \vec{p} with d features each can be expressed as:

$$O(\{\vec{p}_1, \dots, \vec{p}_M\}) = \sum_{i=1}^M \Phi_i(\vec{p}_i) \quad (7.1)$$

1359 where $\Phi : \mathbb{R}^d \rightarrow \mathbb{R}^l$ is a per particle mapping, with l being the dimension of the new basis O .
1360 Figure 7.1 gives a graphical representation of the use of summation in the PFN over per-particle
1361 information to create a permutation-invariant event representation.

1362 Figure 7.2 provides an annotated diagram of the PFN architecture as used in this analysis.

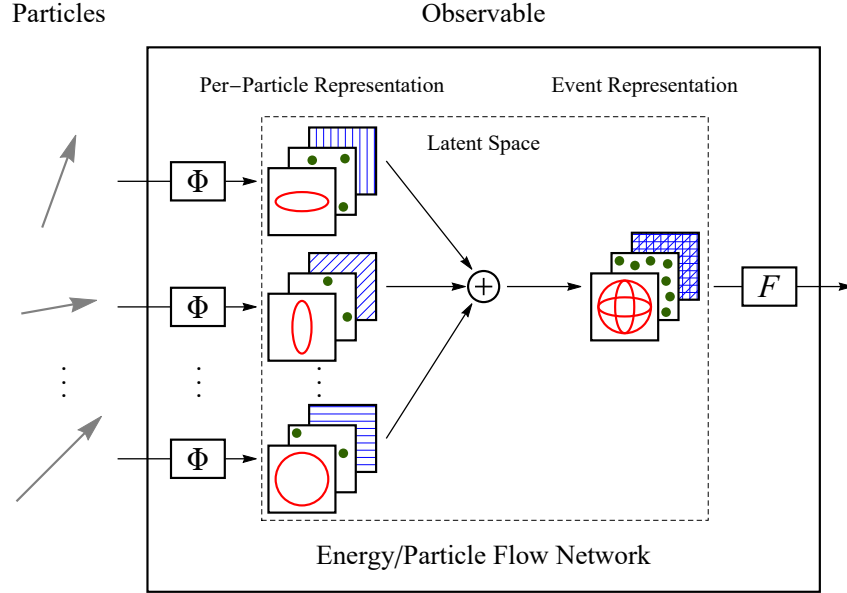


Figure 7.1: The Energy/Particle Flow Network concept, from Ref. [69].

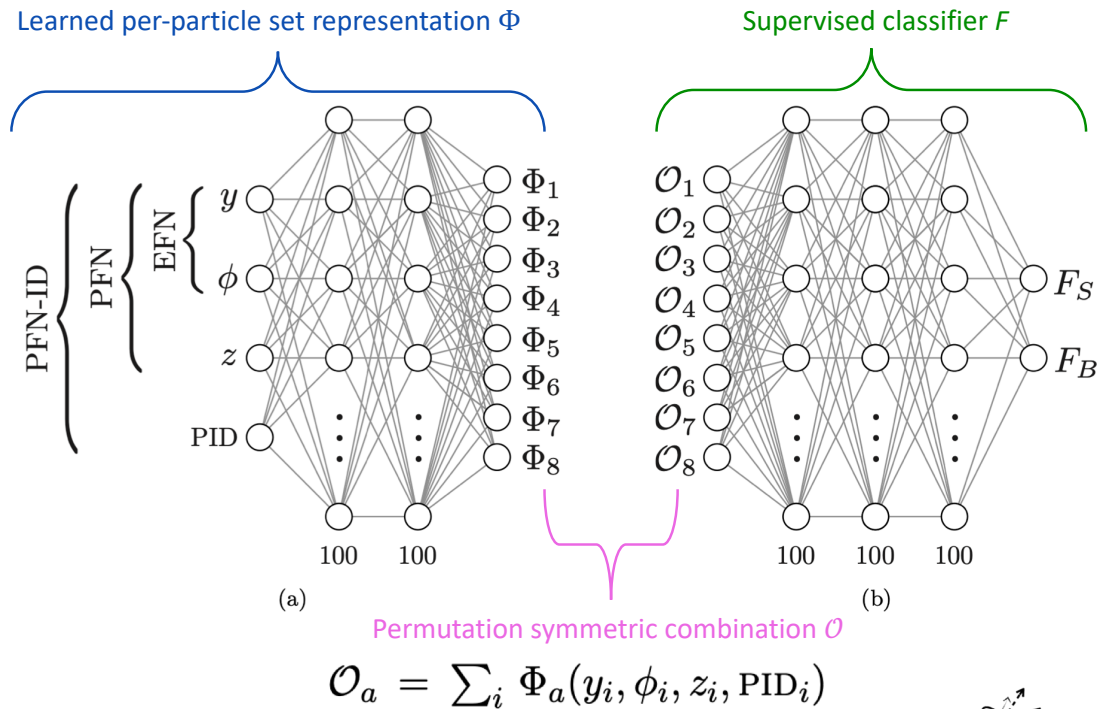


Figure 7.2: An annotated diagram of the PFN architecture. y and ϕ represent geometric information for the input particles, z represents energy information, and PID encompasses any other particle ID information in the input.

1363 **Input Modeling, Scaling, and Rotation**

1364 In this implementation, the particle input information comes from all tracks associated to the
1365 leading and subleading jets. The track association method is Ghost association, as discussed in
1366 Section 5.4.4. A single jet tagger strategy was also considered, but utilizing tracks from both
1367 leading jets creates a complete low-level picture of the event, which both focuses on the objects
1368 most likely to be associated to the decay of the dark quark (as will be justified in Chapter 8)
1369 and the relationship between those objects. If we consider the dijet topology of semi-visible jets
1370 as illustrated in Figure 7.3, the advantage of modeling both leading jets simultaneously becomes
1371 clear. In the semi-visible jet model presented in [22], E_T^{miss} in the event is expected to arise due to
1372 an imbalance in the number of visible tracks of the two jets associated to the dark quark decay.

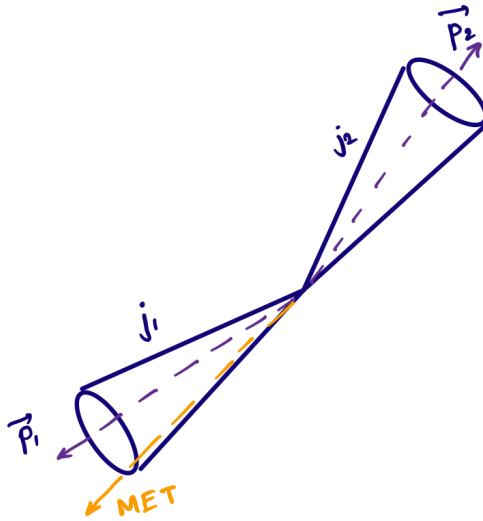


Figure 7.3: A illustration of the expected dijet behavior of semi-visible jets, where one jet is closely aligned with E_T^{miss} .

1373 Each track is described using six variables: the four-vector of the track (p_T , η , ϕ , E), and the
1374 track displacement parameters d_0 and z_0 , where d_0 measures displacement in the radial direction
1375 from the beamline and z_0 measures displacement along the beamline from the primary interac-
1376 tion point. Figure 7.4 illustrates these coordinates. Up to 80 tracks per jet are allowed, which is
1377 a threshold chosen to generally include all the tracks in the jet, which leads to maximal perfor-

1378 mance. Figure 7.5 shows the track multiplicity in the leading and subleading jet for the signal and
 1379 background samples used in training.

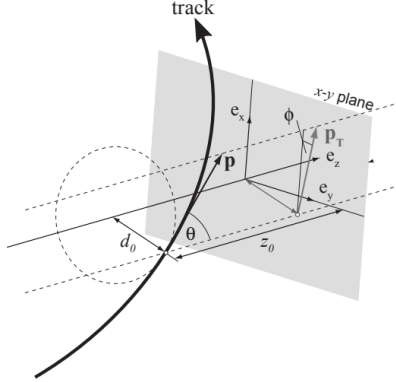


Figure 7.4: Illustration of track coordinates d_0 and z_0 .

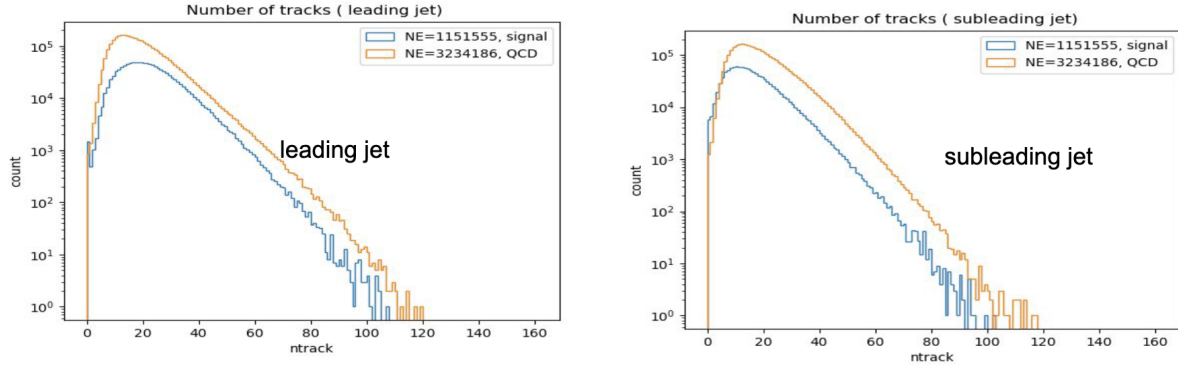


Figure 7.5: Distributions of the track multiplicity in the leading and subleading jets, comparing signal and background PFN training samples.

1380 These tracks (up to 160 total) are the input to the PFN. Referencing Equation 7.1, this corre-
 1381 sponds to $M = 160$ and $d = 6$. The two leading jets and their associated tracks are rotated so
 1382 that the center of the system is aligned with $(\eta, \phi) = (0, 0)$. Each track is normalized to its relative
 1383 fraction of the total dijet system energy and transverse momentum- this enforces agnosticism to the
 1384 total energy and transverse momentum of the event. The rotation and scaling are motivated by the
 1385 procedures described in [69] to improve the optimality of the PFN learning. Figure 7.6 illustrates
 1386 the rotation process.

1387 Finally, each of the 6 track variables is scaled so that its range is $[0,1]$. This is a common

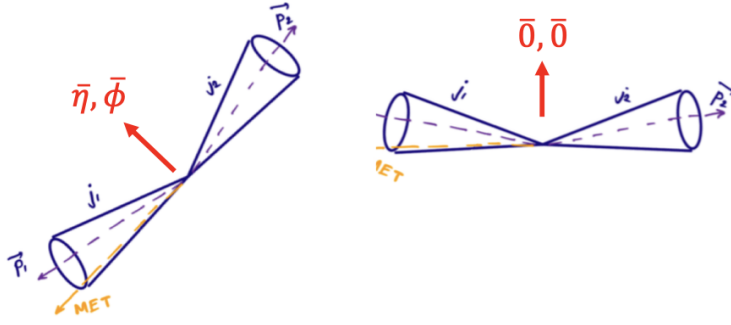


Figure 7.6: A diagram demonstrating how the two jet system is rotated in (ϕ, η) .

1388 preprocessing step that ensures the input data is bounded over a similar range, so that arbitrarily
 1389 large values don't develop an outsized impact on the model. Figure 7.7 show each of 6 track
 1390 variables before and after scaling and rotation have been applied, demonstrating the impact of
 1391 these procedures, as well as the track level similarities differences between the background SM
 1392 QCD processes and the signal SVJ processes. Figure 7.8 illustrates that the data is well modeled
 1393 by the MC at track level.

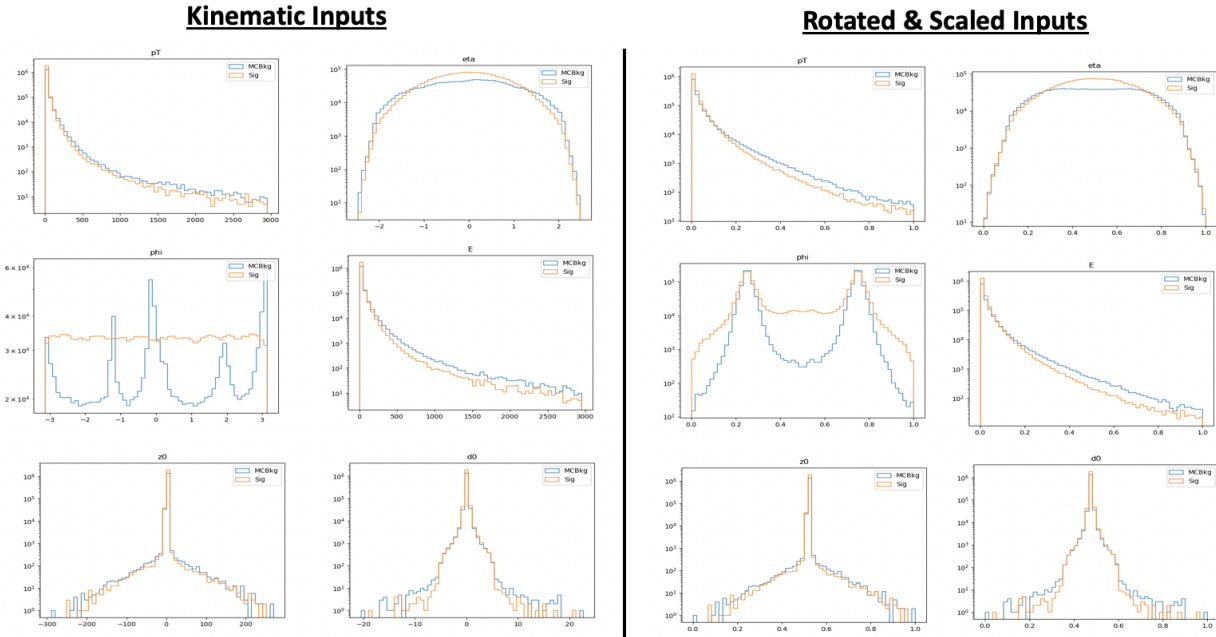


Figure 7.7: The 6 PFN track variables in background MC and signal MC. There are some differences between signal and background, but the track kinematics are largely similar.

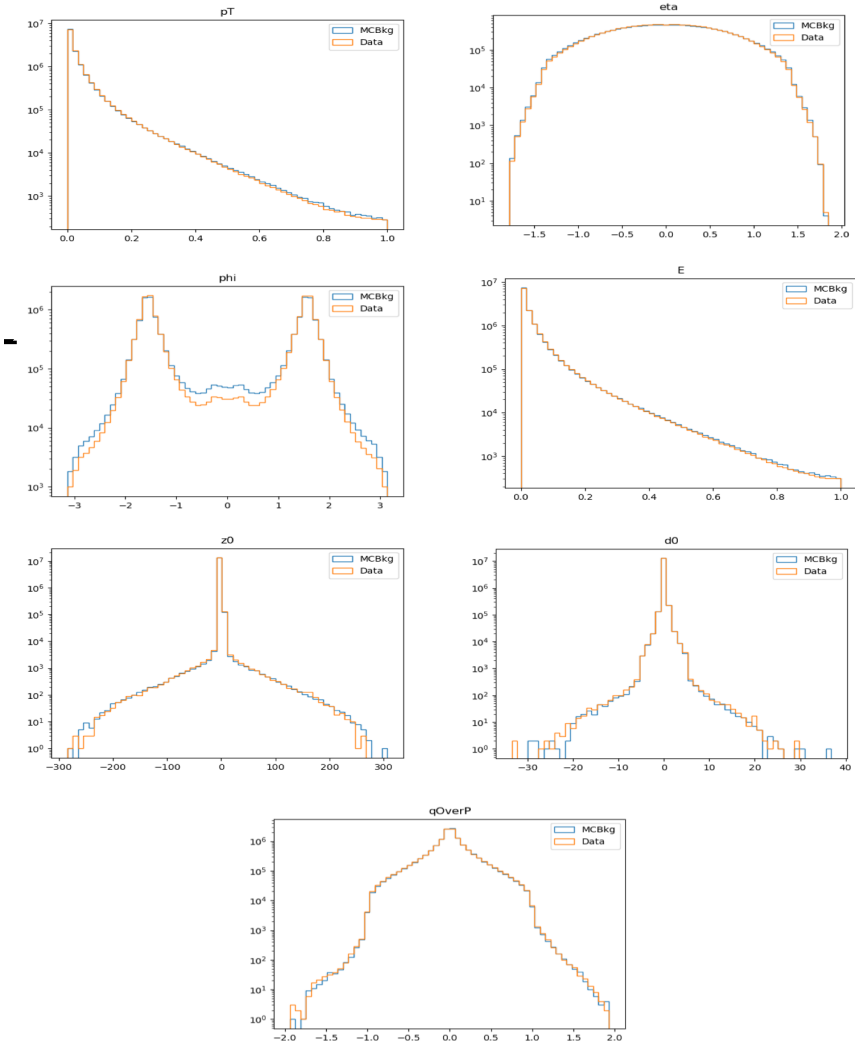


Figure 7.8: The 6 PFN track variables in data and background MC, after the scaling and rotation procedure is applied. There is excellent modeling of the data by the MC within the track variables. The slight discrepancy in the ϕ distribution is due to the modeling of dead TileCal cells by the QCD MC, which will be discussed in Chapter 8. The level of discrepancy is determined to be within tolerance given that the final result will be data driven and the QCD model is used in the PFN training only.

1394 **Training**

1395 As seen in Figure 7.2, two separate architectures are defined and combined to do the super-
1396 vised training. The PFN uses a masking layer to suppress any zero-padded inputs, making the
1397 architecture length agnostic. The masking layer ignores any all-zero inputs in the summation layer.
1398 Additionally, The summation layer in the PFN enforces permutation invariance, so the network is
1399 unordered. The Φ network has 3 dense layers of dimensionality 75 with RELU activation, with
1400 27.5k trainable parameters and an output Φ latent space dimension of 64.

1401 The classifier F network similarly has 3 dense layers with 75 nodes with RELU activation, and
1402 a final softmax layer to determine the event-level classification with a categorical cross-entropy
1403 loss. The Adam optimizer is used with an initial learning rate of 0.001.

1404 The PFN is trained in a fully supervised way using SVJ signal MC and QCD MC events. Al-
1405 though several SM processes are expected to contaminate the SR (see Chapter 8), QCD is the dom-
1406 inant background. Training against a QCD-only sample is determined to produced better results
1407 than training on a more complete background - when training with a background which repre-
1408 sents samples that are more enriched in E_T^{miss} , the ability of the PFN to identify high E_T^{miss} signals
1409 is reduced. When training with a QCD-only background, there is greater contamination from
1410 E_T^{miss} enhanced backgrounds in the final SR - however the increased signal acceptance means that
1411 overall sensitivity is still higher with a QCD-only training. This can be seen in the comparison of
1412 output classifier distributions in Figure 7.9.

1413 500k events from both background and signal are used in training, where the signal is a com-
1414 bined file of all simulated signal points and the full QCD background which is sampled according
1415 to it's MC weights to produce the proper p_T input shape. A study was done to check the optimality
1416 of the inclusive signal model PFN as compared to one trained on high and low R_{inv} points sepa-
1417 rately, to better capture the differences in high and low E_T^{miss} across signals and backgrounds, but
1418 a small effect is found and the decision is taken to keep the inclusive model (Appendix B.2).

1419 The network is trained for 100 epochs. A train/test/validation split of 78%, 20%, and 2% is used
1420 for the final PFN training. Figure 7.10 shows the loss during training, which is stable and flattens

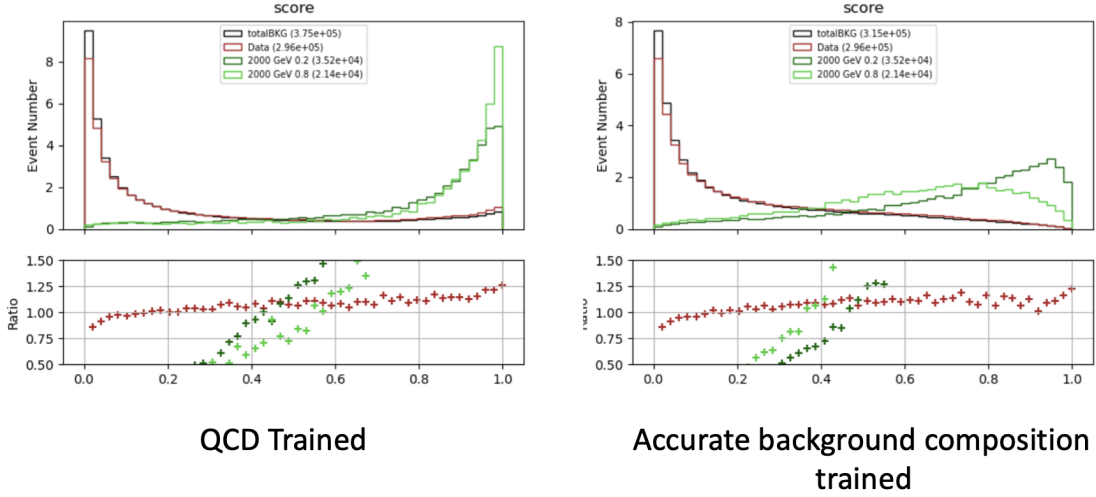


Figure 7.9: PFN score for background MC, data, and signal, comparing a PFN training on QCD-only vs all-background MC samples. The average AUC for the QCD-only training (left) is 0.93, while the average AUC for the mixed background training (right) is 0.84. The sensitivity estimate across the grid is better for the QCD-only training - from the distribution we can conclude that this is because the sensitivity to MET enhanced signals is greatly reduced.

1421 by the end of training, and the final evaluated losses that provide signal-background discrimination
 1422 over the test set.

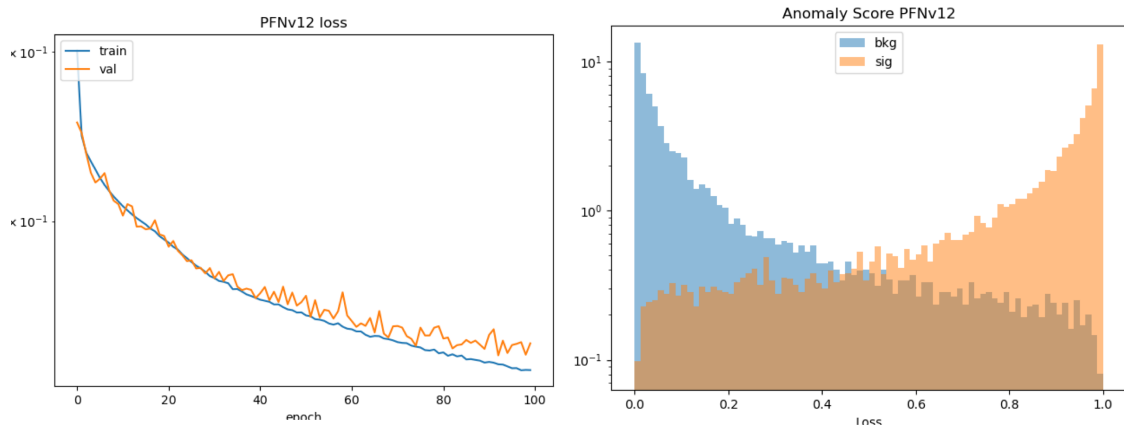


Figure 7.10: PFN architecture loss during training as a function of epoch (left) and the evaluated loss over the signal and background (right).

1423 Optimization studies were performed on the PFN, varying the number of training epochs, num-
 1424 ber of training events, batch size, learning rate, number of neurons, and dimension of the Φ space.
 1425 A summary of these studies is presented in Appendix B.2. The model presented here represents an
 1426 optimal choice across these parameters.

1427 **Performance**

1428 The performance of the PFN can be assessed via the area-under-curve (AUC) of the receiver
1429 operating characteristic (ROC) associated to evaluating the PFN on the test set of signal and back-
1430 ground events. Figure 7.11 shows the ROC curve of the PFN when classifying the QCD back-
1431 ground from the combined signal, with an AUC of 0.93. Figure 7.12 shows the AUC of the PFN
1432 across the SVJ signal grid, demonstrating strong discrimination capability even in the varying cor-
1433 ners of phase space. Figure 7.13 shows the output score distribution in two signals, data, and the
1434 total background MC. A selection of PFN score > 0.6 for all SR events is chosen to maximize
signal sensitivity across the grid.

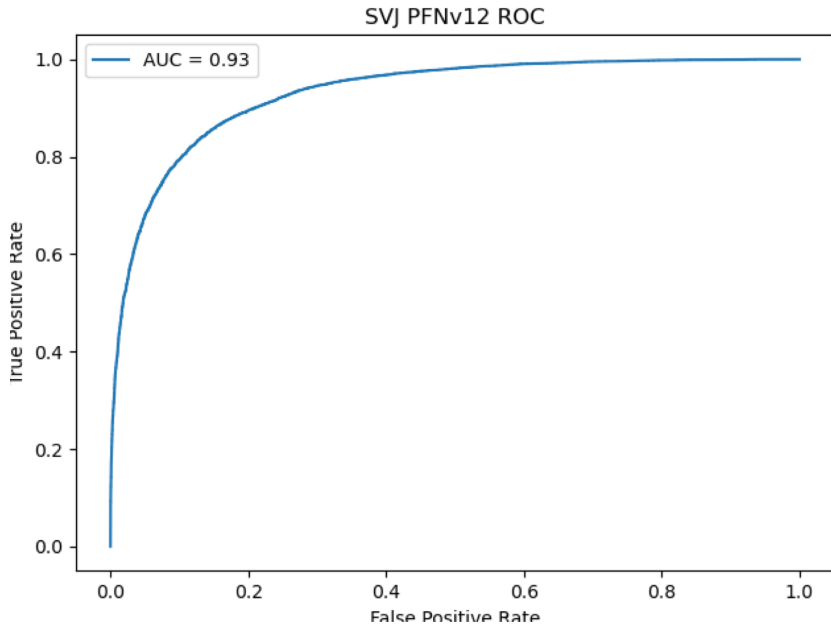


Figure 7.11: ROC the PFN score for combined signal (true positive) and QCD background (false positive).

1435

1436 Another supervised approach was studied using a BDT as the primary selection tool, trained
1437 over high-level variables describing each event. Studies comparing the PFN and BDT approaches
1438 are provided in Appendix B.3. Ultimately the low-level high-dimensional approach offered by the
1439 PFN was selected for its increased performance and lessened kinematic dependence.

1440 Appendix B shows more studies on the ML methods and comparisons of varying approaches.

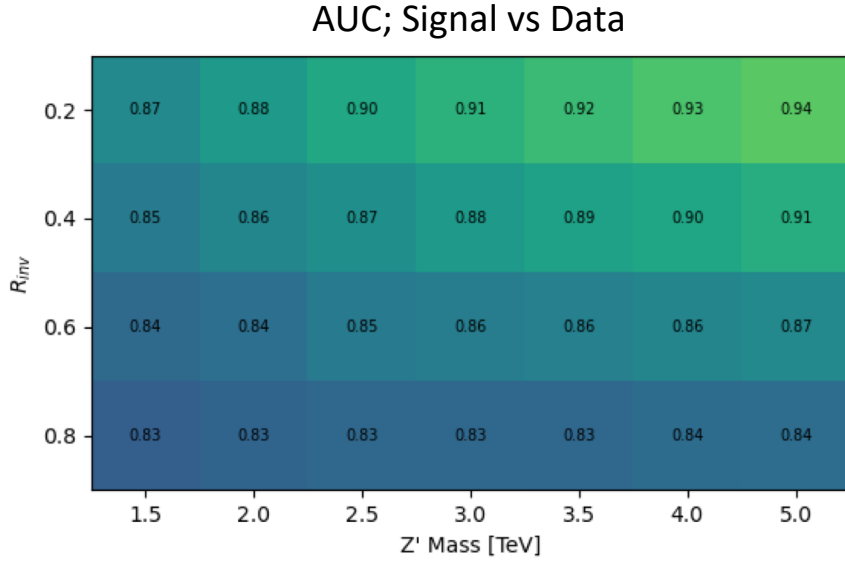


Figure 7.12: AUC from the PFN score for each signal in the SVJ grid, shown versus the QCD-only training sample.

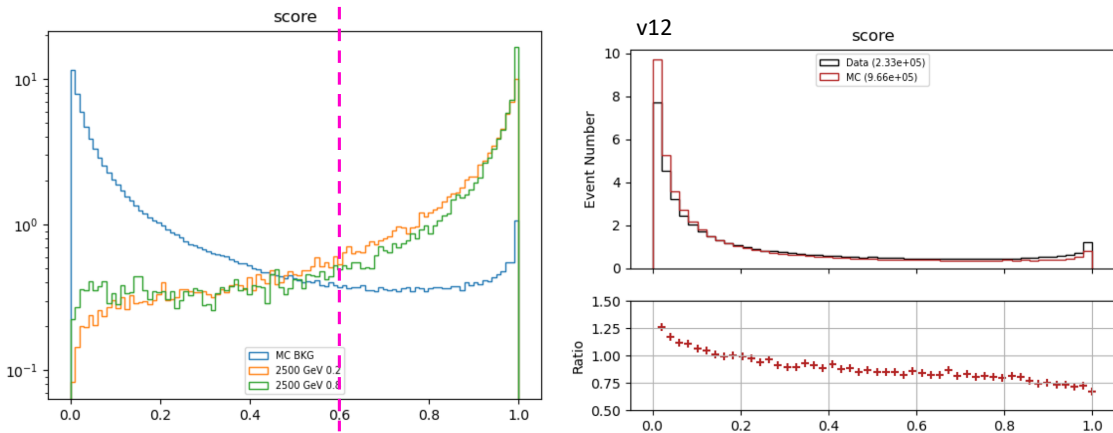


Figure 7.13: PFN score for two signals and the total background MC (top), and between data and MC (bottom). The difference between data and MC efficiency is minimal (< 5%).

1441 7.1.2 ANTELOPE (Semi-supervised)

1442 The semi-supervised analysis approach broadens the discovery sensitivity of the search through
1443 the use of semi-supervised ML, where training of the model is data-driven and labels are only
1444 partially provided during training. While broad sensitivity is a general key goal of LHC searches,
1445 it is particularly motivated in the case of dark QCD models, which can lead to widely varying
1446 topologies depending on the values of model parameters. In the case of SVJs, the R_{inv} fraction in
1447 the jet can dramatically vary the E_T^{miss} , shower shape, and other key features, making it difficult to
1448 find a single standard analysis variable that can distinguish all signal topologies from QCD.

1449 **Architecture Fundamentals**

1450 The model-independent search region of this analysis is implemented with a novel ML ap-
1451 proach that builds on the ANTELOPE architecture to construct a tool that is capable of performing
1452 low-level anomaly detection with permutation-invariant inputs. This tool, referred to as **ANomaly**
1453 **deTEction on particLe flOw latent sPacE (ANTELOPE)**, is a custom solution designed for this
1454 analysis.

1455 ANTELOPE uses the supervised signal vs. background training of the PFN network described
1456 in the previous section to generate a permutation invariant latent space that is representative of the
1457 original input variables, encodes the input events into these latent space variables O , and trains a
1458 *variational autoencoder* (VAE) over the events modeled as PFN latent space variables. A VAE
1459 is a common architecture used for anomaly detection and data-driven ML training. It has been
1460 used in previous ATLAS searched to model jet level information, such as the search presented
1461 in [71] using the recurrent architecture described in [70]. One of the limitations of a recurrent
1462 architecture is the need to order the low level inputs, which affects the performance of the tool. Jet
1463 constituent information is intrinsically unordered, and therefore a permutation invariant approach
1464 removes this element of arbitrary decision making from the modeling process. A visual example
1465 of the ANTELOPE inputs is given in Figure 7.14.

1466 The input to the model is the same 6 track variables for the leading 160 tracks of the leading

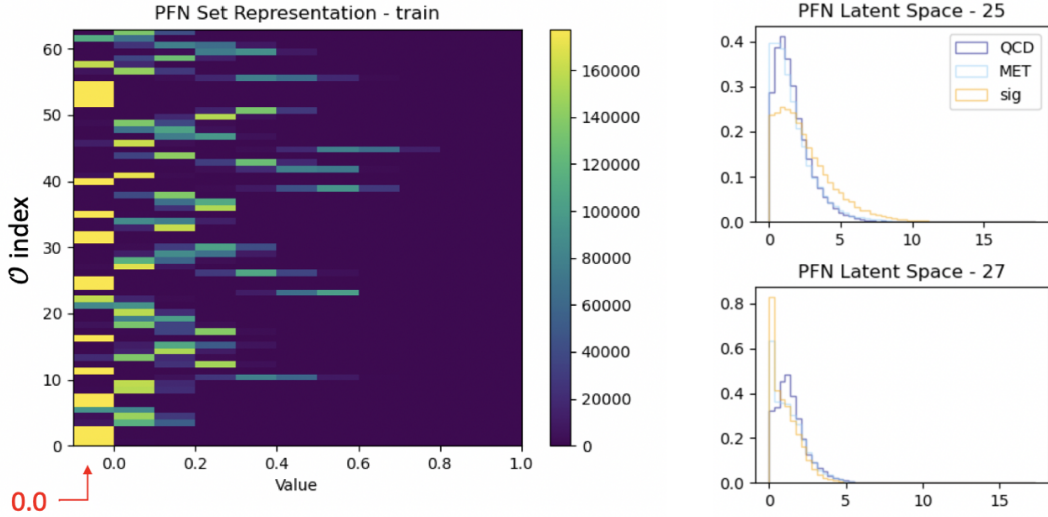


Figure 7.14: A visual representation of the 64 PFN latent space variables which create the input of the VAE component of ANTELOPE. The left shows a 2D histogram of the PFN latent space index (0-63) versus the value assumed by that index. The right shows 1D histograms of two particular PFN latent space variables.

1467 two jets, as presented in Section 7.1.1. The track information is encoded to the PFN Φ latent
 1468 space using the pre-trained Φ network (trained according to the steps outline in Section 7.1.1. The
 1469 resulting Φ basis is summed to created the fixed length symmetric representation O . The VAE is
 1470 then trained in an unsupervised way using inputs encoded to O from data events only. The VAE is
 1471 given no knowledge of the signal model during training. It is able to perform anomaly detection
 1472 through an encoder stage which does a lossy compression on the input to a lower-dimensional
 1473 latent space, and a decoder stage that samples from that latent space and generates an output of the
 1474 original dimensionality. By using the reconstruction error as a loss, this process enables the VAE
 1475 to develop a knowledge of the underlying data structure, thereby isolating new out-of-distribution
 1476 events by their high reconstruction error. This strategy is semi-supervised because the tool has
 1477 some knowledge of correct labels (eg. through the PFN latent space embedding) but is followed
 1478 by a data-driven unsupervised stage.

1479 Figure 7.15 provides a diagram of the ANTELOPE architecture.

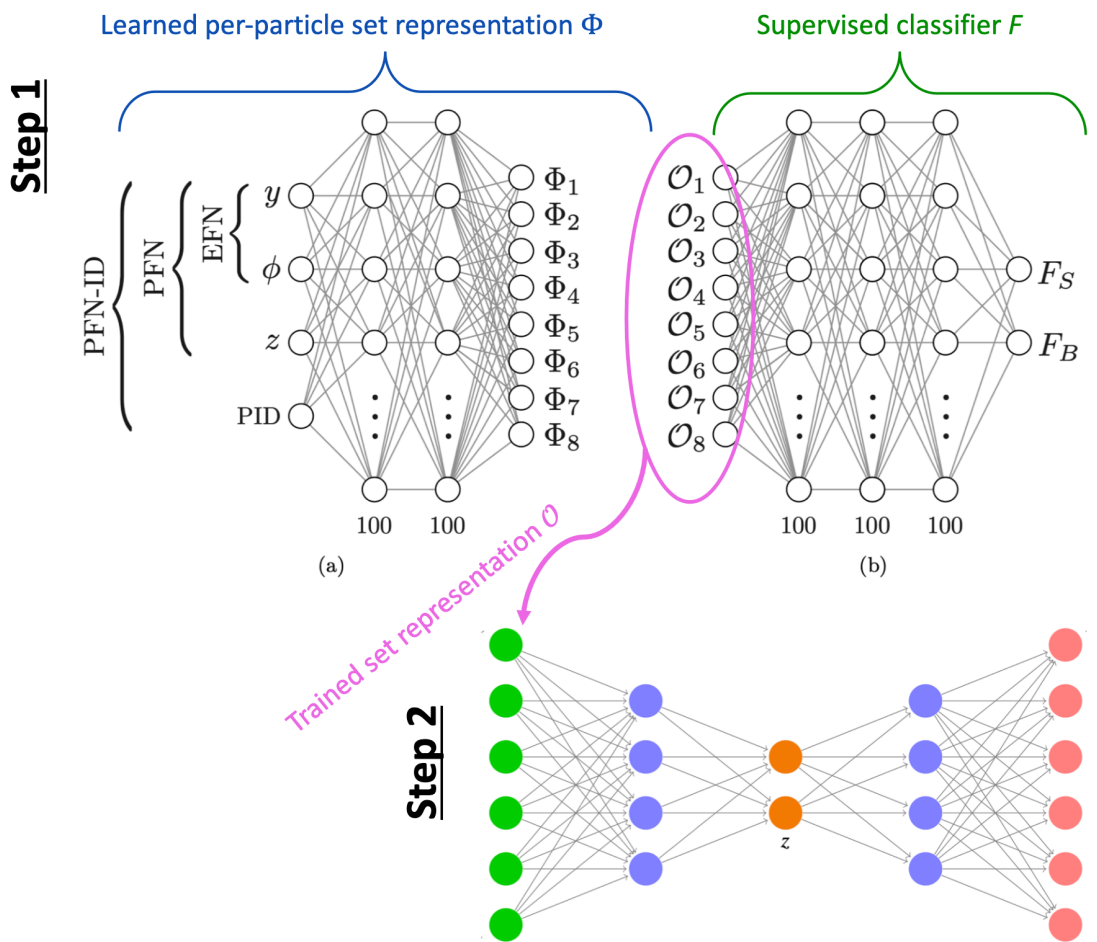


Figure 7.15: An annotated diagram of the ANTELOPE architecture.

1480 **Training**

1481 The VAE stage of the ANTELOPE network is trained directly over a subset of data events
1482 at preselection (6.7 million available, 500,000 used, with a 80% / 20% training/test split). The
1483 input dimensionality of the VAE has to match the encoded Φ dimension of the PFN, in this case
1484 64. The encoder has an encoding layer that brings the dimensionality to 32, and a final layer that
1485 compresses to the latent space dimension of 12. The network is trained for 50 epochs, with a
1486 learning rate of 0.00001. The loss \mathcal{L} is the sum of two terms, the mean-squared error (MSE) of
1487 input-output reconstruction, and the Kullback-Leibler divergence (KLD).

$$\mathcal{L} = \sum_i L_i = \sum_i |\Phi_i^2 - \Phi'_{\ell i}|^2 + \lambda D_{\text{KL}} \quad (7.2)$$

1488 As the PFN inputs are sufficiently normalized to remove any spurious information from train-
1489 ing, no additional normalization is applied to the PFN encoded inputs. The final ANTELOPE score
1490 used in the analysis is produced by applying a log + sigmoid transformation function to the total
1491 evaluated loss \mathcal{L} .

Figure 7.16 shows the loss during training.

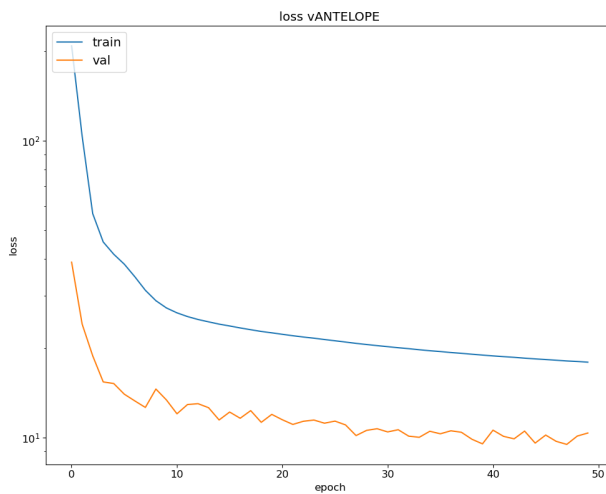


Figure 7.16: ANTELOPE architecture loss during training as a function of epoch.

1493 **Performance**

1494 As with the PFN, the ANTELOPE performance is assessed via the area-under-curve (AUC) of
1495 the receiver operating characteristic (ROC) associated to evaluating the ANTELOPE on the test
1496 set of signal and background events. Figure 7.17 shows the output score distribution in data and
1497 total background MC, showing a very flat ratio and motivating the use of MC for studies of the
1498 ANTELOPE score.

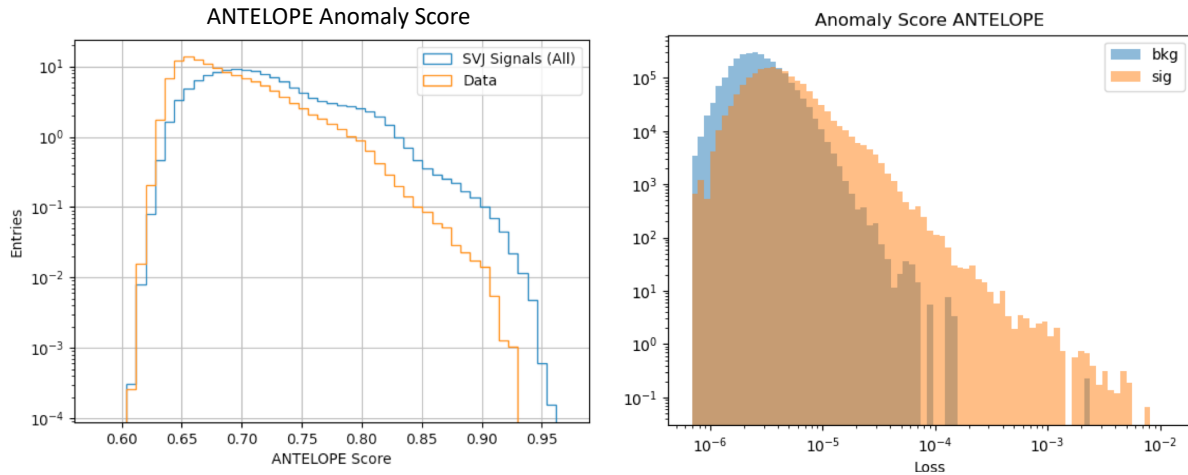


Figure 7.17: ANTELOPE score distribution comparing data and the total background MC (left), with good agreement observed between data and simulated background, and comparing all background MC to signals (right), revealing good discrimination power.

1499 Figure 7.18 shows the AUC of the ANTELOPE across the SVJ signal grid, demonstrating
1500 strong discrimination capability even in the varying corners of phase space. Compared to the
1501 supervised PFN method, the ANTELOPE is not as performant (as expected due to the absence of
1502 signal model in training). However, a selection on events with high ANTELOPE score nonetheless
1503 provides a 10-40% increase in signal significance by removing background and isolating the long
1504 tail of anomalous events.

1505 **Model Independence** The unsupervised component of training the ANTELOPE network is ex-
1506 pected to give it a more generalized sensitivity to new physics with E_T^{miss} and jet activity, beyond
1507 the scope of the SVJ grid. To assess this, alternative signal models are evaluated with the trained

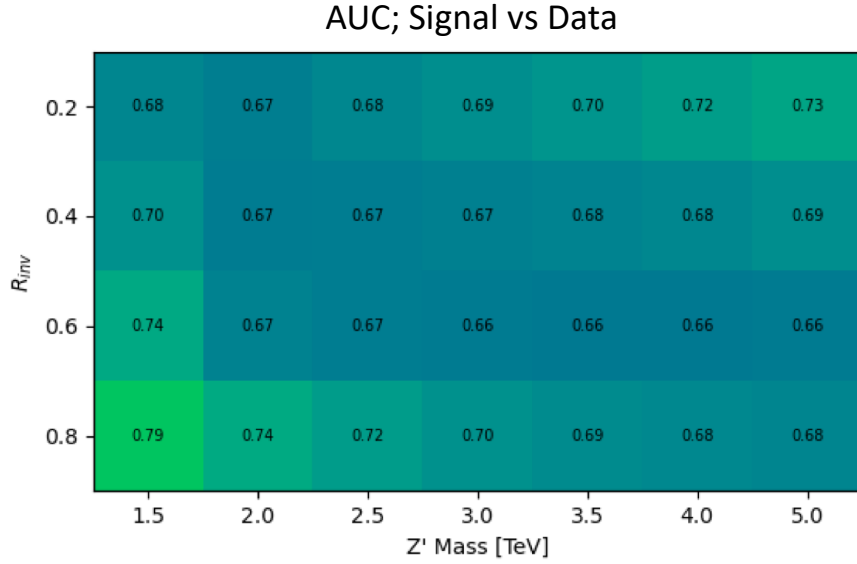


Figure 7.18: AUC from the ANTELOPE score for each signal in the SVJ grid.

1508 ANTELOPE network, as optimized for the SVJ grid, and their sensitivity in the analysis selection
1509 is evaluated.

1510 The following alternate signal models were considered:

- 1511 • $Z' \rightarrow t\bar{t}$
1512 • $W' \rightarrow WZ$
1513 • Gluino pair production \rightarrow R-hadron + LSP (E_T^{miss}) with gluino masses 2000/3000 GeV, LSP
1514 mass 100 GeV, and lifetime 0.03 ns (LSP = *lightest supersymmetric particle*)
1515 • Emerging jets s-channel with mass 1000 GeV and lifetime 1ns

1516 Figure 7.19 shows the distribution of these signals in the PFN score and the ANTELOPE score.
1517 This comparison reveals that ANTELOPE is sensitive to E_T^{miss} in the event; it classifies signals
1518 with no real E_T^{miss} , like the all-hadronic Z' and W' decays (given our imposed lepton veto) as
1519 data-like, but the distributions for signals with E_T^{miss} such as SVJs, R-hadrons, and emerging jets
1520 have distributions with higher anomaly score tails.

1521 Figure 7.20 shows a comparison of the sensitivity of the PFN and ANTELOPE regions across
1522 a variety of signals, including the combined SVJ signal used to train the PFN. The benefit of the

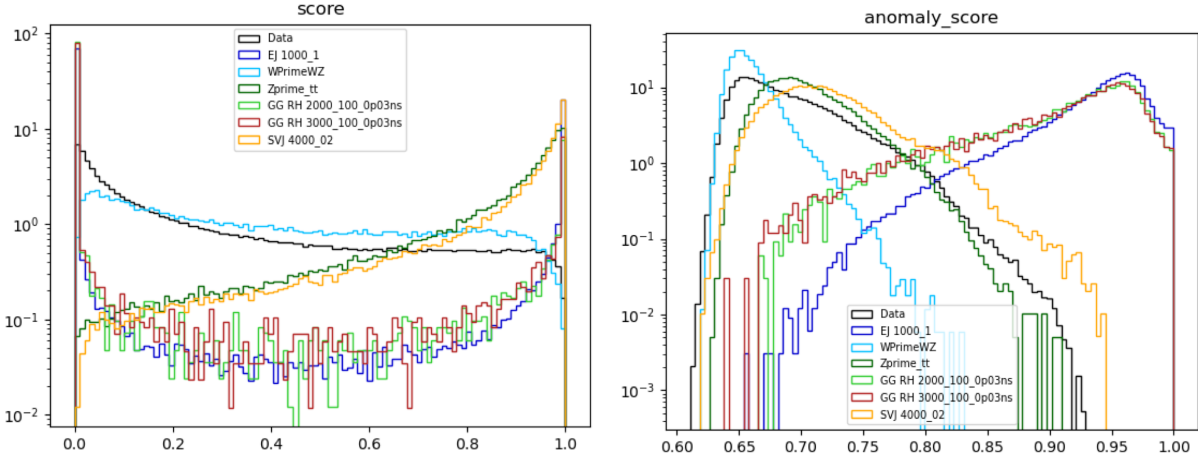


Figure 7.19: Comparing data and the alternate signal models for the PFN score (left) and ANTELOPE score (right). The emerging jet signal is an example of the gain of the model-independent ANTELOPE approach, where it has a bimodal shape in PFN score but is clearly tagged as anomalous by ANTELOPE.

1523 unsupervised stage of ANTELOPE in enhancing model independence is clearly seen through the
 1524 boost in performance for other signal models, namely the gluino and emerging jet signals, which
 1525 have more E_T^{miss} than the W' and Z' signals (all-hadronic) that were also tested. As commented
 1526 above, the PFN outperforms ANTELOPE as expected, because it was designed explicitly for the
 1527 task of classifying SVJs from background, demonstrating the power of supervised learning for the
 1528 model-specific approach.

$\text{sig eff} / \sqrt{\text{bkg eff}}$ for respective score cut (0.6 PFN, 0.7 ANTELOPE)

	EJ 1000	WprimeWZ	Zprime tt	GG RH 2000	GG RH 3000	SVJ
PFN	0.57	0.65	1.92	0.30	0.32	1.97
ANTELOPE	1.73	0.07	0.84	1.72	1.72	1.13

Figure 7.20: Comparing data and the alternate signal models in terms of sensitivity (S/\sqrt{B}) for the PFN and ANTELOPE tools, applying the selection that is used in the analysis. The ANTELOPE network is found to provide significant added sensitivity to alternate signals such as the gluino→R-hadron and emerging jets, which have higher E_T^{miss} than the SVJs.

1529 Studies on the ANTELOPE architecture and comparisons to other methods can be found in
 1530 Appendix B.1.

1531

1532

Chapter 8: Analysis Strategy

1533 This chapter will present the strategies used to isolate ATLAS data events most consistent with
1534 the SVJ model and to estimate the relevant background. The data and MC samples discussed in
1535 Chapter 6 are studied to create the analysis strategy, and the ML scores discussed in Chapter 7
1536 are used to isolate the most signal like events. A *preselection* selects events consistent with the
1537 SVJ topology based on basic features of the jets and E_T^{miss} . Preselected events are then split into
1538 a *control region* (CR), *validation region* (VR), and *signal region* (SR). The CR is used to estimate
1539 the estimate the background and the VR is used to validate that estimation. The SR is blinded
1540 during the development of the analysis strategy, and only unblinded to make the final measurements
1541 presented in Chapter 9. The final result is a polynomial fit of the *transverse mass* (m_T) spectrum
1542 in the SR. The preselection, region definitions, and polynomial fit will be discussed in detail in the
1543 following sections.

1544 **8.1 Preselection**

1545 The preselection isolates the phase space of events that most closely match the SVJ signal
1546 topology. Each cut was determined to reduced the background and enhance signal sensitivity. The
1547 list of preselection cuts and the motivation behind each cut are as follows. Here “jets” refer to
1548 anti- k_t R=0.4 jets, as discussed in Chapter 5.

- 1549 • At least 2 jets; in order to reconstruct the resonance mass
1550 • Leading jet $p_T > 450$ GeV; to ensure the use of the trigger in its efficiency plateau
1551 • Subleading jet $p_T > 150$ GeV; to mitigate the presence of non-collision background (Ap-
1552 pendix B.6.1)

- 1553 • $|\eta_{j1,j2}| < 2.1$; to ensure jets are fully within the tracker
- 1554 • $\Delta Y < 2.8$ (difference in rapidity between the two leading jets); to ensure central production
1555 associated to hard scatter
- 1556 • $E_T^{\text{miss}} > 200 \text{ GeV}$; to focus phase space on events with dark particles
- 1557 • $m_T > 1.2 \text{ TeV}$, to ensure a smoothly falling m_T distribution for fitting (Section 8.4)
- 1558 • At least 3 tracks for each of the two leading jets; to ensure good modeling
- 1559 • $\Delta\Phi(j_1, j_2) > 0.8$; to mitigate the presence of non-collision background (Appendix B.6.1).

A cutflow showing the impact of these cuts in data and signal is shown in Figure 8.1.

Data			Signals - All		
Cut	Statistics	Rel. Efficiency	Cut	Statistics	Rel. Efficiency
Initial	1.71E+10		Init	6.66E+05	
Trigger	3.45E+08	0.0202	Trigger	2.83E+05	0.4245
N. jets ≥ 2	2.84E+08	0.8233	N. jets ≥ 2	2.80E+05	0.9896
Leading Jet Pt $> 450 \text{ GeV}$	1.49E+08	0.5235	Leading Jet Pt $> 450 \text{ GeV}$	2.21E+05	0.7900
Lead Jet Eta < 2.1	1.42E+08	0.9528	Lead Jet Eta < 2.1	2.19E+05	0.9922
Subleading Jet Eta < 2.1	1.33E+08	0.9432	Subleading Jet Eta < 2.1	2.12E+05	0.9661
$dY < 2.8$	1.29E+08	0.9628	$dY < 2.8$	2.11E+05	0.9934
MET > 200	7.07E+05	0.0055	MET > 200	1.13E+05	0.5370
$mT > 1200$	5.38E+05	0.7613	$mT > 1200$	7.94E+04	0.7019
Jet2 pT > 150	5.03E+05	0.9343	Jet2 pT > 150	6.14E+04	0.7739
$d\Phi(j_1, j_2) > 0.8$	4.97E+05	0.9890	$d\Phi(j_1, j_2) > 0.8$	5.83E+04	0.9494

Figure 8.1: Preselection cutflow for data (left) and signal (right).

1560

1561 With the exception of the cuts necessary to reduce the non-collision background, all cuts were
1562 verified to enhance signal sensitivity by improving s/\sqrt{b} , a standard estimate of discovery sensi-
1563 tivity, where s is the number of signal events and b is the number of background events. The cuts
1564 on ΔY and E_T^{miss} were optimized to enhance s/\sqrt{b} , and the other cuts were informed by the physics
1565 motivations provided above.

1566 Vетос are applied to reject any events where an error for a subdetector is flagged. This covers
1567 Tile/LAr calorimeter errors, single event upsets in the SCT, and incomplete events. To reject non-
1568 collision backgrounds (NCB), such as calorimeter noise, beam halo interactions, or cosmic rays,

1569 the standard ATLAS event cleaning procedure is applied. As this analysis is very dependent on
1570 E_T^{miss} associated to jets, the TIGHT event cleaning working point is applied. Tight cleaning requires
1571 jets to pass a stricter set of quality requirements compare to the LOOSE cleaning option. Due to
1572 the alignment between jets and E_T^{miss} in this phase space, it was found that two additional cuts
1573 (indicated above) are needed to remove NCB. The process for selecting these cuts is presented in
1574 Appendix B.6.1.

1575 The two leading in p_T jets in the event are considered as the dark quark candidates. This choice
1576 was determined by truth studies matching the dark quark to reconstructed jets in simulation, which
1577 indicate that the leading p_T assignment allows for high accuracy in ΔR matching to dark quarks.
1578 These studies can be found in Appendix C.

1579 Figure 8.2 and Figure 8.3 show the distribution of signal and background MC in several key
1580 analysis variables after preselection is applied.

1581 **8.2 SVJ Fit and Discovery Analysis Strategies**

1582 As was introduced in Chapter 7 this analysis is interested in achieving dual goals: to make
1583 the best possible measurement of the SVJ signal model generated for this analysis, and to broadly
1584 search for any signals consistent with dark QCD behavior and inconsistent with a Standard-Model-
1585 only background hypothesis. To this end, two parallel analysis strategies are developed.

1586 The SVJ Fit strategy uses the supervised PFN ML score in defining the signal region. Recall,
1587 the PFN is trained over simulated MC background and a combination of all MC SVJ signals. This
1588 gives this ML tool high sensitivity to the particular nuances of the SVJ shower predicted by the
1589 modeled theory. In addition to using the supervised ML tool, the SVJ Fit analysis strategy sets
1590 limits on the expected cross-section of each signal point in the SVJ signal grid. To achieve this, the
1591 shape of the SVJ signals are considered in the final fit, as will be elaborated on Section 8.5.1. The
1592 combination of the supervised PFN ML score and the signal-shape sensitive fitting strategy allows
1593 for the greatest possible sensitivity to the modeled signal process, thus allowing the analysis the
1594 best chance at discovery of this model, or enabling the analysis to set the best possible limits on

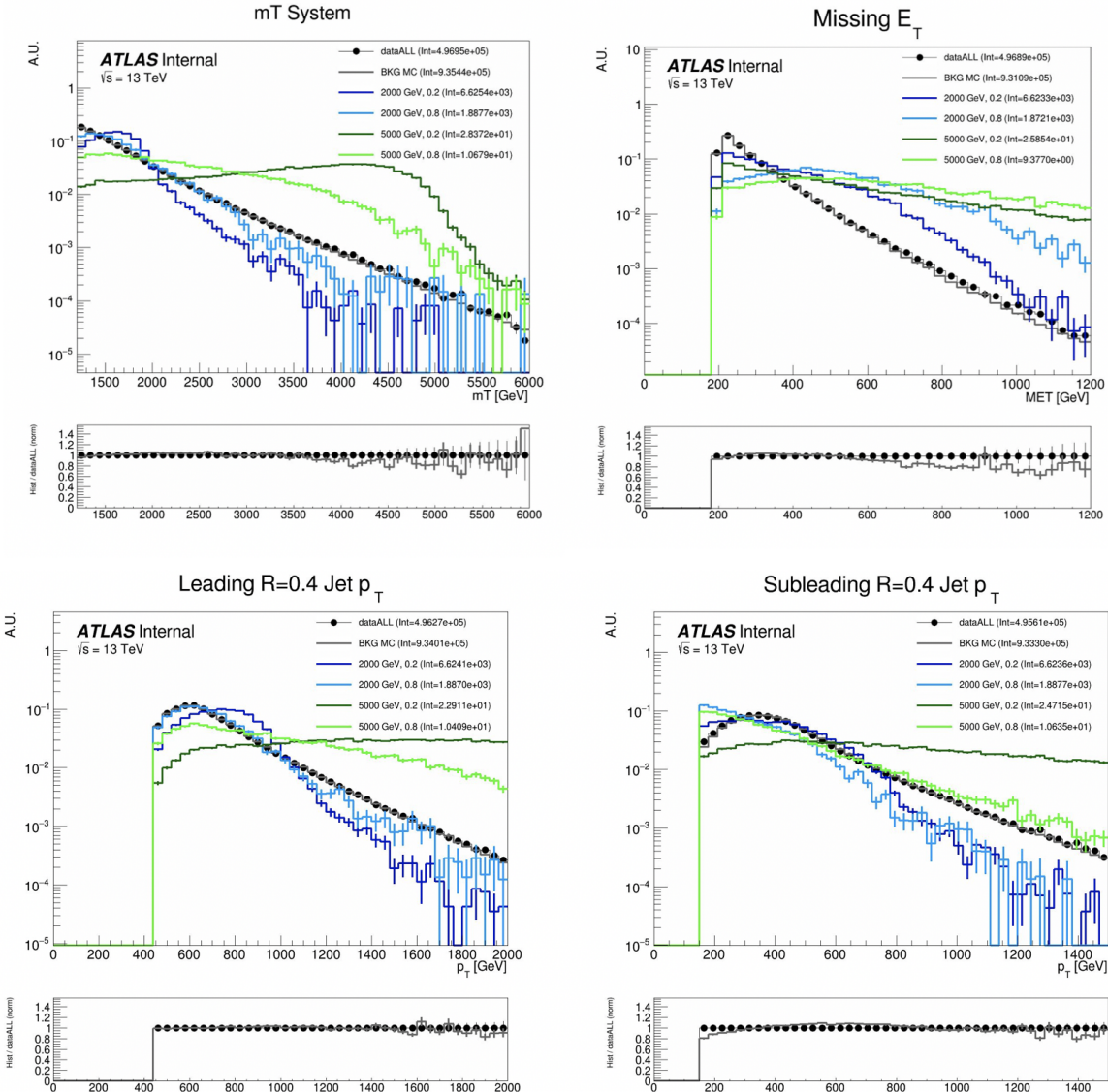


Figure 8.2: Energy and momentum analysis variables at preselection, for data, all background MC and representative signal models. m_T is the key fit variable, and this plot illustrates the smoothly falling background in comparison to the resonant shape of the signals. m_T is further illustrated in Figure 8.9.

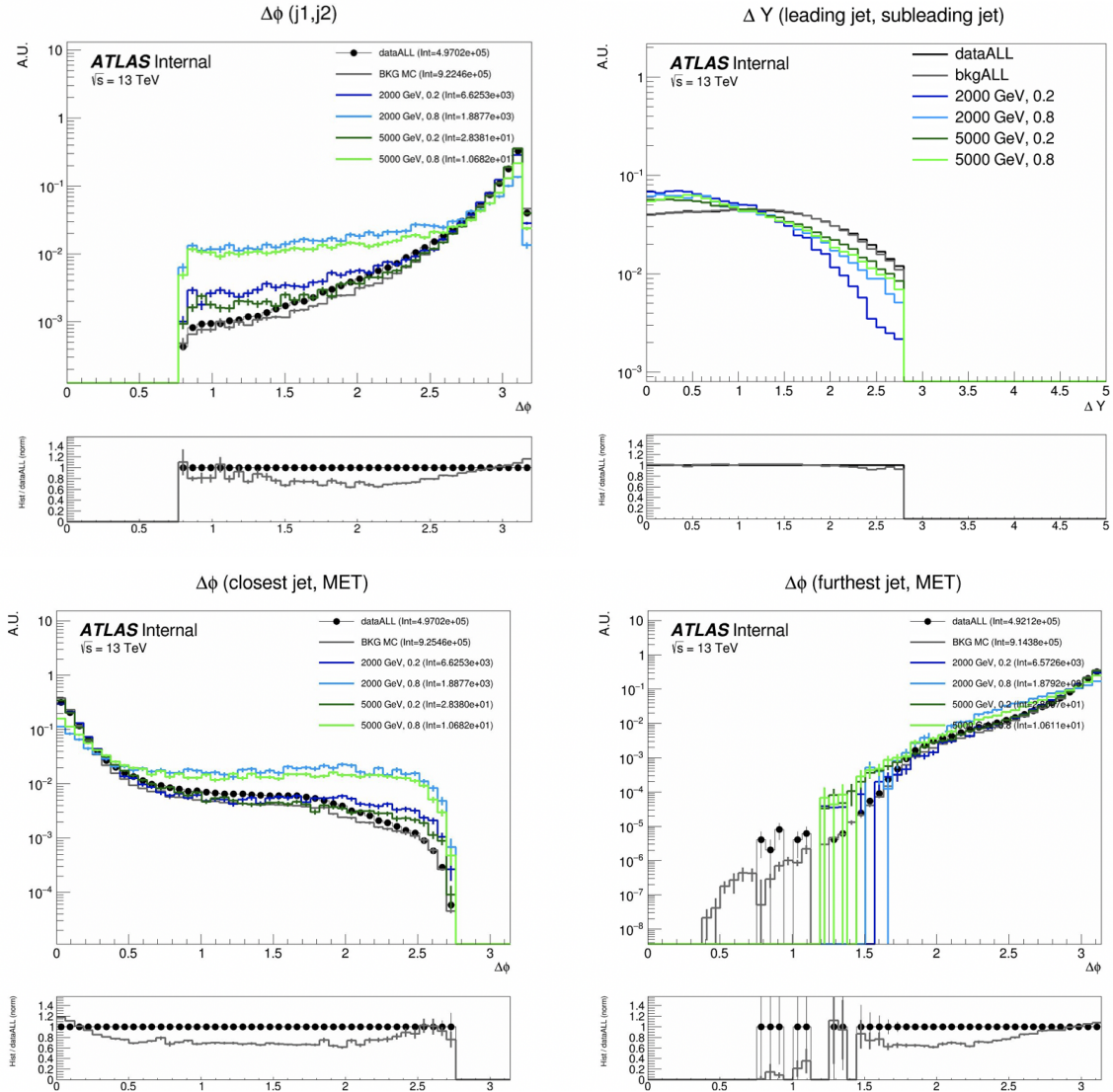


Figure 8.3: Orientation analysis variables at preselection, for data, all background MC and representative signal models. While $\Delta\phi(E_T^{\text{miss}}, j)$ variables are not used explicitly in the analysis flow, they help create a picture of the event.

1595 the observed cross-section.

1596 In contrast, the Discovery analysis strategy attempts to design a more general search, which
1597 could be sensitive to SVJs, but also to other possible hidden valley dark QCD models, such as
1598 fully dark jets or emerging jets [21]. The Discovery analysis strategy uses the semi-supervised
1599 ANTELOPE ML score in defining the signal region. Recall, the ANTELOPE is trained over AT-
1600 LAS data only, with no explicit knowledge of the SVJ signal behavior. The Discovery fit strategy
1601 is also signal model agnostic, by employing a bump hunt [72] strategy, which searches a smoothly
1602 falling template for any bumps inconsistent with a background only hypothesis. Therefore any
1603 signal which could present a resonant signature in m_T could show up as an excess in this strategy.

1604 The details of both strategies will be explored in the follow sections which detail the design
1605 of the signal regions and fit strategies. A diagram demonstrating the analysis flows can be seen in
Figure 8.4. Details on each selection and region can be found in the following subsections.

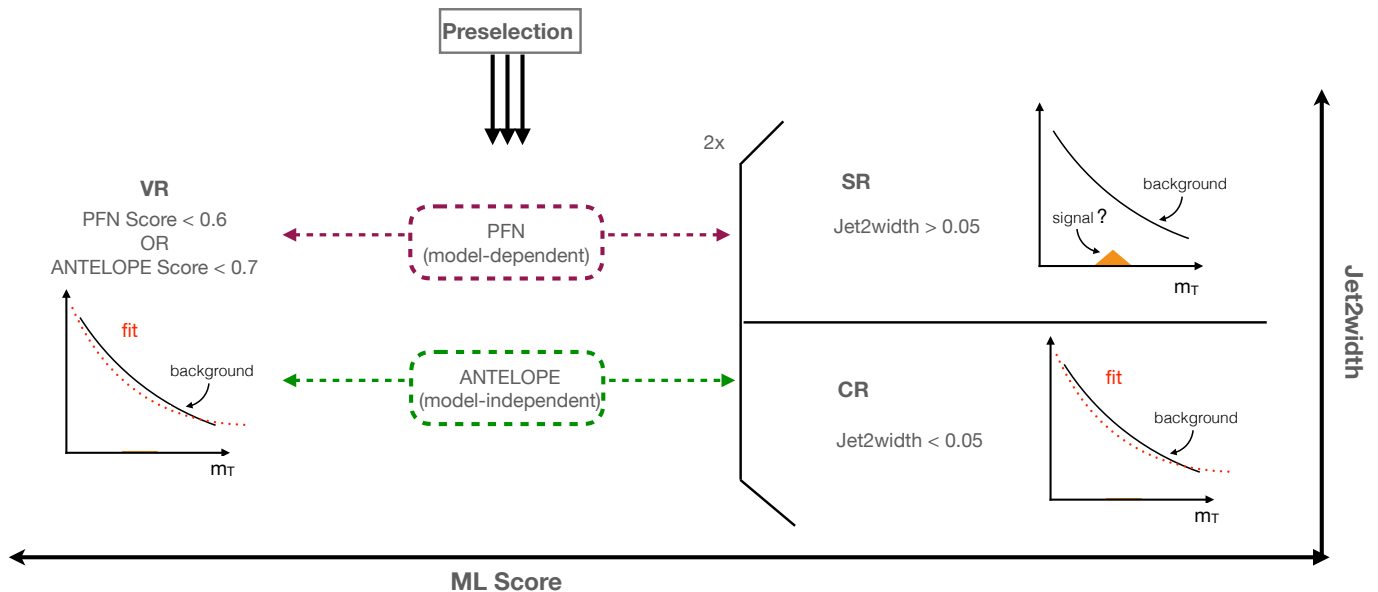


Figure 8.4: Flow of analysis selections, regions, and background estimation/validation fitting strat-
egy. TODO: diagram needs to be corrected

1606

1607 **8.3 Analysis Regions**

1608 **8.3.1 Control and Validation Regions**

1609 The final background estimation will come from a polynomial fit to the m_T distribution in the
 1610 signal region. The control and validation regions are needed to develop and test this fit in data.

1611 To define the CR selection, a variable is needed that isolates background from all signals across
 1612 the (R_{inv}, m_Z) grid, which is challenging due to the varying nature of the signal models in quantities
 1613 such as E_T^{miss} and p_T balance, as illustrated in Figure 8.2. The variable *jet width* is chosen, which
 1614 is the calorimeter measurement of the width of a small-R jet as defined by the distance between
 1615 the cluster and the jet axis scaled by the jet energy [73]. Figure 8.5 shows this variable specifically
 1616 for the subleading jet width, in data, background MC and signal at preselection. The leading jet
 1617 width, which was determined to be less useful for isolating signal from background is also shown.
 1618 The subleading jet is more likely to be the jet aligned with MET, which is why the signal jet width
 1619 is consistently wider in the subleading jet, but not the leading jet. A selection of $\text{width}_{j2} < 0.05$ is
 1620 chosen for the CR, with the VR and SR therefore having a selection of $\text{width}_{j2} \geq 0.05$.

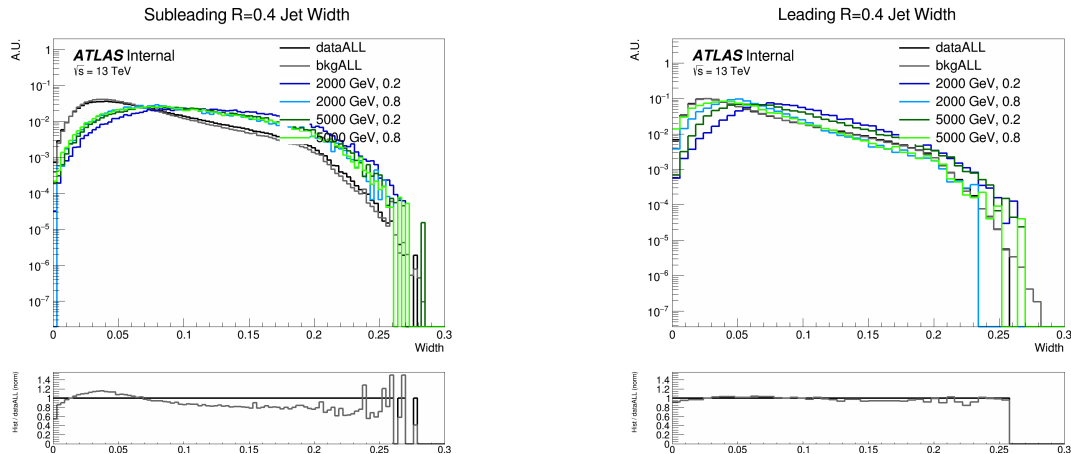


Figure 8.5: Distributions of the subleading jet width width_{j2} (left) and leading jet width width_{j1} (right) in data, background MC and signals at preselection. All SVJ signals are seen to be wider than the background in width_{j2} . The same is not true for width_{j1} , where some signals are observed to closely match the background.

1621 While the CR was used to develop the polynomial strategy, and is the primary region used in

many of the fit studies, a validation region is used as an additional check of the estimation strategy
 in data. The VR is defined using the region of events with low ML score by either the PFN or
 ANTELOPE networks. Here the analysis strategy splits into the two parallel strategies presented
 in Section 8.2: the SVJ fit strategy and the Discovery strategy. A selection of [PFN score ≤ 0.6
 $\& \text{width}_{j2} \geq 0.05$] defines the SVJ Fit VR, while [ANTELOPE score ≤ 0.7 & width $_{j2} \geq 0.05$]
 defines the discovery VR.

There are therefore three variables that are crucial to the analysis strategy: width $_{j2}$, ML score,
 and m_T . Figure 8.6 shows the correlations of all three variables to one another. Any outstanding
 correlations are shown in Figure 8.7 to not sculpt the m_T distribution and only affect its slope,
 making these variables trustworthy for extrapolation across background/signal regions and final
 fitting procedures.

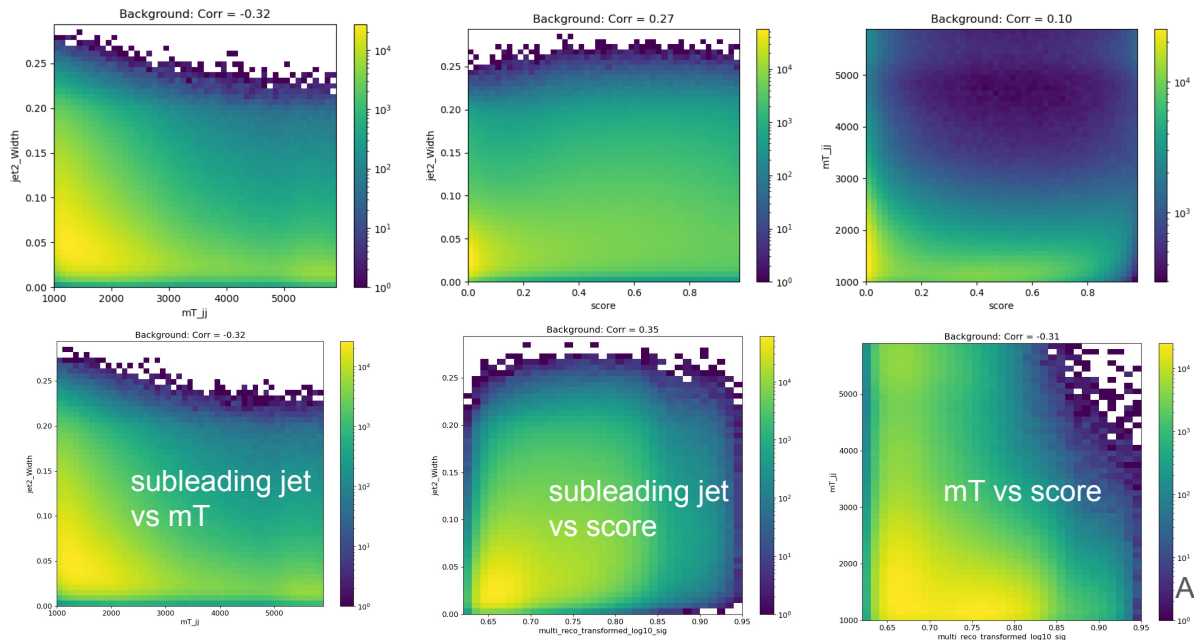


Figure 8.6: 2D plots revealing correlations between width $_{j2}$ and m_T (left), width $_{j2}$ and ML score (middle), and m_T with ML score (right). For the top row, the ML score is the PFN score, and for the bottom three, the ML score is the ANTELOPE score. Minimal correlations are observed and are shown to not sculpt m_T , validating these variables for analysis region construction and statistical treatment.

The most important variable for shape robustness across the CR, VR, and SR is m_T , as this
 is the variable that is fit for the statistical results. Figure 8.7 shows the distribution of m_T across

1635 the CR, VR, and SR, for both the PFN (supervised) and ANTELOPE (semi-supervised) strategies.
 1636 Some slope is observed in the ratio of the CR to the VR/SR shapes; however, the chosen back-
 1637 ground estimation strategy of polynomial fitting is expected to accommodate this slope. Further,
 1638 the ability of the background polynomial to fit both tail shapes will flex the fit framework in a
 1639 way that will generate higher confidence in the final ability to fit the SR. No significant bumps or
 sculpting are observed.

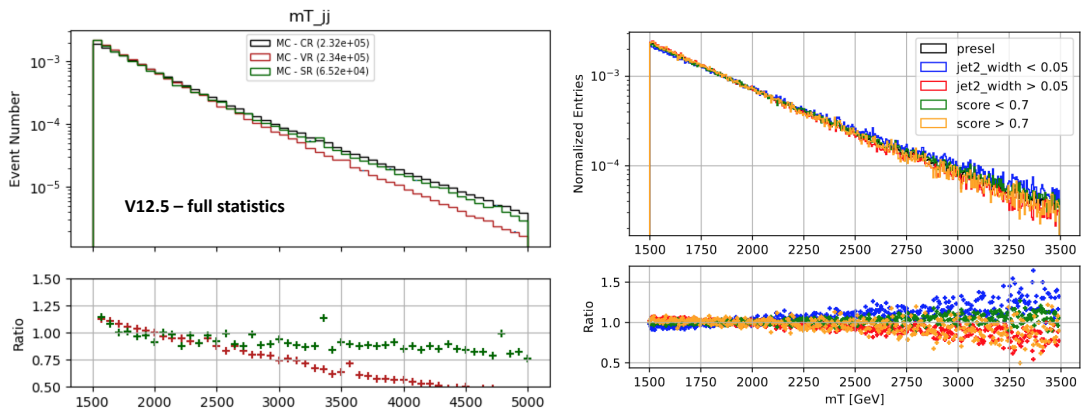


Figure 8.7: m_T in simulation across the CR, VR, and SR for both PFN (left) and ANTELOPE (right) selections.

1640

1641 8.3.2 Signal Region

1642 A selection of PFN score > 0.6 in the SVJ Fit region and ANTELOPE score > 0.7 in the
 1643 Discovery region is made to provide the primary signal-to-background enrichment, as motivated
 1644 by Section 7.1.1. These values are determined to maximize s/\sqrt{b} in each region. The additional
 1645 selection of $\text{width}_{j2} \geq 0.05$ orthogonalizes the SR to the CR. Note that the PFN and ANTELOPE
 1646 regions are not orthogonal; this is because the two analysis flows serve different purposes, their
 1647 statistical treatments are different, and they will not be combined.

1648 A summary of the SR, CR, and VR definitions can be seen in Figure 8.8, along with the relative
 1649 data statistics in each region.

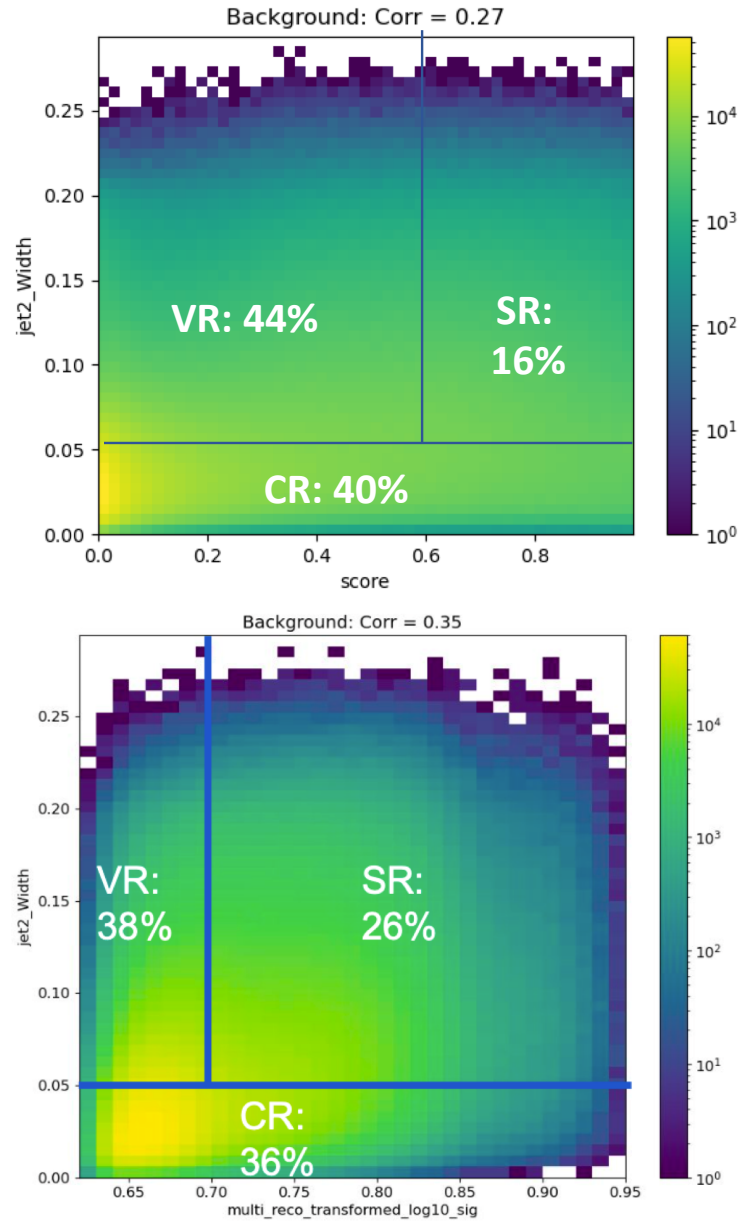


Figure 8.8: Definition of CR, VR, and SR regions using width_{j2} and the ML score, along with the population of each region in data statistics. The SVJ Fit region is shown on top with the PFN score on the x-axis, and Discovery region is shown on the bottom, with the ANTELOPE score on the x-axis.

1650 8.4 Background Estimation

1651 The transverse mass m_T is chosen as the search variable due to the potential for the SVJ signal
 1652 to create a resonant shape around the mass of the Z' . m_T is the total transverse mass of the two
 1653 leading jets and the E_T^{miss} , expressed in Equation 8.1 as:

$$1654 m_T^2 = [E_{T,jj} + E_T^{\text{miss}}]^2 - [\vec{p}_{T,jj} + \vec{p}_T^{\text{miss}}]^2 \quad (8.1)$$

1654 where $E_{T,jj}$ is the transverse energy of the dijet system. We take $E_{T,jj} = m_{jj}^2 + |\vec{p}_{T,jj}|^2$, where
 1655 m_{jj}^2 is the invariant mass of the two leading jets, and $\vec{p}_{T,jj}$ is the vector sum of the p_T of the two
 1656 leading jets. m_T is selected as the search variable in place of simpler invariant mass m_{jj} because
 1657 substantial energy from the Z' decay is captured in the E_T^{miss} . Therefore incorporating E_T^{miss} into
 1658 m_T improves the resonance around the mass of the Z' .

Figure 8.9 illustrates the resonance in m_T of the SVJ signals.

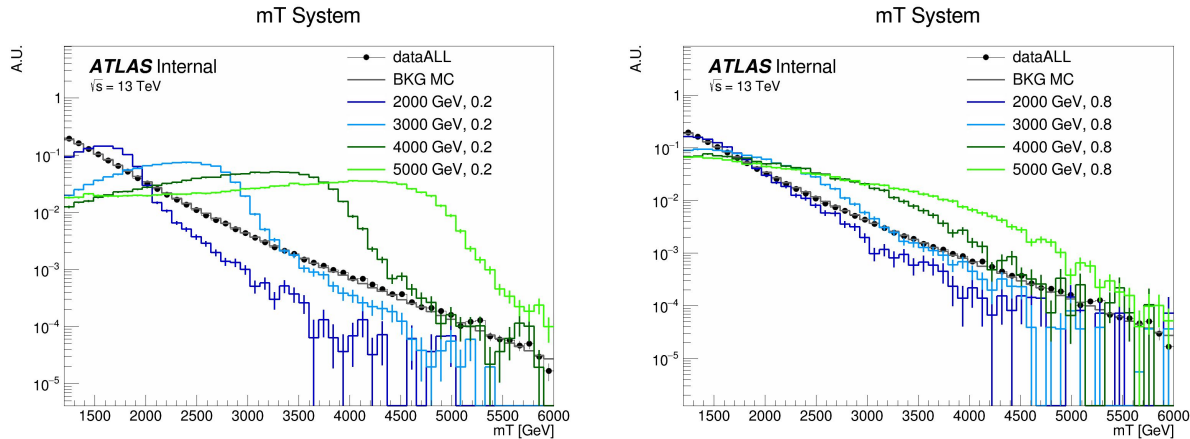


Figure 8.9: The resonant shape of the SVJ signals in m_T , in contrast to the smoothly falling m_T background. The high R_{inv} signals (right) boast a wider shape, making them more difficult to detect, while the low R_{inv} signals (left) produce a more narrow resonance in m_T .

1659
 1660 The SM background in the SR is predominantly composed of QCD events, and due to the poor
 1661 modeling of QCD at high energies by MC, it is estimated in a fully data-driven way. An empirical
 1662 functional form is used for the background shape of m_T . The ability of this function to model
 1663 the background behavior is tested both the CR and the VR for each analysis strategy. The shape

1664 parameters are left free in all the fits.

1665 The fits are performed for $1500 \text{ GeV} < m_T < 6000 \text{ GeV}$. The polynomial chosen is a standard

1666 5-parameter function used in several similar dijet search analyses such as [74] [75] [76] and shown

1667 in Equation 8.2:

$$f(x) = p_1(1 - x)^{p_2}x^{p_3+p_4\ln x+p_5\ln^2 x} \quad (8.2)$$

1668 Here $x = m_{jj}/\sqrt{s}$ and the p_i are free parameters. The fit function is required to be fully positive, and

1669 the m_T distribution is fit to 90 even-width bins. The resulting fit shape is used as the background

1670 estimation for both the SVJ Fit strategy and the Discovery strategy. Validation of the fit and its

1671 ability to both model the background and detect signal are shown in Section 8.5. Higher order

1672 polynomials were also considered, but an F-test was performed and the five parameter function

1673 was determined to be adequate and optimal for capturing the shape of the background.

1674 **8.5 Fit Strategy and Validation**

1675 The steps taken to validate the fitting approach for both the SVJ Fit strategy and the Discovery

1676 strategy will be outlined in the following sections. The signal region fits which compromise the

1677 final result will be presented in Chapter 9.,

1678 **8.5.1 SVJ Fit Strategy**

1679 The ability of the five parameter fit function to capture the shape of the background is studied

1680 extensively, using data from the CR and VR. Signal injection tests are performed to determine the

1681 ability of the fit to recover and quantify any SVJ signal excess. Finally, estimates of the expected

1682 sensitivity are made.

1683 **Background Only Fits**

1684 Three validations are used for the background fit polynomial: MC across all analysis regions,

1685 data in the CR and VR, and pseudo-data in the CR and VR.

1686 Figure 8.10 shows the ability of this polynomial to fit the smoothly falling m_T background in
 1687 simulation across all 3 analysis regions (CR, VR, SR). The m_T spectrum is fit in 90 even bins.
 1688 These distributions are obtained by downsampling the MC statistics to match the relevant statis-
 1689 tics of the data region, in accordance with the MC weights. The high background-only p -value
 indicates a good fit.

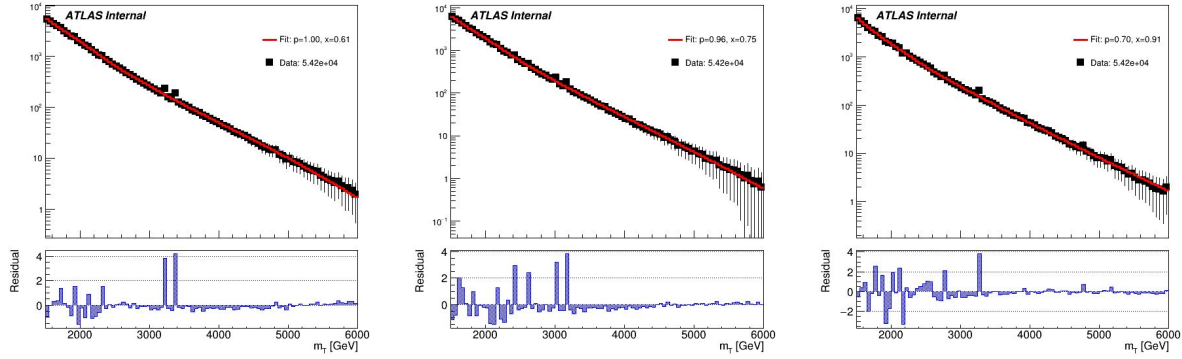


Figure 8.10: Background-only m_T fits using representative MC in the CR (left), VR (middle), and SR (right).

1690
 1691 A slight sinusoidal pattern in the residuals may be observed. This arises due to the “stitching”
 1692 together of the p_T slices for the QCD MC (as shown in Figure 6.1), which is picked up by the
 1693 fit. For this reason, fitting to MC is only checked to verify that the differences in the slope of
 1694 m_T between the three regions (as shown in Figure 8.7) do not pose a problem for the fitting strategy.

1695 After verifying the background modeling in all analysis regions in simulation, it is tested in
 1696 two data regions, the CR (low jet2width) and the VR (low ML score) which are orthogonal to
 1697 the blinded SR Figure 8.11 shows the a successful fit performed on the full statistics CR and VR
 1698 regions.

1699 Figure 8.12 shows the post-fit values of the fit parameters and their uncertainties for each fit.
 1700 TODO: recalculate so it matches plot

1701 Recall Figure 8.8, which illustrates that the statistics of the CR and the VR are almost 3x the
 1702 expected statistics of the SR. The polynomial fitting strategy is sensitive to the statistics of the fitted
 1703 template, and can perform differently To mitigate this, each template m_T histogram is obtained
 1704 by randomly sampling the data in the CR/VR until a sample that is *statistically identical* to the

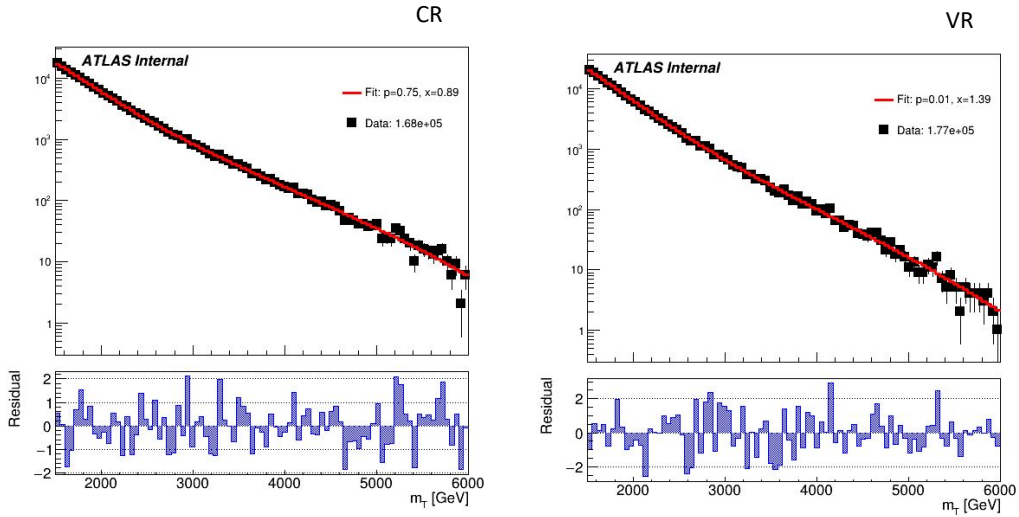


Figure 8.11: Background-only m_T fits using data in the full statistics CR and VR regions.

Parameter	CR		VR	
	Value	Error	Value	Error
N_{bkg}	5.3097E+04	3.35E+02	5.3064E+04	3.33E+02
p2	1.7800E+01	7.92E-01	1.7244E+01	9.73E-01
p3	1.3883E+01	3.90E-01	1.3234E+01	4.40E-01
p4	7.3108E+01	1.07E-01	7.9501E+01	1.17E-01
p5	1.1808E+00	3.19E-02	1.4061E+00	3.48E-02

Figure 8.12: Post-fit parameters for the PFN CR and VR.

1705 SR is obtained. This process is referred to as *downsampling*. Examples of three downsampled histograms are provided for each region in Figure 8.13. TODO: recalculate VR see if it's still bad

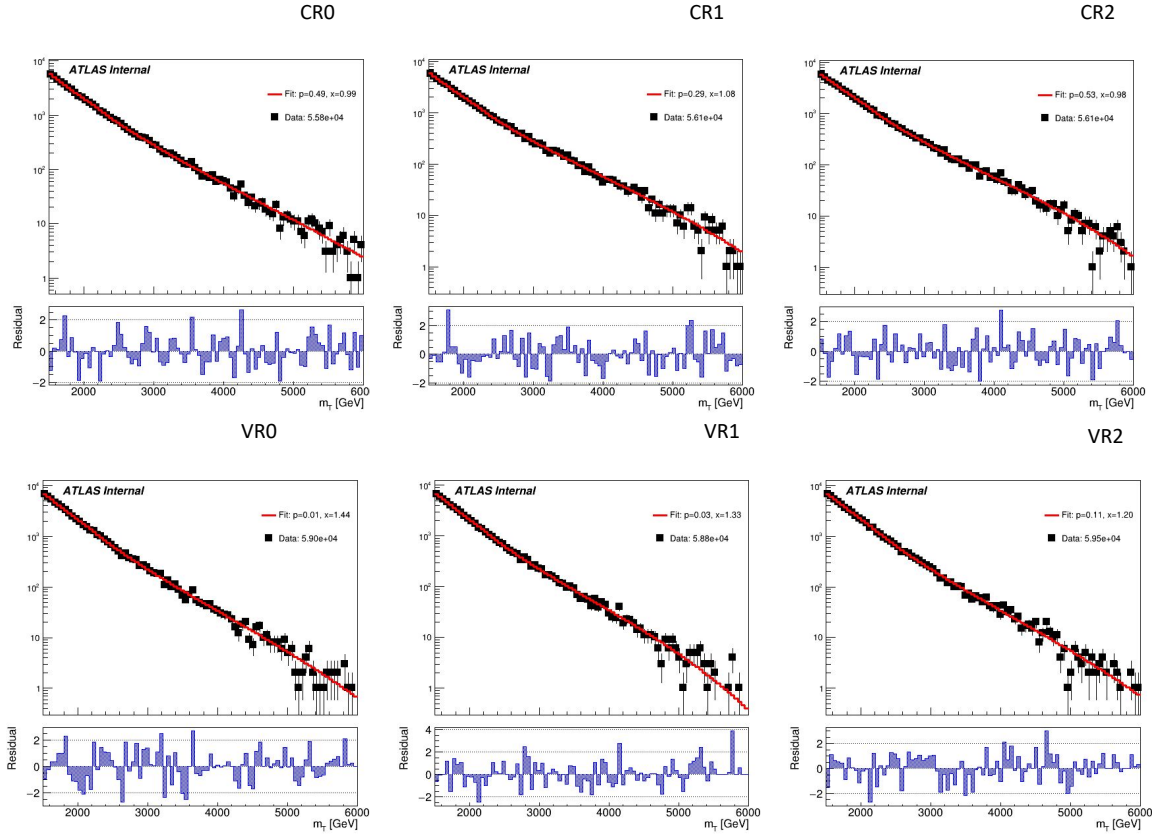


Figure 8.13: Background-only m_T fits using data in orthogonal but statistically identical samples to the SR, obtained by downsampling the CR/VR statistics, for the CR (top) and VR (bottom).

1706

1707 To further validate the fit stability of the fit against potential statistical fluctuations, *pseudo-data*
 1708 (also known as *toy datasets*) are created from the CR data distribution. The pseudo-data is created
 1709 following an *Asimov* prescription [77], using a template to generate a set of toys representing differ-
 1710 ent possible statistical fluctuations. When studied as a group, the performance of the pseudo-data
 1711 collection represents the range of possible behavior for an unknown distribution (the SR data in
 1712 this case), given its statistical uncertainties. The template used to generate the pseudo-data is a
 1713 smoothed version of the CR. The smoothing applied follows the procedure for functional decom-
 1714 position described in Ref. [edgar2018functional]. Figure 8.14 shows the impact of smoothing on
 1715 the source data distribution in the CR. Toys are then generated from the smoothed distribution, by
 1716 varying each bin within its statistical uncertainty according to a Poisson distribution.

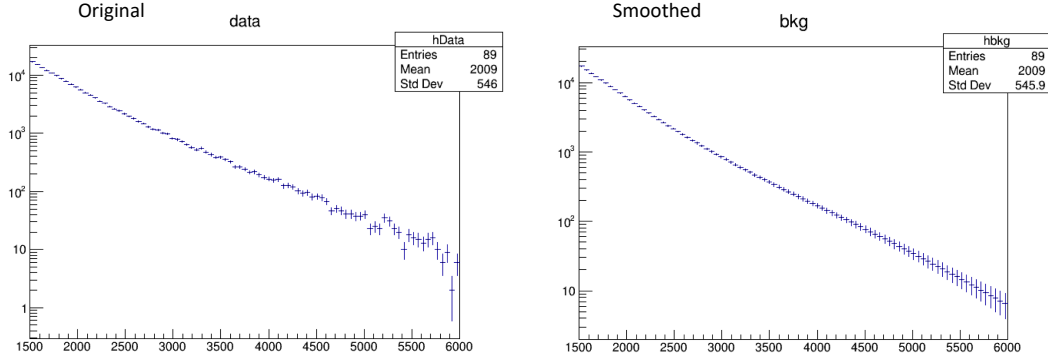


Figure 8.14: m_T distribution in the data CR, before (left) and after (right) smoothing.

1717 Figure 8.15 shows the resulting p-values after an ensemble of 100 Asimov pseudo-data are each
 1718 individually fit. This test determines the likelihood of exceptionally good (high p-value) or poor
 1719 (fit due to random statistical fluctuations in the data. A flat distribution is observed,
 indicating good statistical behavior.

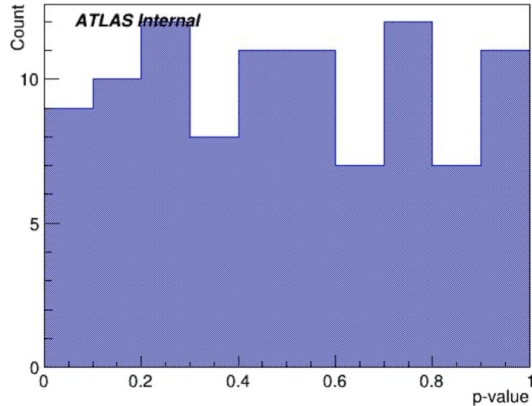


Figure 8.15: p -value histograms from 100 fits to Asimov data in the CR.

1720

1721 Signal + Background Fits

1722 Figure 8.16 shows some examples of S+B fits on the background-only distribution for a variety
 1723 of signal hypotheses across the (R_{inv} , mass) grid.

1724 **Spurious Signal** The spurious signal fits are done using S+B fits on signal-depleted regions.
 1725 These fits performed in pseudodata derived from a smoothed CR template are used to calculate the

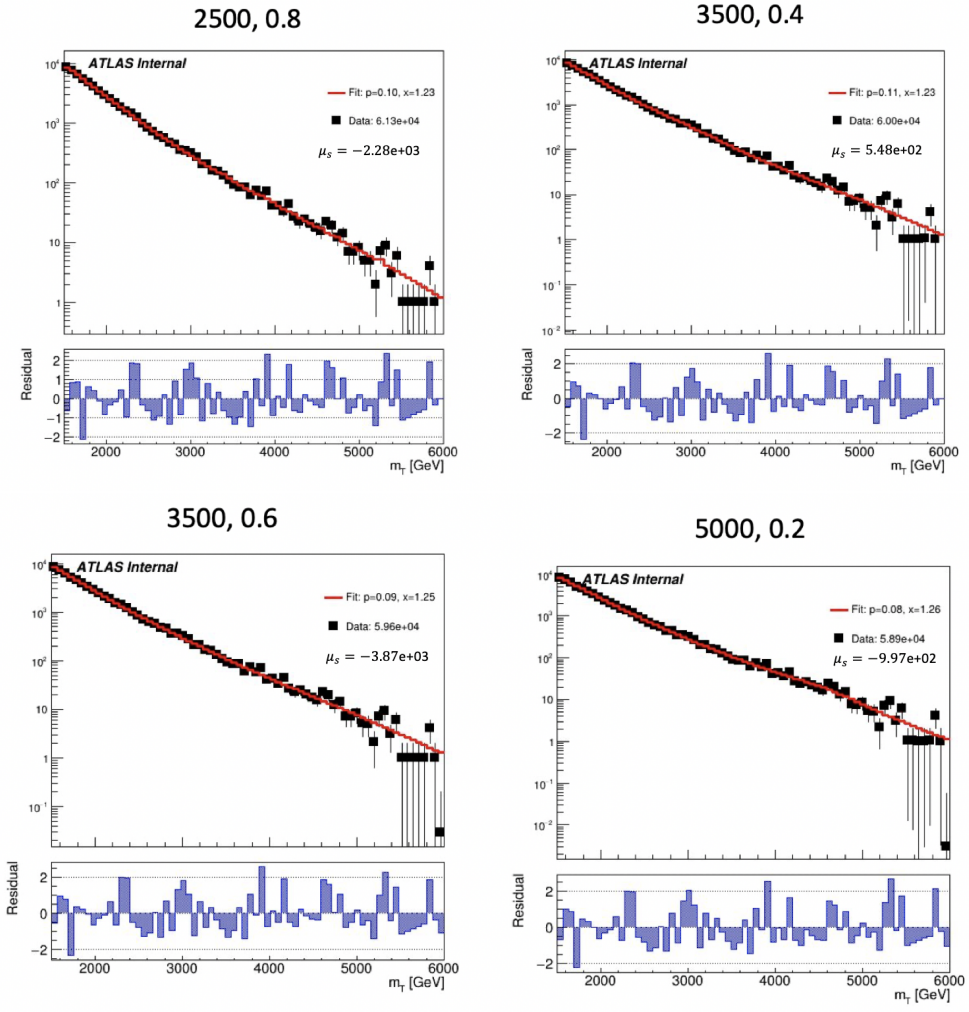


Figure 8.16: Example S+B fits on background only spectrum (without systematics) for a variety of signal points.

¹⁷²⁶ spurious signal uncertainty, as described in Section ??.

1727 **Signal Injection in CR Template** Figure 8.17 shows an example of an injected signal into the
 1728 exclusion region m_T spectrum, and the ability of the fit framework to accurately fit the number of
 signal events.

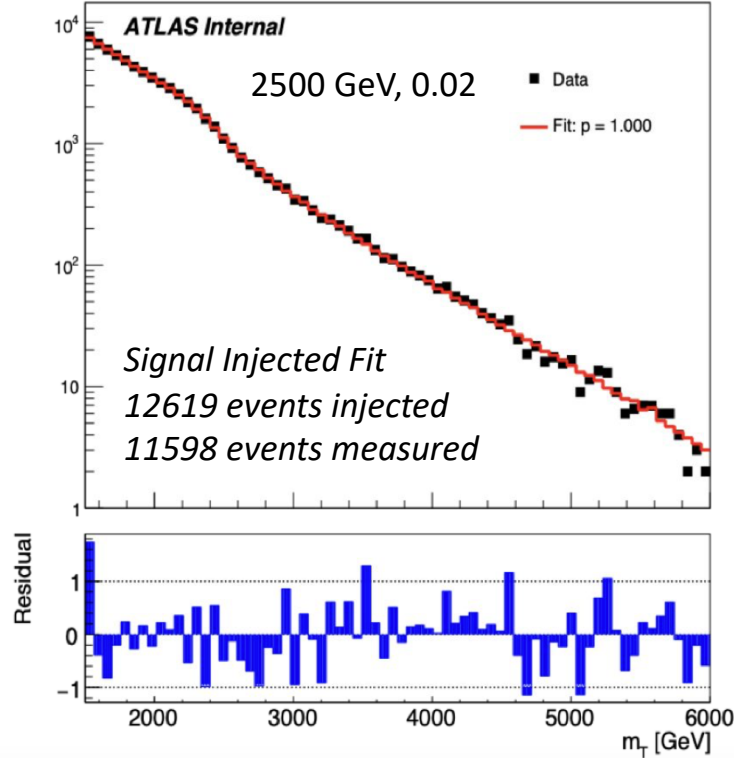


Figure 8.17: Example S+B fits on a background m_T spectrum with injected signal from the point (2500 GeV, $R_{inv}=0.2$).

1729
 1730 Figure 8.18 shows the linearity of the fitted signal as a function of the size of the injected signal,
 1731 for all 4 R_{inv} categories and several Z' masses. No uncertainties on the signal model are included.
 1732 These fits are done in a single template of the CR, making the fitted signal prone to fluctuations in
 1733 the underlying template, motivating the use of toys to better capture the behavior of the S+B fit in
 1734 finding a signal.

1735 **Signal Injection in Asimov Data** To better understand the correlations of fit errors in the above
 1736 single-template injection test and avoid drawing conclusions from a single scenario, signal in-
 1737 jection tests using Asimov data will be performed before unblinding. Criteria for this check are

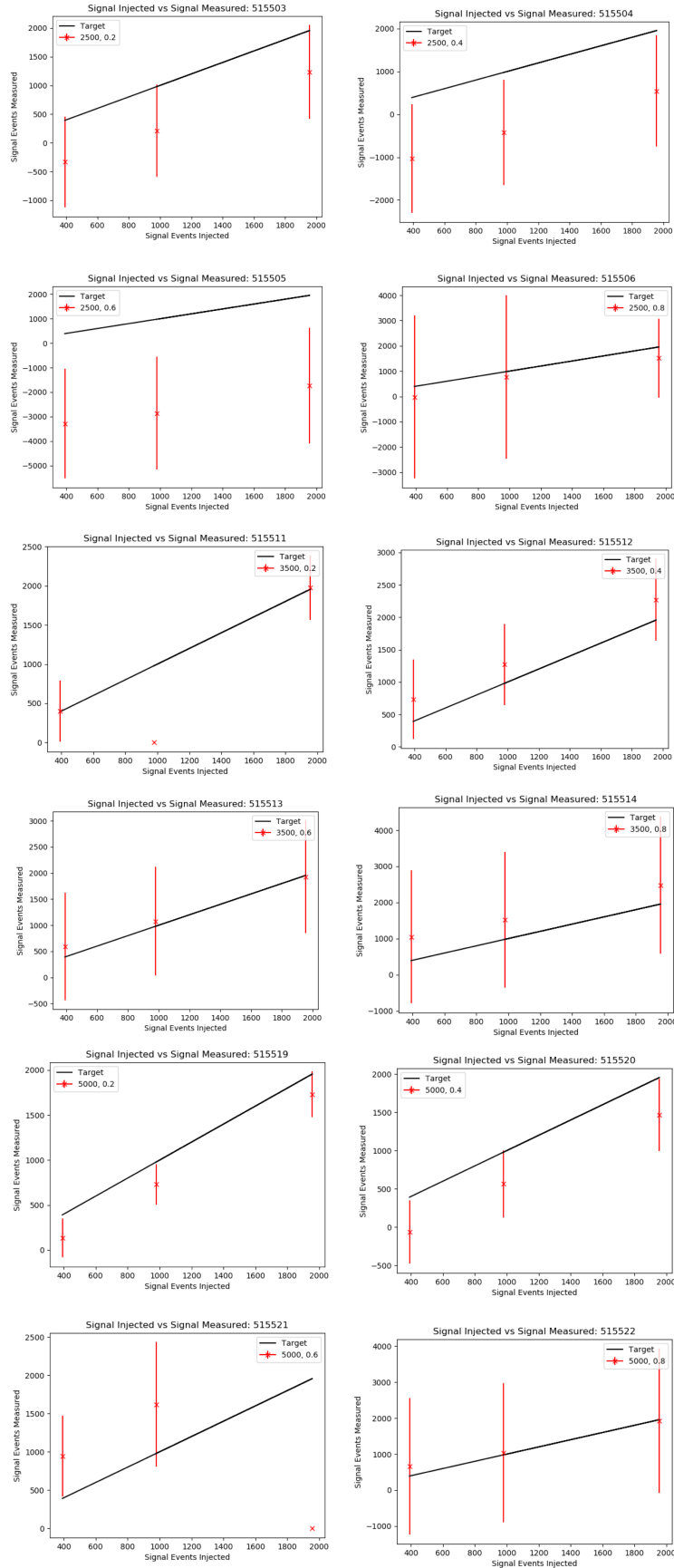


Figure 8.18: Linearity of fitted vs. injected signal across m_T , for signal points with $R_{inv}=0.2, 0.4, 0.6$, and 0.8 , with several Z' masses (2500 GeV, 3500 GeV, and 5000 GeV top to bottom) for a single CR template with no systematics.

adapted from the Run 2 dijet TLA analysis ¹. 50 Asimov trials are run for representative signal points across Z' mass and R_{inv} . Specifically, we will take the difference between fitted and injected signal events as a spurious signal and require it to be less than 10% of the original injected signal yield, or its absolute value to be less than 50% of the fitted signal RMS:

$$S_{\text{spur}} = S_{\text{fit}} - S_{\text{inj}} < 0.1S_{\text{inj}} \text{ OR } < 0.5\sigma_{\text{fit}} \quad (8.3)$$

Figure 8.19 provides tabular results of these tests, assessing both S_{spur} from Equation 8.3. Figure 8.20 displays the measured $S_{\text{spur}}/\sigma_{\text{fit}}$ for each signal point to assess the criterion from Equation 8.3. We find that all but 1 of the tested signal points and signal injection sizes ($m_{Z'} = 4000$ GeV, $R_{inv}=0.2$ at 5σ significance) pass the criteria in Equation 8.3. While ($m_{Z'} = 4000$ GeV, $R_{inv}=0.2$) generally gives the highest S_{spur} of all points, the one injected size that violates the test criterion is close to 0.5 and within a trend shared by all points.

¹<https://cds.cern.ch/record/2632454>, Section 10.4

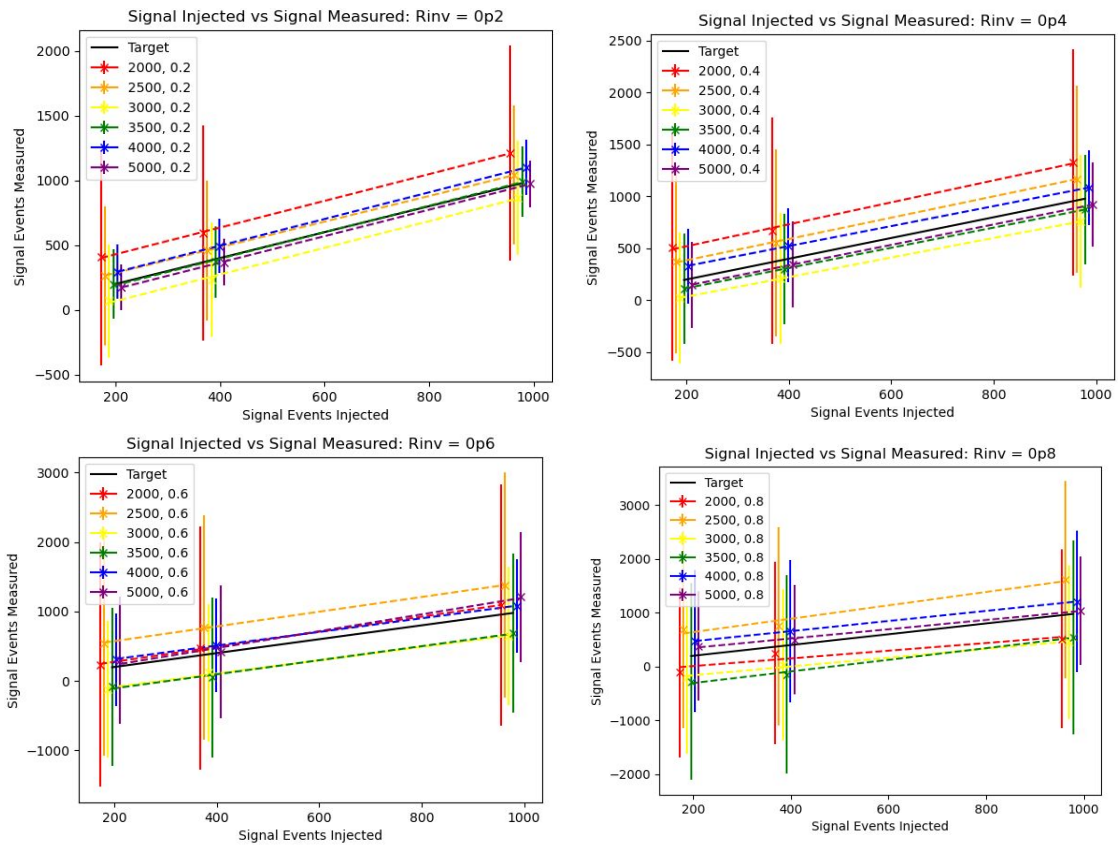


Figure 8.19: Spurious signal at a variety of injected values (1, 2, and 5σ significant), for all signal points in the grid, $R_{inv}=0.2$ (top left), 0.4 (top right), 0.6 (bottom left), and 0.8 (bottom right). i

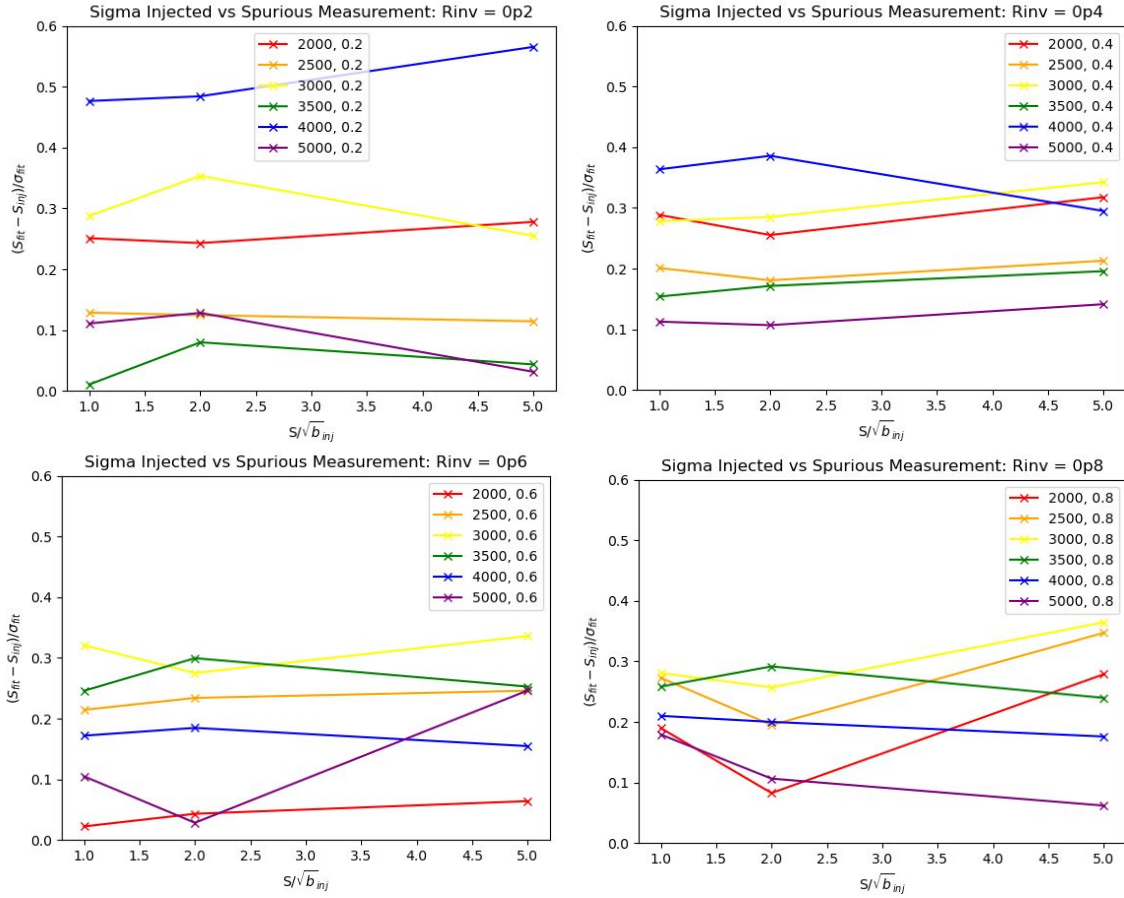


Figure 8.20: S_{spur}/σ_{fit} at a variety of injected values (1, 2, and 5 σ significant), for all signal points in the grid, $R_{inv}=0.2$ (top left), 0.4 (top right), 0.6 (bottom left), and 0.8 (bottom right). i

1748 **Expected Sensitivity**

1749 Limits are obtained by determining the cross section of the signal that can be excluded to 95%
1750 confidence. Figure 8.21 shows the expected limits obtained from S+B fits to statistically identical
1751 m_T spectra from the CR region (which is closest in m_T shape to the SR according to MC studies).

1752 Considerable exclusion power is predicted for low R_{inv} signal points, with the higher R_{inv} points
1753 presenting more difficulty due to the very broad signal bump. A similar trend is observed in the
1754 CMS s-channel search [**cms_schan**].

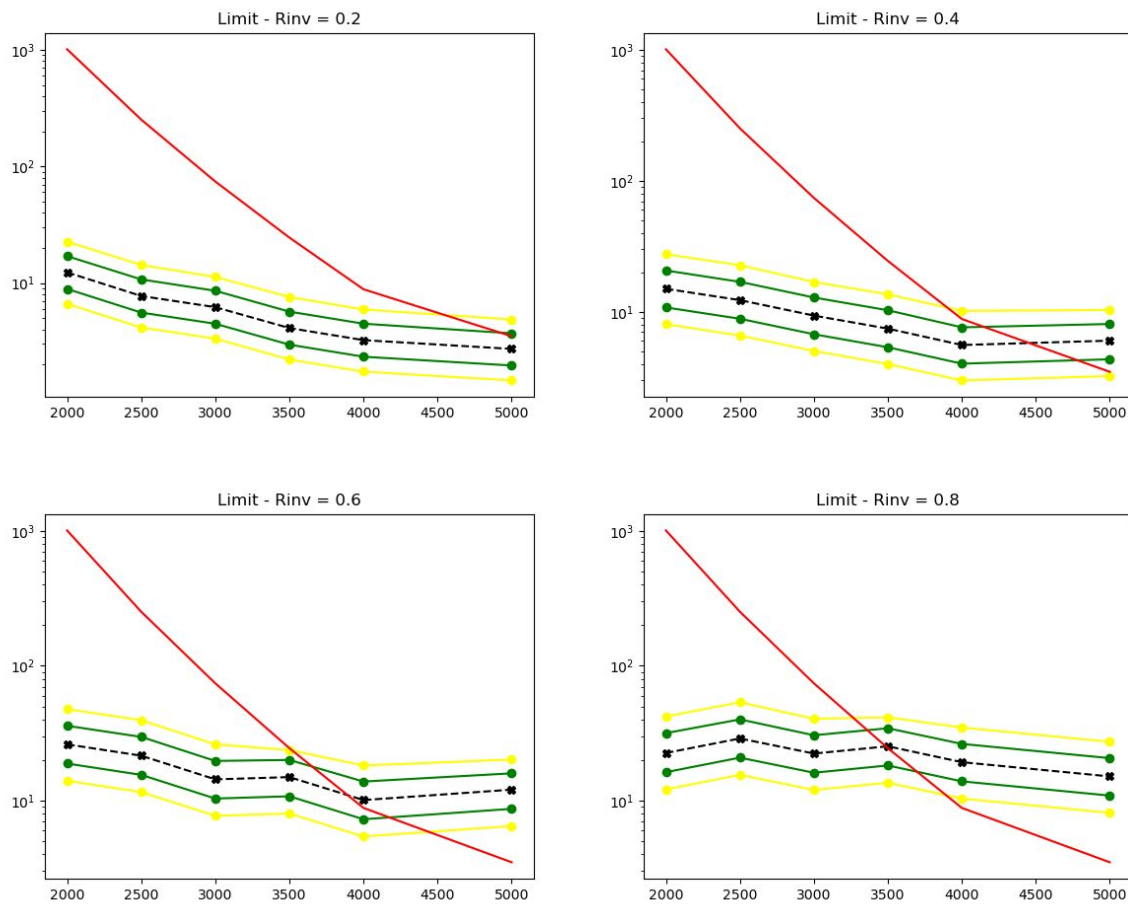


Figure 8.21: 95% C.L. upper limits for signal models across Z' mass, for four different R_{inv} fractions, from the CR region (without systematics).

1755 A 2D limit presentation is also being considered, in the (R_{inv} , mass) plane.

1756 8.5.2 Discovery Strategy)

1757 Model-independent fits for the discovery region will be performed using pyBumpHunter. The
1758 strategy will consist of comparing the data in a given m_T spectrum of interest to a background
1759 estimation derived by performing the polynomial fit and sampling from the post-fit function into
1760 a histogram. The polynomial fit is done to an m_T distribution with 180 bins (25 GeV wide). To
1761 keep the trials factor moderate, a rebinning will be performed based on the signal mass resolution in
1762 m_T (Section 8.5.2) to best assess the significance of BumpHunter results. This is under development
1763 with preliminary studies shown in Appendix ??.

1764 Figure 8.22 shows the post-fit values of the fit parameters and their uncertainties for the discov-
1765 ery (ANTELOPE-based) CR and VR. Figure 8.23 shows the resulting functions and residuals with
1766 respect to the CR and VR data. These results indicate good ability of the 5-parameter polynomial
to also model the ANTELOPE selected region.

Parameter	CR		VR	
	Value	Error	Value	Error
N_{bkg}	8.8299E+04	4.27E+02	8.8312E+04	4.27E+02
p2	3.6804E+01	3.97E+00	3.8490E+01	4.29E+00
p3	4.2925E+01	5.06E+00	4.3432E+01	4.81E+00
p4	1.9080E+01	1.95E+00	1.9626E+01	1.78E+00
p5	2.9298E+00	2.86E-01	3.0527E+00	2.62E-01

Figure 8.22: Post-fit parameters for the ANTELOPE CR and VR.

1767

1768 **Signal Mass Resolution m_T Binning**

1769 In the discovery region, a binning for m_T is determined that is based on the expected signal
1770 width. This is done to improved the BumpHunter performance. The signal mass resolution for a
1771 given point is determined with a double-sided Crystal Ball fit to the mass. These fits are performed
1772 across Z' mass, and a linear fit to these values is performed to determine the optimal bin width

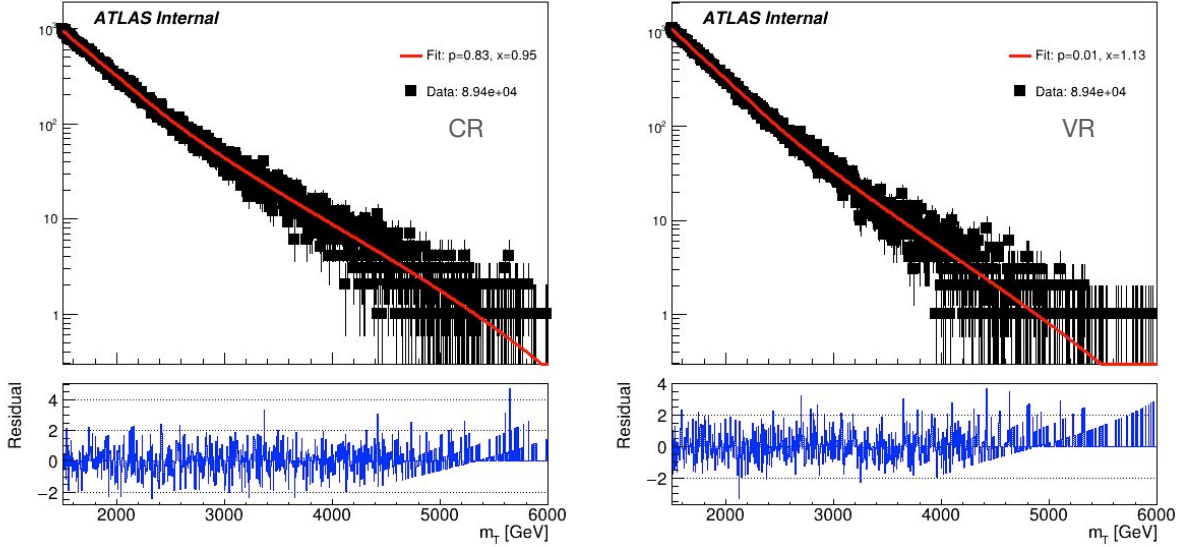


Figure 8.23: Post-fit function and residuals for the ANTELOPE CR and VR.

1773 across m_T .

1774 The x-axis value used is a data-driven way to determine the appropriate value of m_T for a
 1775 given signal, given that the considerable E_T^{miss} from the dark particles means that the truth Z'
 1776 mass does not well approximate the peak m_T value. As the E_T^{miss} in the final state means that the
 1777 m_T is always an underestimate of the Z' mass, the truth Z' mass can be used as an upper bound. An
 1778 integral is then performed backwards from that value until 60% of the total signal yield is included.
 1779 This window is referred to as the 60% mass window; the mean of this window then provides an
 1780 approximate localization of the signal mass peak in m_T . Figure 8.24 shows some examples of this
 1781 algorithm on several signal points of varying R_{inv} and mass.

1782 Figure 8.25 shows the result of this linear fit for the four R_{inv} values considered in the signal
 1783 grid. As expected, the resolution is considerably different for low and high R_{inv} points.

1784 A single m_T binning for the final SR plotting and BumpHunting is determined by selecting a
 1785 harmonized binning at low m_T , and moving to wider bins at high m_T . As for higher R_{inv} signal
 1786 points the mass resolution linear fit gives negative results, we require each bin to have a width of
 1787 at least 100 GeV. Figure 8.26 shows the resulting bins for each R_{inv} category that comes from the
 1788 mass resolution fits, with the addition of the minimum 100 GeV bin width requirement.

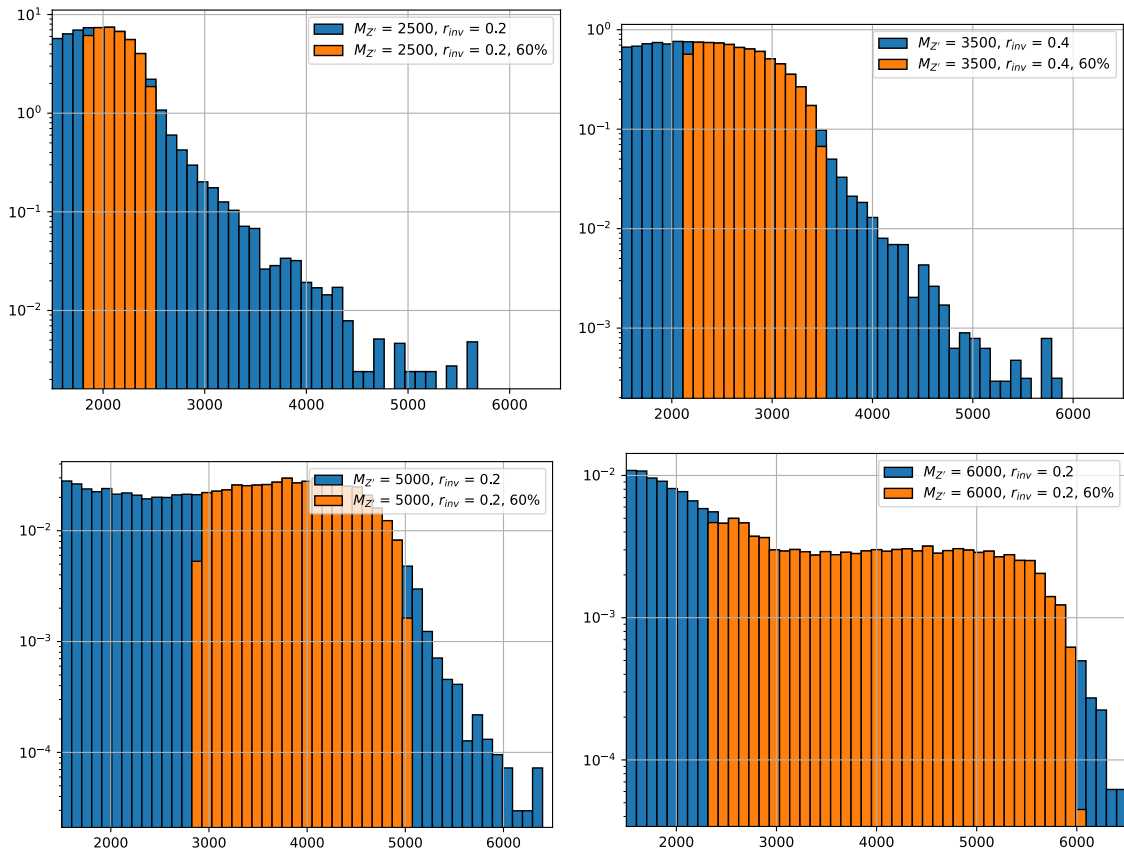


Figure 8.24: Example determinations of the 60% mass window means for several signal points.

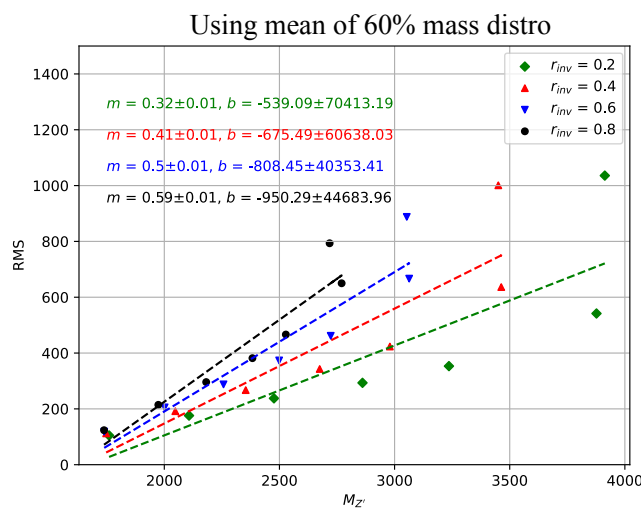


Figure 8.25: Signal mass resolution for m_T binning for the signal grid in (R_{inv}, mass) space.

$r_{inv} = 0.2 \rightarrow$	[1500, 1600, 1700, 1800, 1904, 2029, 2177, 2356, 2569, 2824, 3128, 3493, 3929, 4451, 5075, 5822, 6715]
$r_{inv} = 0.4 \rightarrow$	[1500, 1600, 1700, 1800, 1910, 2053, 2238, 2477, 2787, 3187, 3704, 4374, 5240, 6361]
$r_{inv} = 0.6 \rightarrow$	[1500, 1600, 1700, 1800, 1919, 2087, 2321, 2650, 3110, 3755, 4659, 5925, 7698]
$r_{inv} = 0.8 \rightarrow$	[1500, 1600, 1700, 1800, 1927, 2117, 2400, 2823, 3455, 4400, 5811, 7918]

Figure 8.26: m_T bins based on the signal mass resolution and the minimum 100 GeV width requirement, for each R_{inv} signal category.

1789 In order to have a final m_T binning that is not highly model-dependent, we consolidate these

1790 four different bins into a single binning which is provided below:

1791 [1500, 1600, 1700, 1800, 1900, 2025, 2175, 2350, 2575, 2825, 3125, 3500, 3925, 4450, 5075,
1792 6000]

1793 BumpHunter Fits

1794 Figure 8.27 shows the result of running BumpHunter over the CR and VR m_T spectra, binned
1795 according to the signal mass resolution binning described above. The background estimation here
1796 is derived by fitting the ANTELOPE regions with the polynomial fit function, and sampling from
1797 this function to create a binned histogram. We define a spurious signal as any BumpHunter fit find-
1798 ing an excess with p-value < 0.01 (taken from other dijet analysis eg. Ref. [ATLAS:2023azi]). No
1799 spurious signal is observed, and p-values indicate good agreement with the background estimation.

1800

1801 Figure 8.28 shows BumpHunter p-values over 100 Asimov trials. The same fit success criteria
1802 as the PFN region is applied: p-value > 0.001 and fit status succeeding (0 or 1). In both cases, no
1803 spurious signals are found (p-value < 0.01).

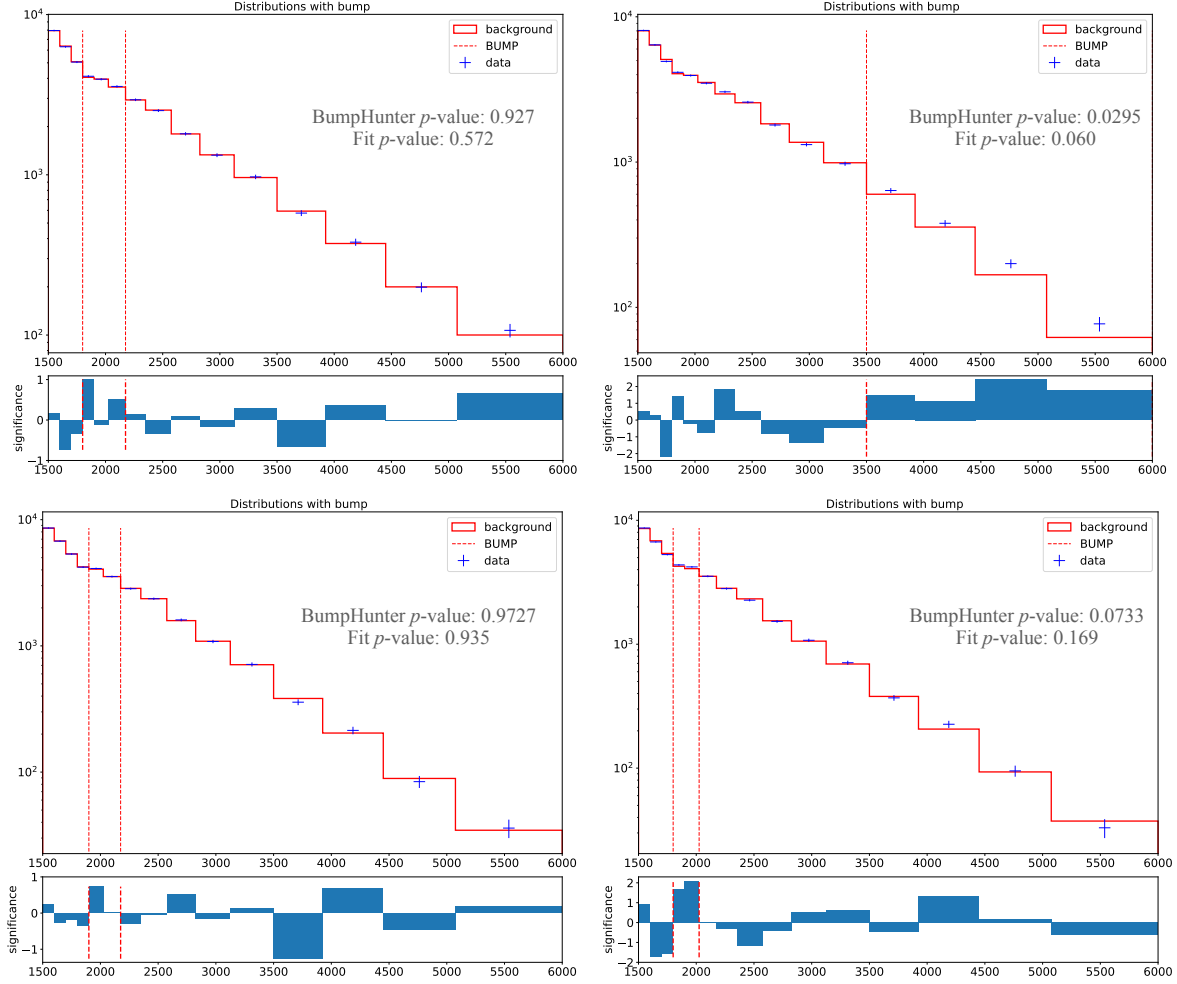


Figure 8.27: BumpHunter fits on the ANTELOPE m_T spectra for both the CR and VR. In a signal-depleted region, good agreement with the background estimation is observed.

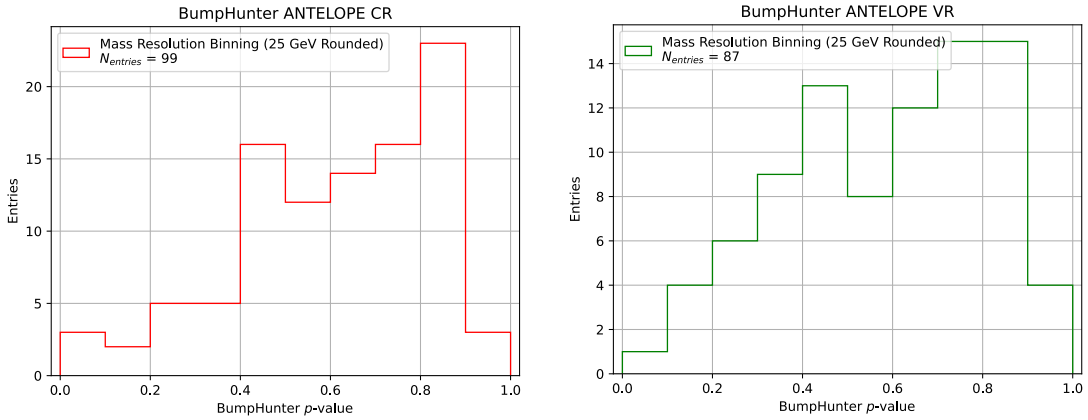


Figure 8.28: BumpHunter p-values extracted for 100 Asimov toys for both the ANTELOPE CR (top) and VR (bottom) showing the highest (left) and lowest (right) p-value fits. The number of events in the histogram deviates from 100 based on failed background-only fits.

1804

1805

Chapter 9: Results

1806

Conclusion or Epilogue

1807 Use this page for your epilogue or conclusion if applicable; please use only one of the titles
1808 for this page. Otherwise, you may delete it. Use this page for your epilogue or conclusion if
1809 applicable; please use only one of the titles for this page. Otherwise, you may delete it. Use this
1810 page for your epilogue or conclusion if applicable; please use only one of the titles for this page.
1811 Otherwise, you may delete it. Use this page for your epilogue or conclusion if applicable; please
1812 use only one of the titles for this page. Otherwise, you may delete it. Use this page for your
1813 epilogue or conclusion if applicable; please use only one of the titles for this page. Otherwise,
1814 you may delete it. Use this page for your epilogue or conclusion if applicable; please use only one
1815 of the titles for this page. Otherwise, you may delete it. Use this page for your epilogue or
1816 conclusion if applicable; please use only one of the titles for this page. Otherwise, you may delete
1817 it. Use this page for your epilogue or conclusion if applicable; please use only one of the titles for
1818 this page. Otherwise, you may delete it. Use this page for your epilogue or conclusion if
1819 applicable; please use only one of the titles for this page. Otherwise, you may delete it. Use this
1820 page for your epilogue or conclusion if applicable; please use only one of the titles for this page.
1821 Otherwise, you may delete it. Use this page for your epilogue or conclusion if applicable; please
1822 use only one of the titles for this page. Otherwise, you may delete it. Use this page for your
1823 epilogue or conclusion if applicable; please use only one of the titles for this page. Otherwise,
1824 you may delete it. Use this page for your epilogue or conclusion if applicable; please use only one
1825 of the titles for this page. Otherwise, you may delete it. Use this page for your epilogue or
1826 conclusion if applicable; please use only one of the titles for this page. Otherwise, you may delete

1827 it. Use this page for your epilogue or conclusion if applicable; please use only one of the titles for
1828 this page. Otherwise, you may delete it. Use this page for your epilogue or conclusion if
1829 applicable; please use only one of the titles for this page. Otherwise, you may delete it. Use this
1830 page for your epilogue or conclusion if applicable; please use only one of the titles for this page.
1831 Otherwise, you may delete it. Use this page for your epilogue or conclusion if applicable; please
1832 use only one of the titles for this page. Otherwise, you may delete it. Use this page for your
1833 epilogue or conclusion if applicable; please use only one of the titles for this page. Otherwise,
1834 you may delete it. Use this page for your epilogue or conclusion if applicable; please use only one
1835 of the titles for this page. Otherwise, you may delete it. Use this page for your epilogue or
1836 conclusion if applicable; please use only one of the titles for this page. Otherwise, you may delete
1837 it. Use this page for your epilogue or conclusion if applicable; please use only one of the titles for
1838 this page. Otherwise, you may delete it. Use this page for your epilogue or conclusion if
1839 applicable; please use only one of the titles for this page. Otherwise, you may delete it. Use this
1840 page for your epilogue or conclusion if applicable; please use only one of the titles for this page.
1841 Otherwise, you may delete it. Use this page for your epilogue or conclusion if applicable; please
1842 use only one of the titles for this page. Otherwise, you may delete it. Use this page for your
1843 epilogue or conclusion if applicable; please use only one of the titles for this page. Otherwise,
1844 you may delete it. Use this page for your epilogue or conclusion if applicable; please use only one
1845 of the titles for this page. Otherwise, you may delete it. Use this page for your epilogue or
1846 conclusion if applicable; please use only one of the titles for this page. Otherwise, you may delete
1847 it. Use this page for your epilogue or conclusion if applicable; please use only one of the titles for
1848 this page. Otherwise, you may delete it. Use this page for your epilogue or conclusion if
1849 applicable; please use only one of the titles for this page. Otherwise, you may delete it. Use this
1850 page for your epilogue or conclusion if applicable; please use only one of the titles for this page.
1851 Otherwise, you may delete it. Use this page for your epilogue or conclusion if applicable; please
1852 use only one of the titles for this page. Otherwise, you may delete it. Use this page for your
1853 epilogue or conclusion if applicable; please use only one of the titles for this page. Otherwise,

1854 you may delete it. Use this page for your epilogue or conclusion if applicable; please use only one
1855 of the titles for this page. Otherwise, you may delete it. Use this page for your epilogue or
1856 conclusion if applicable; please use only one of the titles for this page. Otherwise, you may delete
1857 it. Use this page for your epilogue or conclusion if applicable; please use only one of the titles for
1858 this page. Otherwise, you may delete it. Use this page for your epilogue or conclusion if
1859 applicable; please use only one of the titles for this page. Otherwise, you may delete it. Use this
1860 page for your epilogue or conclusion if applicable; please use only one of the titles for this page.
1861 Otherwise, you may delete it. Use this page for your epilogue or conclusion if applicable; please
1862 use only one of the titles for this page. Otherwise, you may delete it. Use this page for your
1863 epilogue or conclusion if applicable; please use only one of the titles for this page. Otherwise,
1864 you may delete it. Use this page for your epilogue or conclusion if applicable; please use only one
1865 of the titles for this page. Otherwise, you may delete it. Use this page for your epilogue or
1866 conclusion if applicable; please use only one of the titles for this page. Otherwise, you may delete
1867 it. Use this page for your epilogue or conclusion if applicable; please use only one of the titles for
1868 this page. Otherwise, you may delete it. Use this page for your epilogue or conclusion if
1869 applicable; please use only one of the titles for this page. Otherwise, you may delete it. Use this
1870 page for your epilogue or conclusion if applicable; please use only one of the titles for this page.
1871 Otherwise, you may delete it. Use this page for your epilogue or conclusion if applicable; please
1872 use only one of the titles for this page. Otherwise, you may delete it. Use this page for your
1873 epilogue or conclusion if applicable; please use only one of the titles for this page. Otherwise,
1874 you may delete it. Use this page for your epilogue or conclusion if applicable; please use only one
1875 of the titles for this page. Otherwise, you may delete it. Use this page for your epilogue or
1876 conclusion if applicable; please use only one of the titles for this page. Otherwise, you may delete
1877 it. Use this page for your epilogue or conclusion if applicable; please use only one of the titles for
1878 this page. Otherwise, you may delete it. Use this page for your epilogue or conclusion if
1879 applicable; please use only one of the titles for this page. Otherwise, you may delete it. Use this
1880 page for your epilogue or conclusion if applicable; please use only one of the titles for this page.

1881 Otherwise, you may delete it. Use this page for your epilogue or conclusion if applicable; please
1882 use only one of the titles for this page. Otherwise, you may delete it. Use this page for your
1883 epilogue or conclusion if applicable; please use only one of the titles for this page. Otherwise,
1884 you may delete it. Use this page for your epilogue or conclusion if applicable; please use only one
1885 of the titles for this page. Otherwise, you may delete it. Use this page for your epilogue or
1886 conclusion if applicable; please use only one of the titles for this page. Otherwise, you may delete
1887 it. Use this page for your epilogue or conclusion if applicable; please use only one of the titles for
1888 this page. Otherwise, you may delete it. Use this page for your epilogue or conclusion if
1889 applicable; please use only one of the titles for this page. Otherwise, you may delete it. Use this
1890 page for your epilogue or conclusion if applicable; please use only one of the titles for this page.
1891 Otherwise, you may delete it. Use this page for your epilogue or conclusion if applicable; please
1892 use only one of the titles for this page. Otherwise, you may delete it. Use this page for your
1893 epilogue or conclusion if applicable; please use only one of the titles for this page. Otherwise,
1894 you may delete it. Use this page for your epilogue or conclusion if applicable; please use only one
1895 of the titles for this page. Otherwise, you may delete it. Use this page for your epilogue or
1896 conclusion if applicable; please use only one of the titles for this page. Otherwise, you may delete
1897 it. Use this page for your epilogue or conclusion if applicable; please use only one of the titles for
1898 this page. Otherwise, you may delete it. Use this page for your epilogue or conclusion if
1899 applicable; please use only one of the titles for this page. Otherwise, you may delete it. Use this
1900 page for your epilogue or conclusion if applicable; please use only one of the titles for this page.
1901 Otherwise, you may delete it. Use this page for your epilogue or conclusion if applicable; please
1902 use only one of the titles for this page. Otherwise, you may delete it. Use this page for your
1903 epilogue or conclusion if applicable; please use only one of the titles for this page. Otherwise,
1904 you may delete it. Use this page for your epilogue or conclusion if applicable; please use only one
1905 of the titles for this page. Otherwise, you may delete it. Use this page for your epilogue or
1906 conclusion if applicable; please use only one of the titles for this page. Otherwise, you may delete
1907 it.

References

- [1] Jens Erler and Paul Langacker. “Electroweak model and constraints on new physics”. In: (July 2004). arXiv: hep-ph/0407097.
- [2] David J Griffiths. *Introduction to elementary particles; 2nd rev. version*. Physics textbook. New York, NY: Wiley, 2008.
- [3] M. Tanabashi et al. “Review of Particle Physics”. In: *Phys. Rev. D* 98 (3 2018), pp. 847–851.
- [4] E. Noether. “Invariante Variationsprobleme”. In: *Nachr. d. König. Gesellsch. d. Wiss. zu Göttingen, Math-phys. Klasse*, Seite 235–157 (1918). eprint: www.physics.ucla.edu/\~\cwp/articles/noether.trans/german/emmy235.html.
- [5] J. H. Christenson et al. “Evidence for the 2π Decay of the K_2^0 Meson”. In: *Phys. Rev. Lett.* 13 (1964), pp. 138–140.
- [6] Michael Gronau. “CP Violation in B Meson Decays”. In: *Nuclear Physics B - Proceedings Supplements* 142 (May 2005), 263–270.
- [7] J. E. Augustin et al. “Discovery of a Narrow Resonance in e^+e^- Annihilation”. In: *Phys. Rev. Lett.* 33 (1974), pp. 1406–1408.
- [8] J. J. Aubert et al. “Experimental Observation of a Heavy Particle J ”. In: *Phys. Rev. Lett.* 33 (1974), pp. 1404–1406.
- [9] Martin L. Perl et al. “Evidence for Anomalous Lepton Production in $e^+ - e^-$ Annihilation”. In: *Phys. Rev. Lett.* 35 (1975), pp. 1489–1492.
- [10] S. W. Herb et al. “Observation of a Dimuon Resonance at 9.5-GeV in 400-GeV Proton-Nucleus Collisions”. In: *Phys. Rev. Lett.* 39 (1977), pp. 252–255.
- [11] F. Abe et al. “Observation of top quark production in $\bar{p}p$ collisions”. In: *Phys. Rev. Lett.* 74 (1995), pp. 2626–2631. arXiv: hep-ex/9503002.
- [12] S. Abachi et al. “Observation of the top quark”. In: *Phys. Rev. Lett.* 74 (1995), pp. 2632–2637. arXiv: hep-ex/9503003.
- [13] K. Kodama et al. “Observation of tau neutrino interactions”. In: *Phys. Lett. B* 504 (2001), pp. 218–224. arXiv: hep-ex/0012035.

- 1935 [14] G. Arnison et al. “Experimental Observation of Lepton Pairs of Invariant Mass Around 95-
 1936 GeV/c**2 at the CERN SPS Collider”. In: *Phys. Lett. B* 126 (1983), pp. 398–410.
- 1937 [15] P. Bagnaia et al. “Evidence for $Z^0 \rightarrow e^+e^-$ at the CERN $\bar{p}p$ Collider”. In: *Phys. Lett. B* 129
 1938 (1983), pp. 130–140.
- 1939 [16] Serguei Chatrchyan et al. “Observation of a New Boson at a Mass of 125 GeV with the
 1940 CMS Experiment at the LHC”. In: *Phys. Lett. B* 716 (2012), pp. 30–61. arXiv: 1207.7235
 1941 [hep-ex].
- 1942 [17] Georges Aad et al. “Observation of a new particle in the search for the Standard Model
 1943 Higgs boson with the ATLAS detector at the LHC”. In: *Phys. Lett. B* 716 (2012), pp. 1–29.
 1944 arXiv: 1207.7214 [hep-ex].
- 1945 [18] K. G. Begeman, A. H. Broeils, and R. H. Sanders. “Extended rotation curves of spiral galax-
 1946 ies: Dark haloes and modified dynamics”. In: *Mon. Not. Roy. Astron. Soc.* 249 (1991), p. 523.
- 1947 [19] Y. Ashie et al. “Evidence for an oscillatory signature in atmospheric neutrino oscillation”.
 1948 In: *Phys. Rev. Lett.* 93 (2004), p. 101801. arXiv: hep-ex/0404034.
- 1949 [20] C. Abel et al. “Measurement of the Permanent Electric Dipole Moment of the Neutron”. In:
 1950 *Phys. Rev. Lett.* 124.8 (2020), p. 081803. arXiv: 2001.11966 [hep-ex].
- 1951 [21] Guillaume Albouy et al. “Theory, phenomenology, and experimental avenues for dark show-
 1952 ers: a Snowmass 2021 report”. In: *The European Physical Journal C* 82.12 (Dec. 2022).
- 1953 [22] Timothy Cohen et al. “LHC searches for dark sector showers”. In: *Journal of High Energy
 1954 Physics* 2017.11 (Nov. 2017).
- 1955 [23] Lyndon Evans and Philip Bryant. “LHC Machine”. In: *Journal of Instrumentation* 3.08
 1956 (2008), S08001.
- 1957 [24] “The ATLAS Experiment at the CERN Large Hadron Collider”. In: *JINST* 3 (2008). Also
 1958 published by CERN Geneva in 2010, S08003.
- 1959 [25] “The CMS experiment at the CERN LHC”. In: *Journal of Instrumentation* 3.08 (2008),
 1960 S08004.
- 1961 [26] “The ALICE experiment at the CERN LHC”. In: *Journal of Instrumentation* 3.08 (2008),
 1962 S08002.
- 1963 [27] “The LHCb Detector at the LHC”. In: *Journal of Instrumentation* 3.08 (2008), S08005.
- 1964 [28] Ana Lopes and Melissa Loyse Perrey. *FAQ-LHC The guide*. 2022.

- 1965 [29] Esma Mobs. “The CERN accelerator complex in 2019. Complexe des accélérateurs du
1966 CERN en 2019”. In: (2019). General Photo.
- 1967 [30] *Pulling together: Super Conducting electromagnets*. <https://home.cern/science/engineering/pulling-together-superconducting-electromagnets>.
1968 Accessed: 2024-01-05.
- 1970 [31] *The High-Luminosity LHC*. <https://voisins.web.cern.ch/en/high-luminosity-lhc-hl-lhc>. Accessed: 2024-01-05.
- 1972 [32] Aad G., et al. (ATLAS Collaboration and CMS Collaboration). “Combined Measurement of
1973 the Higgs Boson Mass in pp Collisions at $\sqrt{s} = 7$ and 8 TeV with the ATLAS and CMS
1974 Experiments”. In: *Phys. Rev. Lett.* 114 (19 2015), p. 191803.
- 1975 [33] O. Aberle et al. *High-Luminosity Large Hadron Collider (HL-LHC): Technical design re-*
1976 *port*. CERN Yellow Reports: Monographs. Geneva: CERN, 2020.
- 1977 [34] The ATLAS Collaboration. “The ATLAS Experiment at the CERN Large Hadron Collider”.
1978 In: *Journal of Instrumentation* 3.08 (2008), S08003.
- 1979 [35] G Aad, B Abbott, and ATLAS Collaboration. “Performance of the reconstruction of large
1980 impact parameter tracks in the inner detector of ATLAS”. In: *Eur. Phys. J. C Part. Fields*
1981 83.11 (Nov. 2023).
- 1982 [36] Joao Pequenao. *Computer Generated image of the ATLAS calorimeter*. 2008.
- 1983 [37] *ATLAS liquid-argon calorimeter: Technical Design Report*. Technical design report. AT-
1984 LAS. Geneva: CERN, 1996.
- 1985 [38] H A Gordon. “Liquid argon calorimetry for the SSC”. In: () .
- 1986 [39] Henric Wilkens and (on behalf of the ATLAS LArg Collaboration). “The ATLAS Liquid
1987 Argon calorimeter: An overview”. In: *Journal of Physics: Conference Series* 160.1 (2009),
1988 p. 012043.
- 1989 [40] *Technical Design Report for the Phase-II Upgrade of the ATLAS Tile Calorimeter*. Tech.
1990 rep. Geneva: CERN, 2017.
- 1991 [41] “Technical Design Report for the Phase-II Upgrade of the ATLAS Muon Spectrometer”. In:
1992 () .
- 1993 [42] L Pontecorvo. “The ATLAS Muon Spectrometer”. In: (2004). revised version number 1
1994 submitted on 2003-07-27 16:31:16.

- 1995 [43] *ATLAS magnet system: Technical Design Report, 1*. Technical design report. ATLAS. Geneva:
1996 CERN, 1997.
- 1997 [44] Joao Pequenao. “Event Cross Section in a computer generated image of the ATLAS detector.” 2008.
1998
- 1999 [45] ATLAS Collaboration. “ATLAS Experiment Implements Heterogeneous Particle Recon-
2000 struction with Intel oneAPI Tools”. General Photo. 2023.
- 2001 [46] ATLAS Collaboration. “Electron and photon performance measurements with the ATLAS
2002 detector using the 2015–2017 LHC proton-proton collision data”. In: *Journal of Instrumen-*
2003 *tation* 14.12 (2019), P12006.
- 2004 [47] Chiara Deponte. “Studies on the properties of non-prompt photons at the ATLAS experi-
2005 ment”. Presented 16 Aug 2022. Technische Universitaet Dortmund (DE), 2022.
- [48] ATLAS Collaboration. “Muon reconstruction performance of the ATLAS detector in pro-
ton–proton collision data at \sqrt{s}
2006 $s = 13 \text{ TeV}$ ”. In: *The European Physical Journal C* 76.5 (2016).
- 2007 [49] Sebastien Rettie. *Muon identification and performance in the ATLAS experiment*. Tech. rep.
2008 Geneva: CERN, 2018.
- 2009 [50] B. R. Webber. *Fragmentation and Hadronization*. 1999. arXiv: hep-ph/9912292 [hep-ph].
- 2010 [51] Eric M. Metodiev. *The Fractal Lives of Jets* | Eric M. Metodiev — ericmetodiev.com. https://
2011 //www.ericmetodiev.com/post/jetformation/. 2019, note = [Accessed 18-
2012 05-2024],
- 2013 [52] Matteo Cacciari, Gavin P Salam, and Gregory Soyez. “The anti-ktjet clustering algorithm”.
2014 In: *Journal of High Energy Physics* 2008.04 (Apr. 2008), 063–063.
- 2015 [53] Matteo Cacciari, Gavin P. Salam, and Gregory Soyez. “FastJet user manual: (for version
2016 3.0.2)”. In: *The European Physical Journal C* 72.3 (Mar. 2012).
- 2017 [54] Steven Schramm. *ATLAS Jet Reconstruction, Calibration, and Tagging of Lorentz-boosted
2018 Objects*. Tech. rep. Geneva: CERN, 2017.
- 2019 [55] ATLAS Collaboration. “Topological cell clustering in the ATLAS calorimeters and its per-
2020 formance in LHC Run 1”. In: *The European Physical Journal C* 77.7 (July 2017).
- 2021 [56] ATLAS Collaboration. “Jet reconstruction and performance using particle flow with the
2022 ATLAS Detector”. In: *The European Physical Journal C* 77.7 (July 2017).

- 2023 [57] Stephen D. Ellis and Davison E. Soper. “Successive combination jet algorithm for hadron
2024 collisions”. In: *Physical Review D* 48.7 (Oct. 1993), 3160–3166.
- 2025 [58] M. Wobisch and T. Wengler. *Hadronization Corrections to Jet Cross Sections in Deep-*
2026 *Inelastic Scattering*. 1999. arXiv: hep-ph/9907280 [hep-ph].
- 2027 [59] Gavin P Salam and Gr  gory Soyez. “A practical seedless infrared-safe cone jet algorithm”.
2028 In: *Journal of High Energy Physics* 2007.05 (May 2007), 086–086.
- 2029 [60] Gavin P. Salam. “Towards jetography”. In: *The European Physical Journal C* 67.3–4 (May
2030 2010), 637–686.
- 2031 [61] *A Monte Carlo study of track association to jets for b-tagging*. Tech. rep. Geneva: CERN,
2032 2021.
- 2033 [62] *Flavor Tagging with Track Jets in Boosted Topologies with the ATLAS Detector*. Tech. rep.
2034 All figures including auxiliary figures are available at <https://atlas.web.cern.ch/Atlas/GROUPS/PHYSICS/P>
2035 PHYS-PUB-2014-013. Geneva: CERN, 2014.
- 2036 [63] ATLAS Collaboration. “Performance of missing transverse momentum reconstruction with
2037 the ATLAS detector using proton-proton collisions at $\sqrt{s} = 13$ TeV”. In: *Eur. Phys. J. C*
2038 78.11 (2018), p. 903. arXiv: 1802.08168.
- 2039 [64] GEANT4 Collaboration, S. Agostinelli, et al. “GEANT4 – a simulation toolkit”. In: *Nucl.*
2040 *Instrum. Meth. A* 506 (2003), p. 250.
- 2041 [65] Christian Bierlich et al. *A comprehensive guide to the physics and usage of PYTHIA 8.3*.
2042 2022. arXiv: 2203.11601 [hep-ph].
- 2043 [66] J. Alwall et al. “The automated computation of tree-level and next-to-leading order differ-
2044 ential cross sections, and their matching to parton shower simulations”. In: *JHEP* 07 (2014),
2045 p. 079. arXiv: 1405.0301 [hep-ph].
- 2046 [67] Jon Butterworth et al. “PDF4LHC recommendations for LHC Run II”. In: *J. Phys. G* 43
2047 (2016), p. 023001. arXiv: 1510.03865 [hep-ph].
- 2048 [68] Peter Skands, Stefano Carrazza, and Juan Rojo. “Tuning PYTHIA 8.1: the Monash 2013
2049 Tune”. In: *Eur. Phys. J. C* 74.8 (2014), p. 3024. arXiv: 1404.5630 [hep-ph].
- 2050 [69] Patrick T. Komiske, Eric M. Metodiev, and Jesse Thaler. “Energy flow networks: deep sets
2051 for particle jets”. In: *Journal of High Energy Physics* 2019.1 (2019).
- 2052 [70] A. Kahn et al. “Anomalous jet identification via sequence modeling”. In: *Journal of Instru-*
2053 *mentation* 16.08 (Aug. 2021), P08012.

- 2054 [71] Georges Aad et al. “Anomaly detection search for new resonances decaying into a Higgs
2055 boson and a generic new particle X in hadronic final states using $\sqrt{s} = 13$ TeV pp collisions
2056 with the ATLAS detector”. In: *Phys. Rev. D* 108 (2023), p. 052009. arXiv: 2306.03637
2057 [[hep-ex](#)].
- 2058 [72] Georgios Choudalakis. *On hypothesis testing, trials factor, hypertests and the BumpHunter*.
2059 2011. arXiv: 1101.0390.
- 2060 [73] Peter Loch. “Jet measurements in ATLAS”. In: *J. Phys. Conf. Ser.* 323 (2011). Ed. by Gior-
2061 gio Bellettini, p. 012002.
- 2062 [74] The ATLAS Collaboration. “Search for diboson resonances in hadronic final states in 139
2063 fb-1 of pp collisions at $\sqrt{s} = 13$ TeV with the ATLAS detector”. In: *Journal of High Energy*
2064 *Physics* 2019.9 (Sept. 2019).
- 2065 [75] *Recommendations for the Modeling of Smooth Backgrounds*. Tech. rep. Geneva: CERN,
2066 2020.
- 2067 [76] The CMS Collaboration. “Search for resonant production of strongly coupled dark matter
2068 in proton-proton collisions at 13 TeV”. In: *Journal of High Energy Physics* 2022.6 (June
2069 2022).
- 2070 [77] Glen Cowan et al. “Asymptotic formulae for likelihood-based tests of new physics”. In: *The*
2071 *European Physical Journal C* 71.2 (Feb. 2011).

Appendix A: Trigger Studies

2074 Both the lowest unprescaled E_T^{miss} and single small-R jet triggers were considered for this
 2075 analysis. The E_T^{miss} trigger is observed to have higher efficiency for low mass, high R_{inv} points,
 2076 while the single small-R trigger favors high mass, low R_{inv} points. Figure A.1 shows the yields
 2077 and signal efficiencies across the grid for both these strategies.

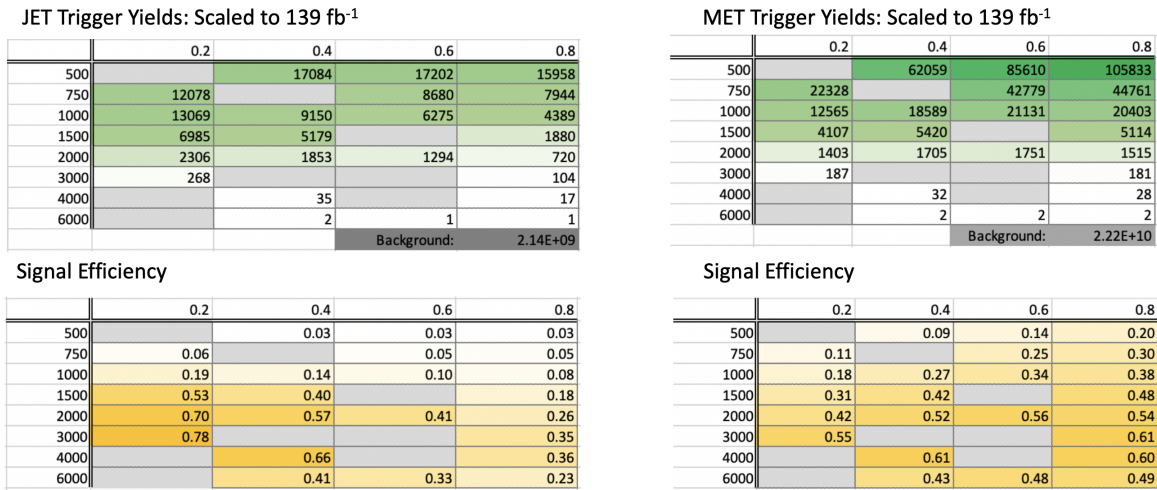


Figure A.1: Trigger yield and efficiency for both the MET trigger and small-R jet trigger approach. Each entry represent a signal point, labelled by the Z' mass and the R_{inv} fraction.

2078 The cross section is higher for the lower Z' mass signal points. As a result, our sensitivity
 2079 to these points and ability to set limits on them is already naturally enhanced. Figure A.2 shows
 2080 the factor of improvement in the inclusive S/\sqrt{B} using each trigger strategy. A cross-check was
 2081 also done calculating S/\sqrt{B} in windows around the mT mass. The results of this cross-check
 2082 confirmed the results shown in Figure A.2.

2083 Figure A.3 shows the ratio of S/\sqrt{B} across the signal grid for the jet trigger compared to the
 2084 E_T^{miss} trigger.

2085 This plot makes clear that the E_T^{miss} trigger favors the low mass, high R_{inv} signal points, while

$(\text{JET Trigger } S/\sqrt{B}) / (\text{Untriggered } S/\sqrt{B})$				
	0.2	0.4	0.6	0.8
500		1.26	1.43	1.53
750	2.99		2.52	2.68
1000	9.24	6.74	5.03	4.07
1500	26.45	20.15		8.83
2000	34.66	28.24	20.57	12.85
3000	39.05			17.35
4000		32.94		17.96
6000		20.57	16.55	11.53

$(\text{MET Trigger } S/\sqrt{B}) / (\text{Untriggered } S/\sqrt{B})$				
	0.2	0.4	0.6	0.8
500		1.43	2.21	3.15
750	1.72		3.86	4.69
1000	2.76	4.26	5.26	5.89
1500	4.83	6.56		7.47
2000	6.55	8.08	8.65	8.40
3000	8.46			9.38
4000		9.51		9.32
6000		6.68	7.43	7.59

Figure A.2: The factor of improvement in S/\sqrt{B} for each trigger method compared to the untriggered case.

	0.2	0.4	0.6	0.8
500		0.89	0.65	0.49
750	1.74		0.65	0.57
1000	3.35	1.58	0.96	0.69
1500	5.47	3.07		1.18
2000	5.29	3.49	2.38	1.53
3000	4.62			1.85
4000		3.46		1.93
6000		3.08	2.23	1.52

Figure A.3: The ratio of S/\sqrt{B} of jet trigger over E_T^{miss} trigger selection.

2086 the single jet trigger favors the high mass, low R_{inv} signal points. A number of considerations led
2087 us to selecting the single jet trigger. First, Figure A.2 illustrates that the sensitivity enhancement is
2088 greater for signals favored by the jet trigger than signals favored by the E_T^{miss} trigger. This indicates
2089 we have more to gain from focusing on the region of our signal grid where the jet trigger is most
2090 efficient. We combined this with the observation that the jet trigger is beneficial for high mass
2091 points where the cross-section is lower and we need to maximize sensitivity to hope to set limits
2092 on these points.

2093 Second, there are a number of analysis variables at our disposal which are more discriminant for
2094 high R_{inv} signals than for low R_{inv} signals. A collection of these variables are shown in Figure A.4.
2095 Given that we had multiple avenues available to enhance sensitivity to low R_{inv} signals through
2096 analysis strategy cuts, we opted for a trigger strategy that benefitted the low R_{inv} signal points.
2097 Additionally, we know E_T^{miss} is highly correlated with these discriminant analysis variables, and a
2098 E_T^{miss} trigger would reduce the effectiveness of these variables. Not implementing the E_T^{miss} trigger
2099 allows us to explore other ways of leveraging E_T^{miss} in the analysis using a cut that is more finely
2100 tuned to the specifics of the signal model than the E_T^{miss} trigger is.

2101 Third, we know that fitting the high R_{inv} mass points would be challenging given their very
2102 broad shapes in the key analysis variable m_T . Given the analysis decision to do a search for
2103 resonant features in m_T , we chose to design a search that emphasized maximizing sensitivity
2104 to the signal points that we were mostly to appear as a resonant feature in m_T . The shape of
2105 m_T and our reduced ability to set limits on high R_{inv} points is demonstrated in the body of this
2106 note. Another search strategy may be more optimal for setting limits on high R_{inv} semi-visible jet
2107 signals, but it is currently outside the scope of this analysis.

2108 A jet or E_T^{miss} trigger was also considered, but abandoned due to concerns about sculpting
2109 features in the smoothly falling E_T^{miss} or leading jet p_T distributions, as shown in Figure A.5.

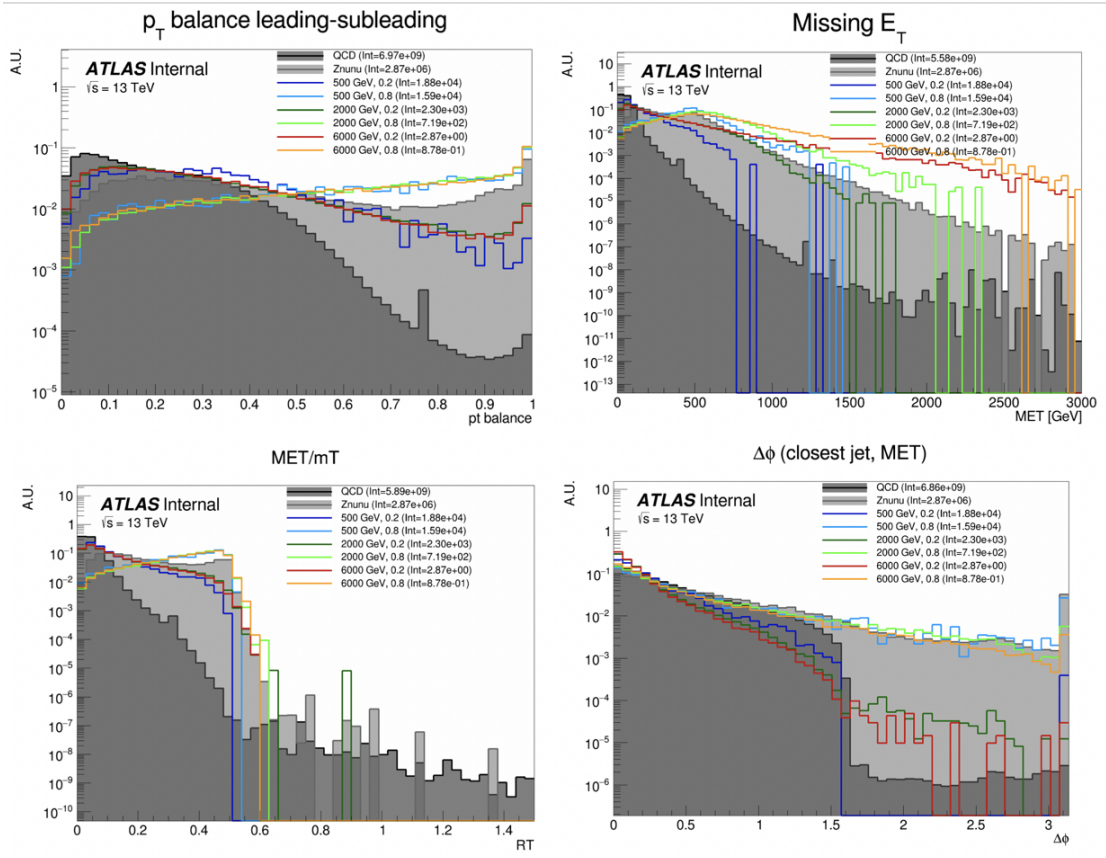


Figure A.4: Analysis variables where high R_{inv} signals a clearly distinct from background and low R_{inv} variables. On the contrary, leading jet p_T is one of the only variables where low R_{inv} signals are distinct from background.

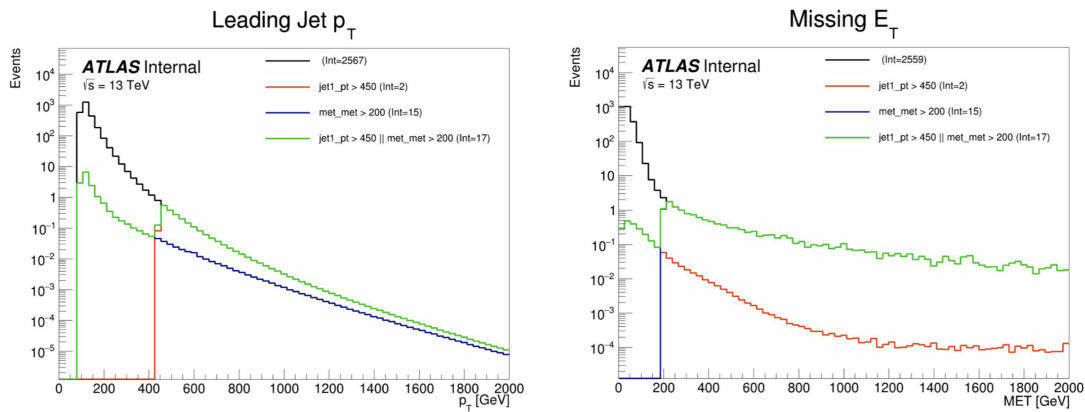


Figure A.5: OR of jet and E_T^{miss} triggers.

2110

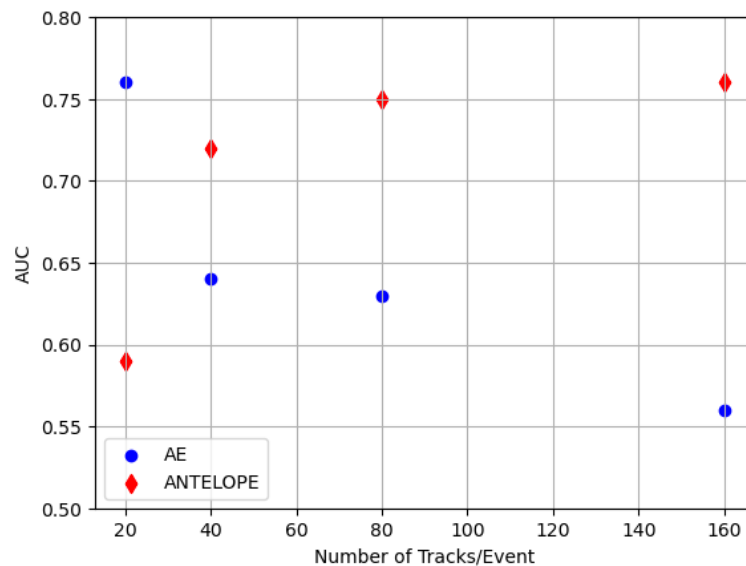
2111

Appendix B: Machine Learning Approaches

2112 B.1 Unsupervised: AE vs. ANTELOPE

2113 To understand the benefits of the semi-supervised ANTELOPE approach, we study the AN-
 2114 TELope in comparison to a traditional anomaly detection architecture like an autoencoder. The
 2115 autoencoder cannot accommodate variable length or permutation invariant inputs.

2116 Figure B.1 shows the AUC determined by each of these two tools as a function of number
 2117 of tracks. The trend is that the AE suffers when more information is given, due to the presence
 2118 of 0-padding. In contrast, the ANTELOPE architecture performs better with more information,
 motivating the use of high dimensional input modelin with this method.



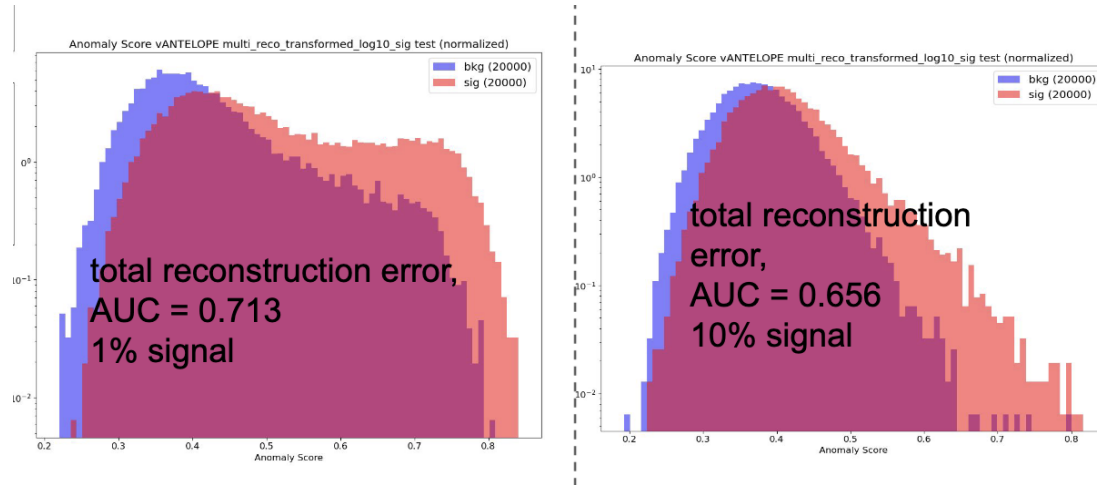
- Confirms that AE is negatively sensitive to zero padding while ANTELOPE sees a performance improvement as it sees more “information”

Figure B.1

2119

2120 **Signal Contamination**

2121 To understand the effect of signal contamination in training on the ANTELOPE score, we inject
2122 a percent of signal events into the data used to train the ANTELOPE autoencoder stage and look
2123 at the AUC on signals. Figure B.2 shows no variation in AUC with 1% contamination in training
data, but a few % drop going up to 10%.



2124 Figure B.2

2125 **B.2 PFN Optimality Checks**

2126 The PFN is trained using QCD as the background. A study was done to compare the perfor-
2127 mance of the tool in the analysis context if it trains against QCD or a representative MC background
2128 considering the small fractions of other processes ($V+jets$, top) that would contribute at preselec-
2129 tion. Figure B.3 shows the AUC across the grid for both training approaches, revealing better
2130 performance if the tool focuses on learning QCD differences.

2131 Further studies were done to ensure the relatively optimality of the single PFN model, trained
2132 over combined signals, across the grid. As the grid spans signals with a large range of E_T^{miss} , their
2133 varying input features and background composition may be conducive to separate PFN models
2134 trained on high and low E_T^{miss} signal points to better capture the signal-background differences.
2135 Figure B.4 shows a comparison of the signal-inclusive PFN model performance and the perfor-

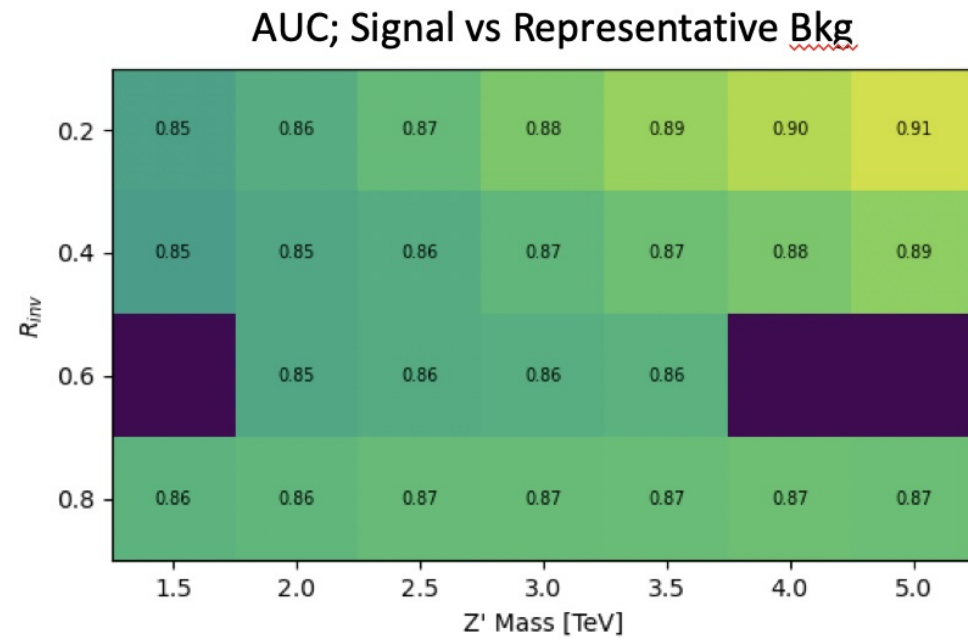
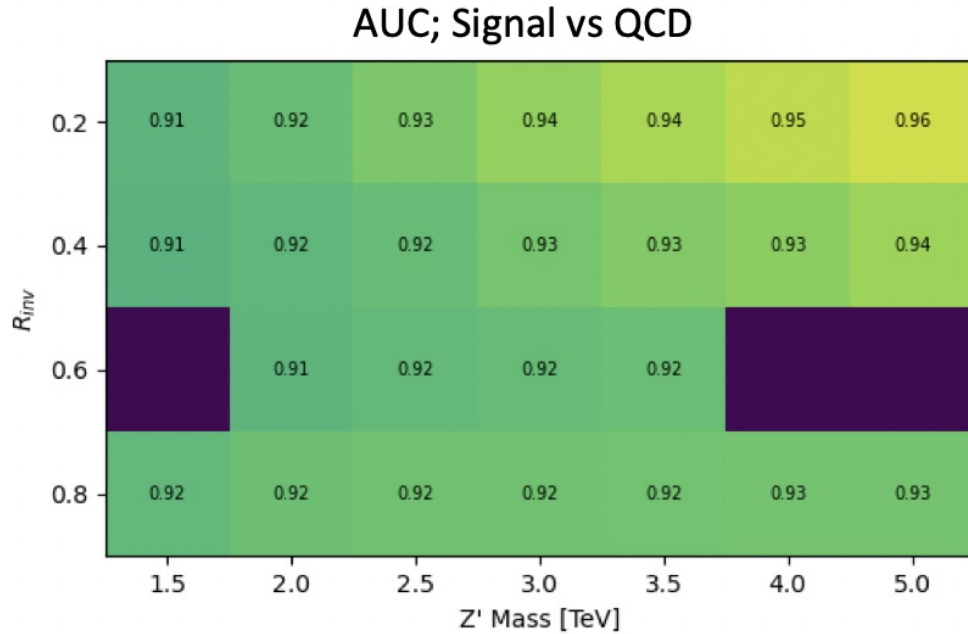


Figure B.3: AUC from the PFN score for each signal in the SVJ grid, shown versus the QCD-only training sample (top) and the total MC background (bottom). Note the three missing points will be added shortly - they were delayed due to a DAOD production mistake.

2136 mance of models separated into high and low R_{inv} signals in training. The most notable impact is
 2137 found for the low R_{inv} and high mass points, indicating that the signal-inclusive PFN is learning
 2138 morning about the distinction between high- E_T^{miss} signals and backgrounds. However, these high
 2139 mass points are also the most challenging to find due to their very wide resonance on top of m_T ,
 2140 and in the final projected sensitivity in the m_T window the differences are $< 10\%$ across the grid.
 2141 To maintain a harmonized strategy with the ANTELOPE region we keep the inclusive PFN model
 2142 as the final version.

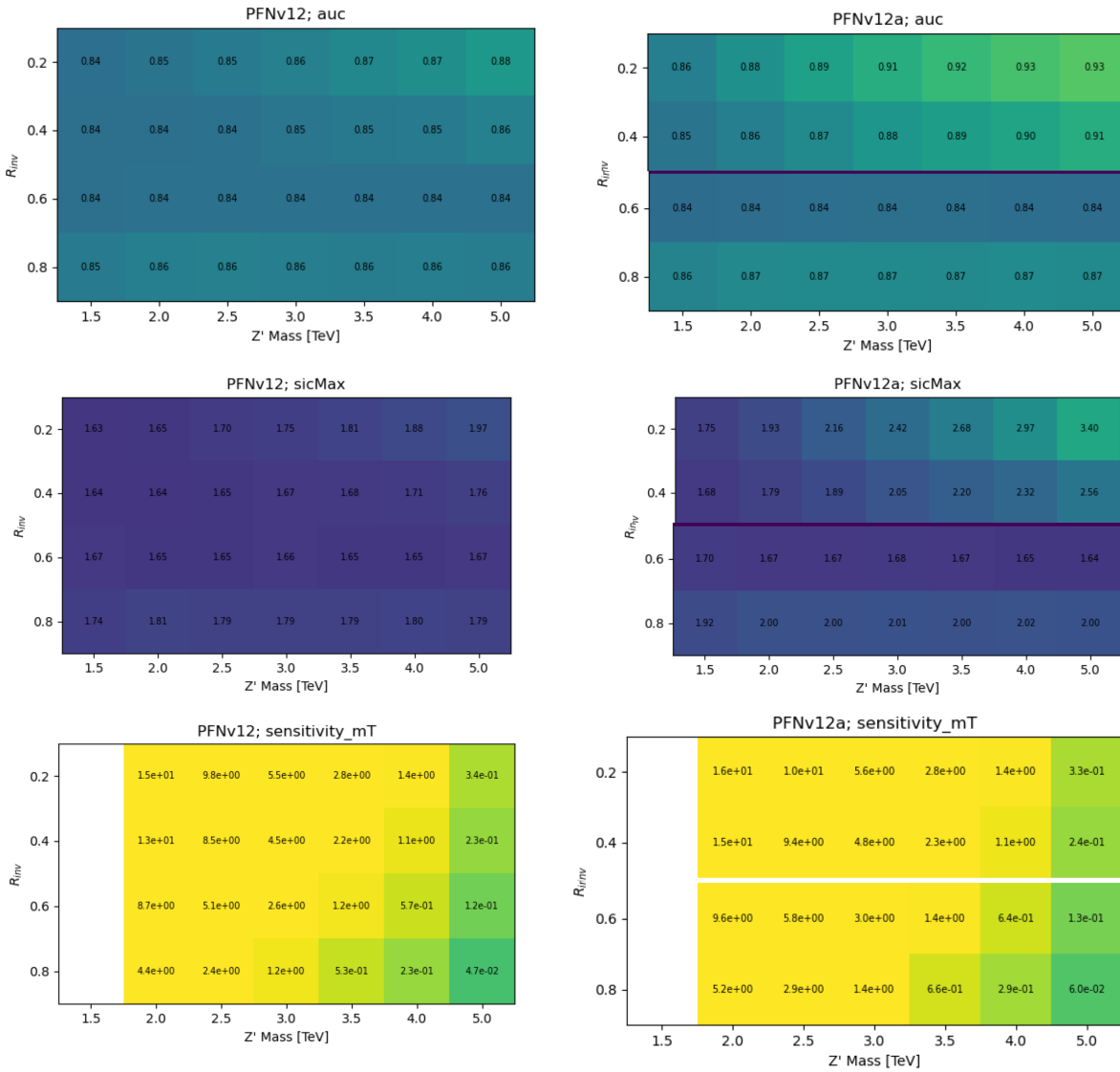


Figure B.4: Comparison of PFN AUC (top), SIC (middle), and sensitivity in the m_T mass window (bottom) for a single PFN model (left) vs. two models, trained on $R_{inv} < 0.5$ and > 0.5 separately.

2143 Figure B.5 shows the optimal cut on the PFN score for each point in the signal grid, motivating
the loose inclusive choice used to define the SR.

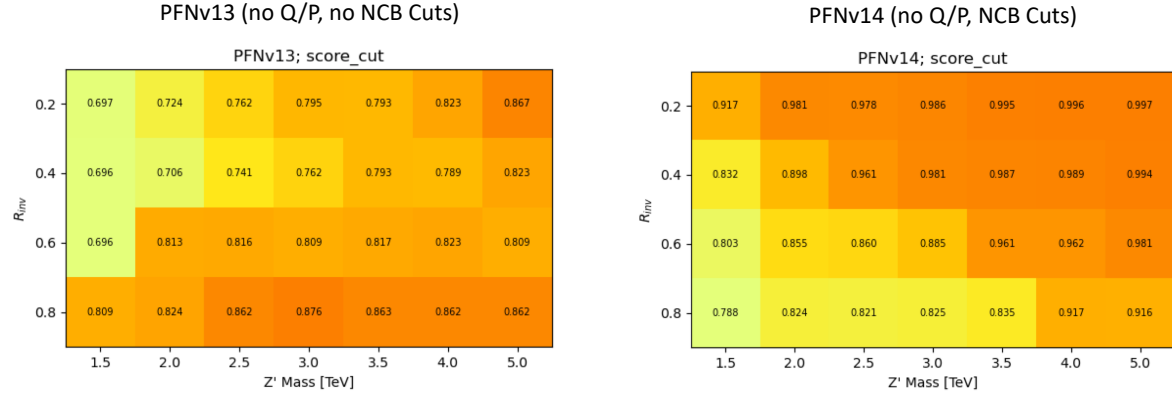


Figure B.5: Preferred cuts on the PFN score for each point in the grid, comparing the effect of adding the NCB preselection.

2144
2145 Grid cans for optimality were also performed on the number of training epochs, number of
2146 training events, batch size, learning rate, number of neurons, and dimension of the Φ space. The
2147 results of these scans are summarized in the tables in Figure B.6. The selected or default parameters
2148 were found to be optimal, or close enough to optimal to justify not increasing the training time or
2149 complexity of the network for negligible increases in performance.

2150 B.3 Supervised: BDT vs. PFN

2151 Studies of the BDT compared to the PFN performance, where training over events modeled
2152 with jet-related HLVs (high-level track variables, etas, angles, etc.) are compared to events mod-
2153 eled by the tracks of the 2 leading jets. Figure B.7 shows the performance of the BDT with and
2154 without explicit use of energy scale variables.

2155 B.4 Single Jet vs Jet System ML Approach

2156 The analysis considered both a single jet and jet system ML approach. A jet system approach,
2157 where the leading two jets and their orientation with respect to each other was selected for a variety
2158 of reasons. The jet system approach captures the MET information which is crucial to identifying

	default s_events=500096 b_events=501396	s_events:49135 b_events: 48220 *	s_events:246205 b_events:245136
AUC	.905	.874	.892

	default	n_neuro n 40	n_neuro n 150	phi_dim 32	phi_dim 128	learning rate 0.0005	learning rate 0.002	nepochs 50	nepochs 200*
AUC	.905	.898	.906	.902	.906	.898	.905	.893	.909

	default	batchsize_pfn 250	batchsize_pfn 1000
AUC	.905	.903	.902

Figure B.6: Scans done to check for optimality of PFN training parameters.

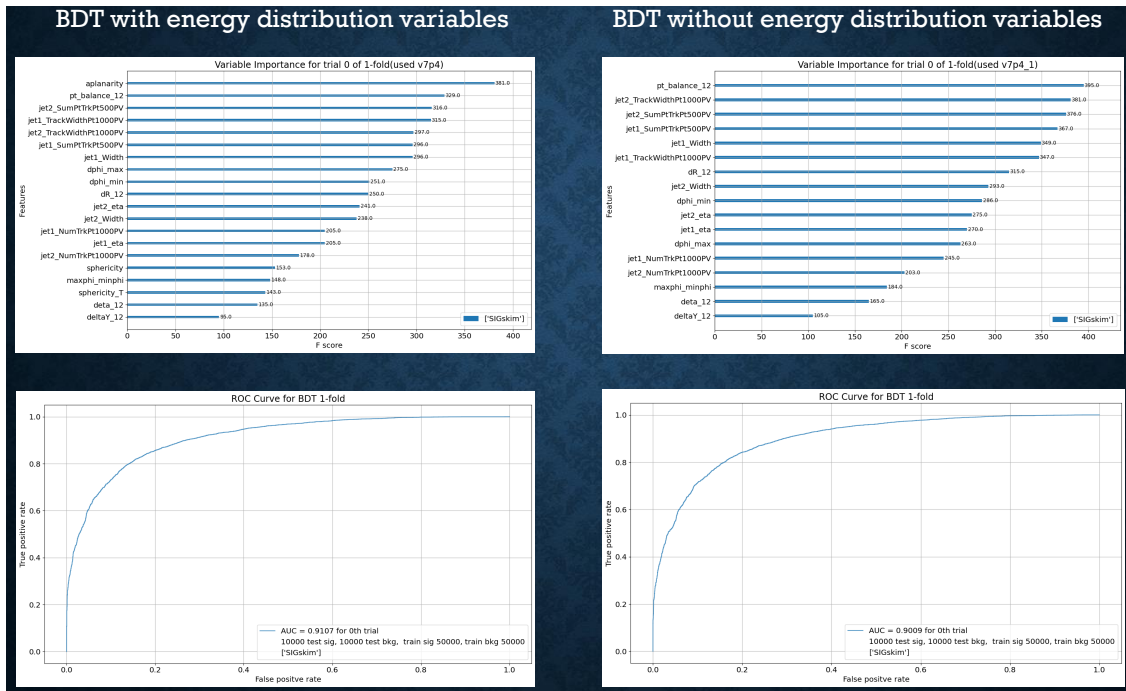


Figure B.7

2159 SVJs. In the topology where the dark quarks come from a heavy Z' decay and are back to back,
 2160 the measurable MET will have to be aligned with one or the other.

2161 Additionally, the performance of both a supervised PFN approach and an unsupervised AE ap-
 2162 proach was studied in the case of a single jet tagger. While the PFN approach was still performant
 2163 on a single jet case, the unsupervised approach was significantly improved by using both jets. This
 2164 is shown in Figure B.8.

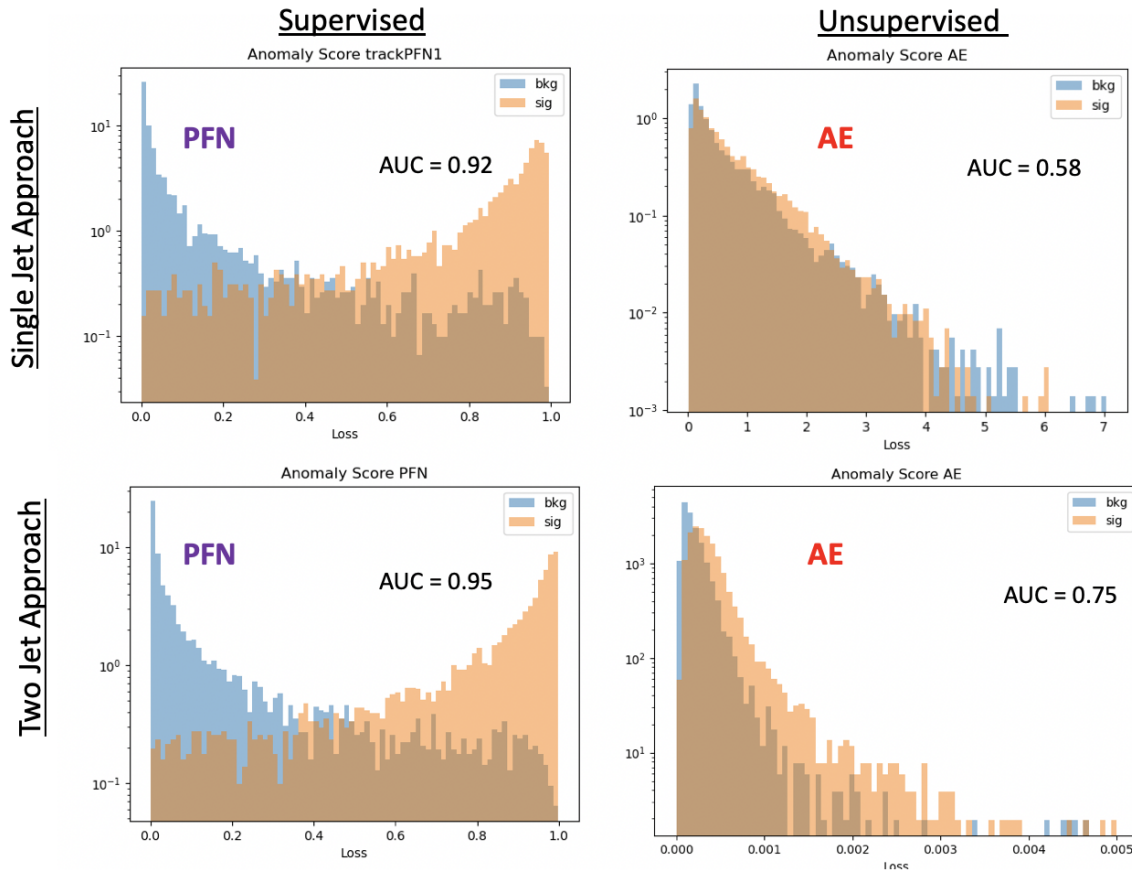


Figure B.8: ϕ Performance comparison between single jet and jet system ML approach

2165 B.5 PFN Training Composition

2166 The overall sensitivity and stability across the signal grid is observed to benefit by training
 2167 the ML tool to reject only the dominant background, QCD. This is evidenced by the PFN response
 2168 plots shown in Section 7.1.1 and the following AUC and sensitivity comparison plots in Figure B.9.

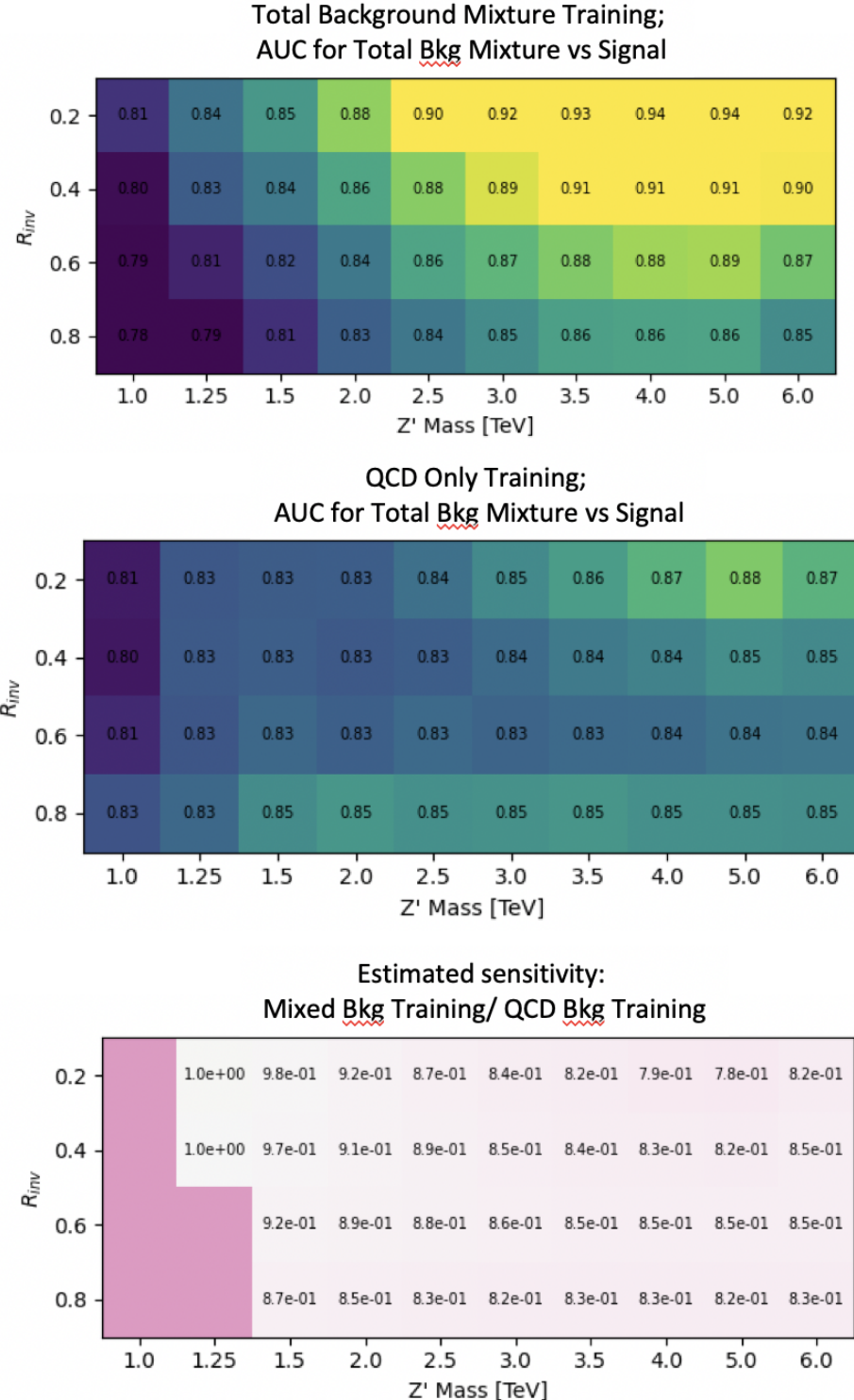


Figure B.9: ϕ Comparison in the AUC score across the grid for the mixed background strategy vs the QCD only strategy. The bottom table highlights that the QCD only strategy gives superior sensitivity across the signal grid.

2169 **B.6 E_T^{miss} and $E_T^{\text{miss}}\phi$ Shapes**

2170 The Tight cleaning working point was found to be necessary due to the nature of our signal
 2171 being E_T^{miss} and hadronic activity that are closely aligned, presenting a signature that is very af-
 2172 fected by beam-induced background (BIB). As per the cleaning recommendations, any event with
 2173 a jet that fails Tight criteria is rejected. Figure B.10 shows the effect of Tight cleaning on the shape
 of E_T^{miss} in data, fixing a feature present in Loose cleaning only.

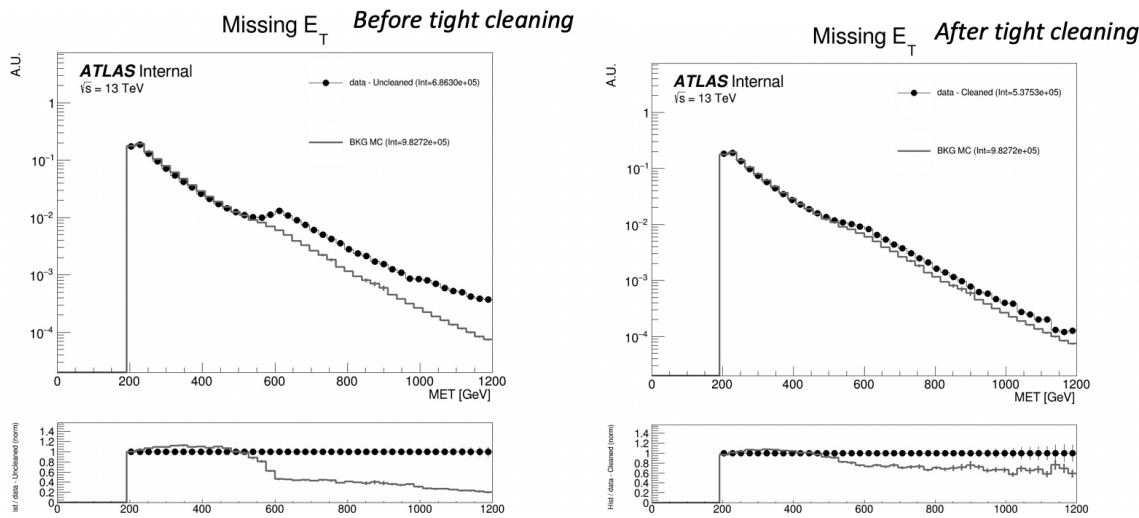


Figure B.10: E_T^{miss} in data before and after Tight event cleaning is applied.

2174
 2175 Figure B.11 further illustrates the correlation between the excess events and the leading jet p_T ,
 2176 and illustrates the impact of the tight cleaning in reducing this feature.

2177 Figure B.12 illustrates the 2D η vs ϕ distribution of the leading and subleading jets before and
 2178 after tight cleaning. No major spikes or hot areas are observed. One bright spot in the subleading
 2179 jet map at $\eta \approx 0$ and $\phi \approx -1.0$ was studies and found to have no impact on the E_T^{miss} shape, indicating
 2180 a likely missed spot in the Tile cleaning which does not affect E_T^{miss} .

2181 **B.6.1 NCB Preselection**

2182 A final preselection was derived to entirely remove the presence of non-collision background,
 2183 particularly noted through its impact on the E_T^{miss} shape. Cuts are added on the subleading jet

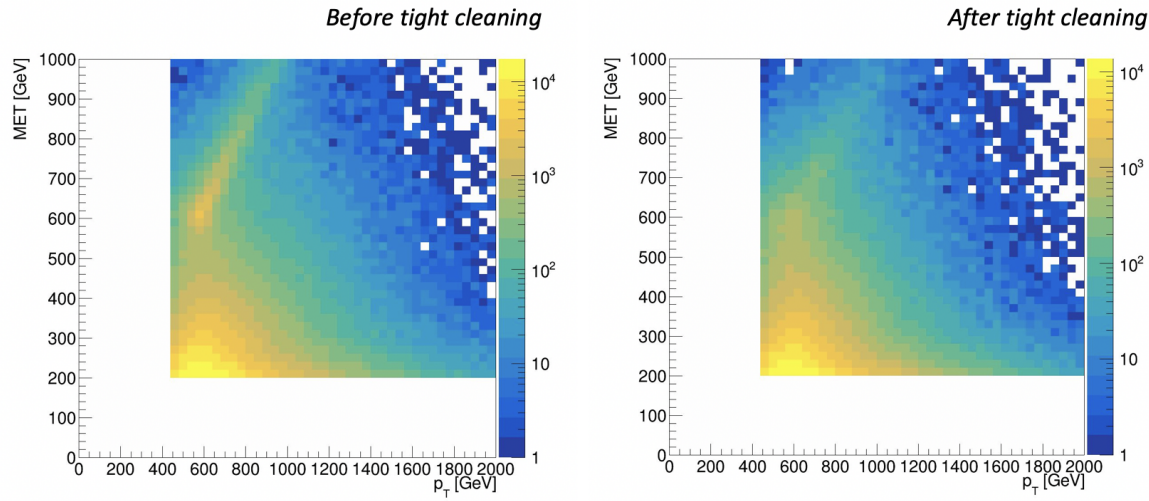


Figure B.11: E_T^{miss} vs jet1 p_T in data before and after Tight event cleaning is applied.

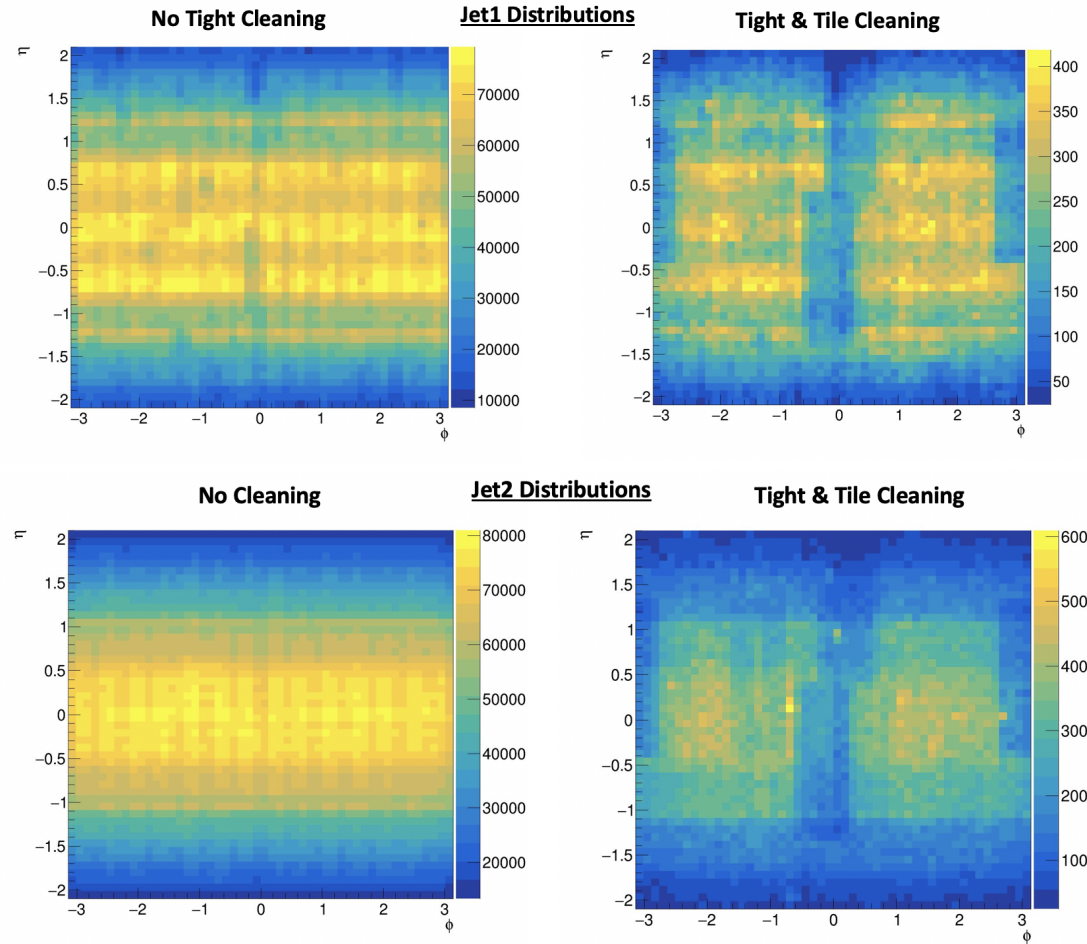


Figure B.12: η vs ϕ for leading and subleading jets, before and after the application of tight cleaning.

2184 $p_T > 150$ GeV and $\Delta\Phi(j1,j2) > 0.8$. Figure B.13 shows the impact of these cuts to create a fully
 2185 smoothly falling E_T^{miss} distribution. Figure B.14 shows the impact on the data yields in the CR and
 2186 VR and several signals in the SR; the greatest inefficiencies are found for the signal points that are
 2187 not sensitive in the analysis anyway. The reduction in background ultimately means that no impact
 is noticed on the limits.

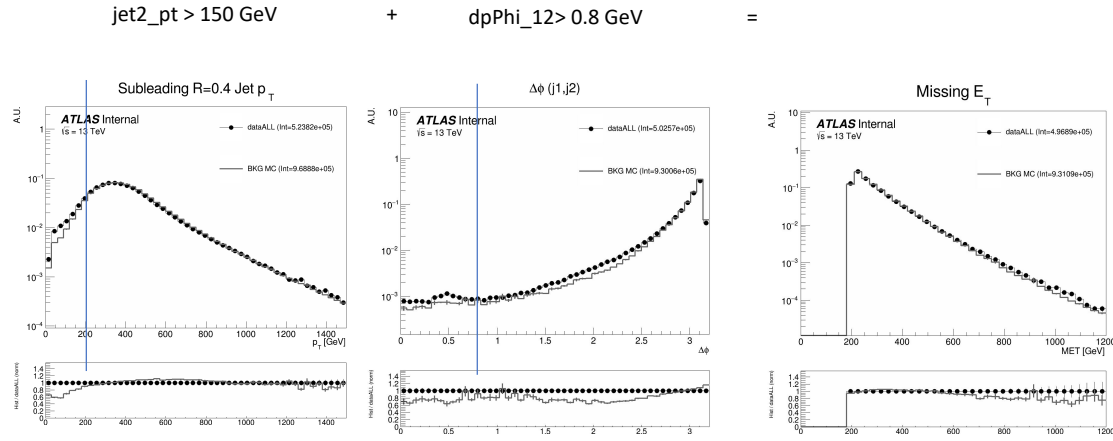


Figure B.13: Added NCB preselection and impact on E_T^{miss} shape.

2188
 2189 Figure B.15 shows the impact of these cuts on the 2D E_T^{miss} vs jet1 p_T distribution, where the
 2190 feature is also observed to be smoothed.

2191 This strategy was discussed and signed off by the Jet/ E_T^{miss} CP group ¹.

2192 B.6.2 TileCal Correction

2193 The $E_T^{\text{miss}}\phi$ distribution was fixed through the implementation of an offline TileCal correction
 2194 tool, which removes certain lumiblocks of certain runs based on poor functioning in TileCal mod-
 2195 ules. Figure B.16 shows the $E_T^{\text{miss}}\phi$ distribution in data across runs, before and after the application
 2196 of the tool, showing the ability of the tool to remove spikes due to instrumental problems.

¹<https://indico.cern.ch/event/1413217/>

Region	Before Extra Cleaning Cuts	After Extra Cleaning Cuts	Efficiency
Data - CR	108957	107435	0.99
Data - VR	116917	116008	0.99
2500, 0.2 - SR	1921	1709	0.89
2500, 0.4 - SR	1819	1424	0.78
2500, 0.6 - SR	1150	735	0.64
2500, 0.8 - SR	543	251	0.46
5000, 0.2 - SR	21.5	20.3	0.94
5000, 0.4 - SR	22.3	19.4	0.87
5000, 0.6 - SR	16.0	11.6	0.73
5000, 0.8 - SR	8.1	4.1	0.51

Figure B.14: NCB preselection impact on data and signal yields.

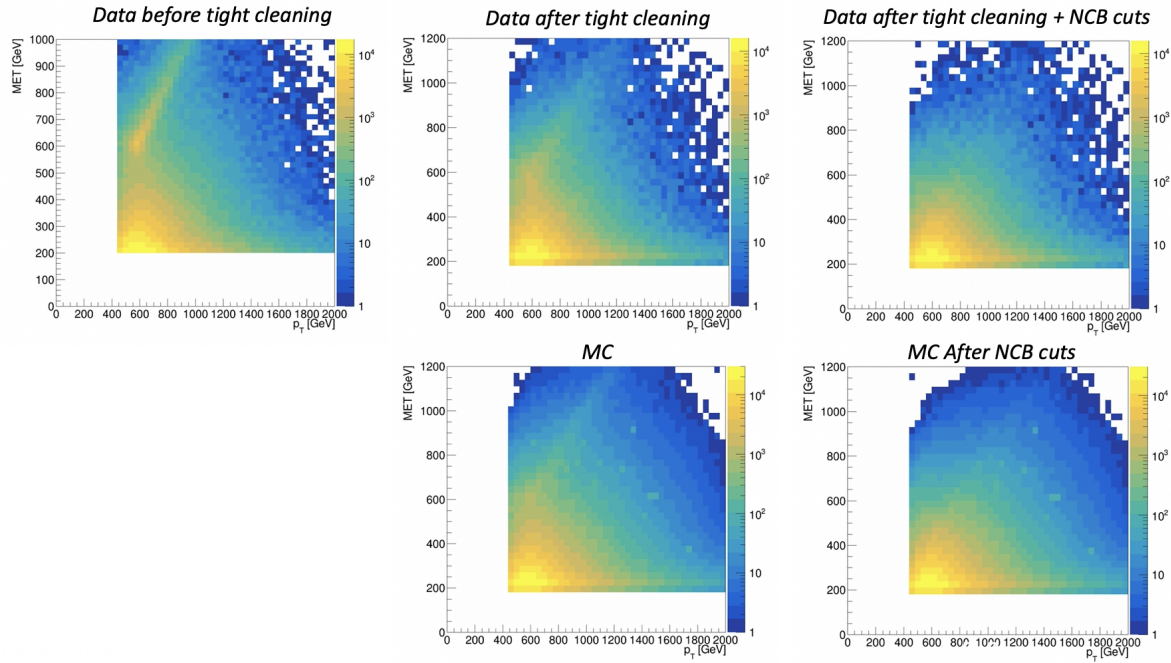


Figure B.15: Impact of tight cleaning and non-collision background preselection.

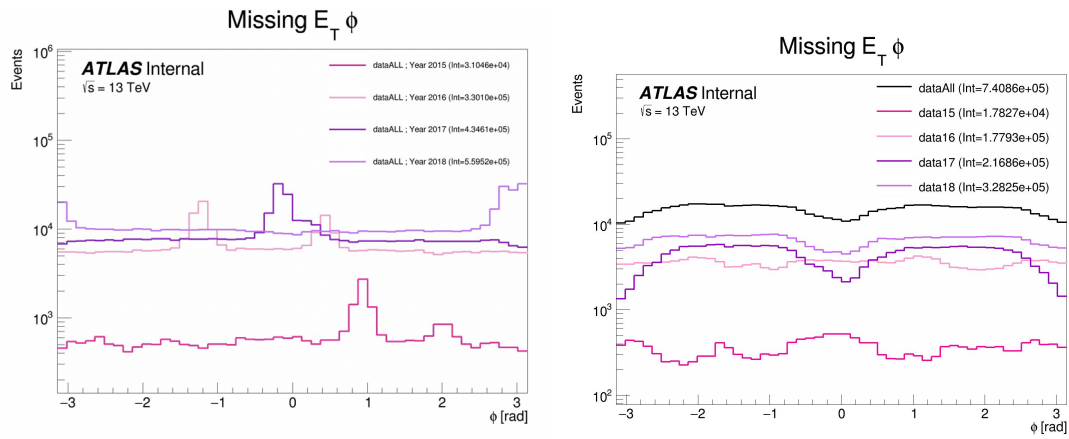


Figure B.16: $E_T^{\text{miss}}\phi$ in data, before (left) and after (right) application of the TileCal correction tool.

Appendix C: Truth Studies

2199 C.1 Jet dR Matching

2200 Figure C.1 demonstrates that the leading and subleading jet are overwhelmingly the most likely
 2201 jets to be matched to a dark quark.

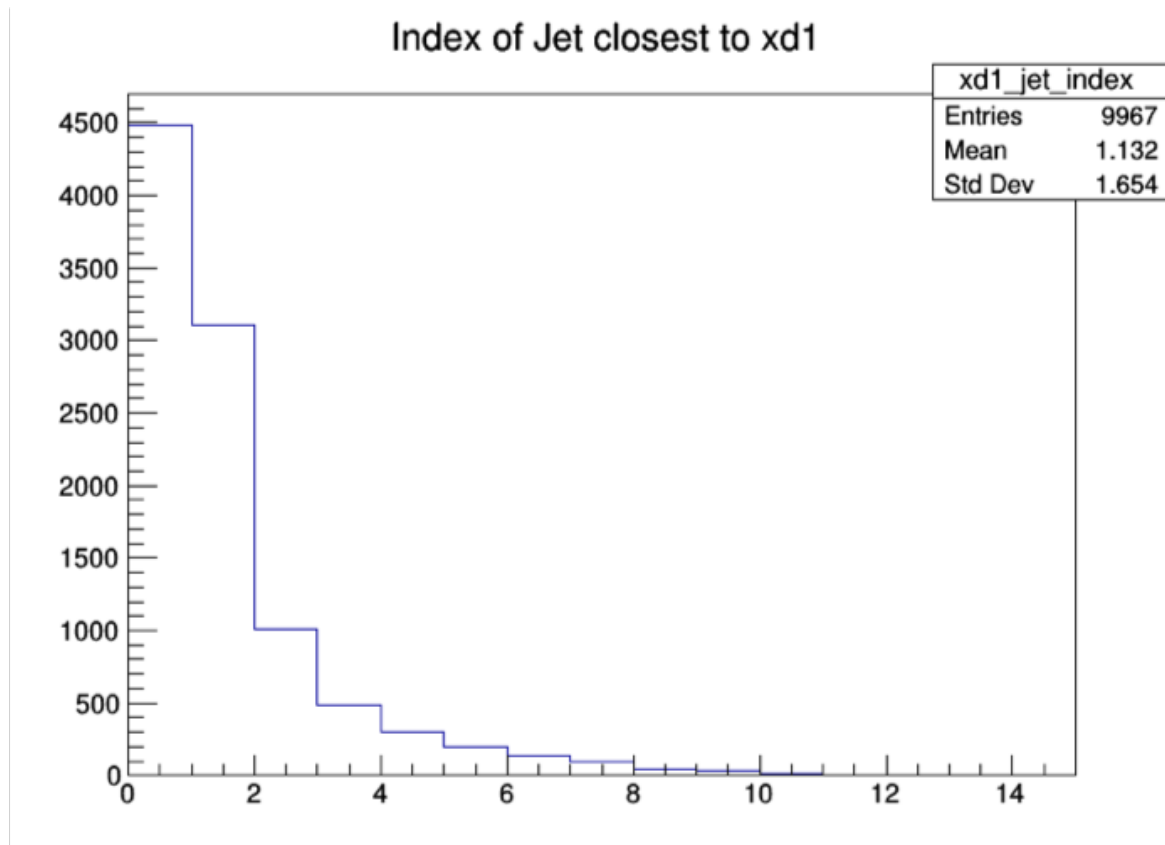


Figure C.1: Index of jets truth matched (by requirement of $\Delta R < 0.4$) with dark quark.

2202 Other matching strategies were explored, such as choosing the jet most aligned with $E_T^{\text{miss}}(\min$
 2203 $\Delta\phi(j, E_T^{\text{miss}}))$ and the jet most anti-aligned with $E_T^{\text{miss}}(\max \Delta\phi(j, E_T^{\text{miss}}))$. However, in most cases
 2204 these two measurements correspond to the subleading and leading jets respectively. Additionally,
 2205 as shown in Figure C.2 the leading/subleading strategy generally results in more matched jets than

2206 the E_T^{miss} aligned and E_T^{miss} anti-aligned strategy. Therefore the leading and subleading jets were
 2207 chosen for consideration in this analysis.

Signal ($M_{Z'}$, r_{inv})	% Leading Jets dR Matched	% MET anti- aligned Jets dR matched	% Subleading Jets dR Matched	% MET aligned jets dR matched
750 GeV, 0.2	0.432883	0.3567	0.3777	0.3504
750 GeV, 0.8	0.187819	0.1589	0.1826	0.1803
3500 GeV, 0.2	0.692931	0.5408	0.5097	0.4144
3500 GeV, 0.8	0.344057	0.2927	0.2634	0.2585
6000 GeV, 0.2	0.647237	0.5047	0.4975	0.3919
6000 GeV, 0.8	0.345542	0.2882	0.2517	0.249

Figure C.2: Percent of jets with $\Delta R(j, E_T^{\text{miss}}) < 0.4$ comparing two jet identification strategies. Leading and subleading jets are seen to be the better metric for identifying jets associated with the dark quark decay.